



<b>Publication Year</b>	2021
<b>Acceptance in OA @INAF</b>	2022-06-10T09:03:17Z
<b>Title</b>	Gaia Early Data Release 3. The astrometric solution
<b>Authors</b>	Lindgren, L.; Klioner, S. A.; Hernández, J.; Bombrun, A.; Ramos-Lerate, M.; et al.
<b>DOI</b>	10.1051/0004-6361/202039709
<b>Handle</b>	<a href="http://hdl.handle.net/20.500.12386/32262">http://hdl.handle.net/20.500.12386/32262</a>
<b>Journal</b>	ASTRONOMY & ASTROPHYSICS
<b>Number</b>	649

# Gaia Early Data Release 3

## The astrometric solution

L. Lindegren<sup>1</sup>, S. A. Klioner<sup>2</sup>, J. Hernández<sup>3</sup>, A. Bombrun<sup>4</sup>, M. Ramos-Lerate<sup>5</sup>, H. Steidelmüller<sup>2</sup>, U. Bastian<sup>6</sup>, M. Biermann<sup>6</sup>, A. de Torres<sup>4</sup>, E. Gerlach<sup>2</sup>, R. Geyer<sup>2</sup>, T. Hilger<sup>2</sup>, D. Hobbs<sup>1</sup>, U. Lammers<sup>3</sup>, P. J. McMillan<sup>1</sup>, C. A. Stephenson<sup>7</sup>, J. Castañeda<sup>8</sup>, M. Davidson<sup>9</sup>, C. Fabricius<sup>10</sup>, G. Gracia-Abril<sup>11,6</sup>, J. Portell<sup>10</sup>, N. Rowell<sup>9</sup>, D. Teyssier<sup>7</sup>, F. Torra<sup>8</sup>, S. Bartolomé<sup>10</sup>, M. Clotet<sup>10</sup>, N. Garralda<sup>10</sup>, J. J. González-Vidal<sup>10</sup>, J. Torra<sup>†,10</sup>, U. Abbas<sup>12</sup>, M. Altmann<sup>6,13</sup>, E. Anglada Varela<sup>14</sup>, L. Balaguer-Núñez<sup>10</sup>, Z. Balog<sup>6,15</sup>, C. Barache<sup>13</sup>, U. Becciani<sup>16</sup>, M. Bernet<sup>10</sup>, S. Bertone<sup>17,18,12</sup>, L. Bianchi<sup>19</sup>, S. Bouquillon<sup>13</sup>, A. G. A. Brown<sup>20</sup>, B. Bucciarelli<sup>12</sup>, D. Busonero<sup>12</sup>, A. G. Butkevich<sup>12</sup>, R. Buzzì<sup>12</sup>, R. Cancelliere<sup>21</sup>, T. Carlucci<sup>13</sup>, P. Charlot<sup>22</sup>, M.-R. L. Cioni<sup>23</sup>, M. Crosta<sup>12</sup>, C. Crowley<sup>4</sup>, E. F. del Peloso<sup>6</sup>, E. del Pozo<sup>24</sup>, R. Drimmel<sup>12</sup>, P. Esquej<sup>25</sup>, A. Fienga<sup>26,27</sup>, E. Fraile<sup>25</sup>, M. Gai<sup>12</sup>, M. Garcia-Reinaldos<sup>3</sup>, R. Guerra<sup>3</sup>, N. C. Hambly<sup>9</sup>, M. Hauser<sup>15,28</sup>, K. Janßen<sup>23</sup>, S. Jordan<sup>6</sup>, Z. Kostrzewa-Rutkowska<sup>20,29</sup>, M. G. Lattanzi<sup>12,30</sup>, S. Liao<sup>12</sup>, E. Licata<sup>12</sup>, T. A. Lister<sup>31</sup>, W. Löffler<sup>6</sup>, J. M. Marchant<sup>32</sup>, A. Masip<sup>10</sup>, F. Mignard<sup>33</sup>, A. Mints<sup>23</sup>, D. Molina<sup>10</sup>, A. Mora<sup>24</sup>, R. Morbidelli<sup>12</sup>, C. P. Murphy<sup>3</sup>, C. Pagani<sup>34</sup>, P. Panuzzo<sup>35</sup>, X. Peñalosa Esteller<sup>10</sup>, E. Poggio<sup>12</sup>, P. Re Fiorentin<sup>12</sup>, A. Riva<sup>12</sup>, A. Sagristà Sellés<sup>6</sup>, V. Sanchez Gimenez<sup>10</sup>, M. Sarasso<sup>12</sup>, E. Sciacca<sup>16</sup>, H. I. Siddiqui<sup>36</sup>, R. L. Smart<sup>12</sup>, D. Souami<sup>37,38</sup>, A. Spagna<sup>12</sup>, I. A. Steele<sup>32</sup>, F. Taris<sup>13</sup>, E. Utrilla<sup>24</sup>, W. van Reeve<sup>24</sup>, and A. Vecchiato<sup>12</sup>

(Affiliations can be found after the references)

Received 18 October 2020 / Accepted 18 November 2020

### ABSTRACT

**Context.** *Gaia* Early Data Release 3 (*Gaia* EDR3) contains results for 1.812 billion sources in the magnitude range  $G = 3\text{--}21$  based on observations collected by the European Space Agency *Gaia* satellite during the first 34 months of its operational phase.

**Aims.** We describe the input data, the models, and the processing used for the astrometric content of *Gaia* EDR3, as well as the validation of these results performed within the astrometry task.

**Methods.** The processing broadly followed the same procedures as for *Gaia* DR2, but with significant improvements to the modelling of observations. For the first time in the *Gaia* data processing, colour-dependent calibrations of the line- and point-spread functions have been used for sources with well-determined colours from DR2. In the astrometric processing these sources obtained five-parameter solutions, whereas other sources were processed using a special calibration that allowed a pseudocolour to be estimated as the sixth astrometric parameter. Compared with DR2, the astrometric calibration models have been extended, and the spin-related distortion model includes a self-consistent determination of basic-angle variations, improving the global parallax zero point.

**Results.** *Gaia* EDR3 gives full astrometric data (positions at epoch J2016.0, parallaxes, and proper motions) for 1.468 billion sources (585 million with five-parameter solutions, 882 million with six parameters), and mean positions at J2016.0 for an additional 344 million. Solutions with five parameters are generally more accurate than six-parameter solutions, and are available for 93% of the sources brighter than the 17th magnitude. The median uncertainty in parallax and annual proper motion is 0.02–0.03 mas at magnitude  $G = 9\text{--}14$ , and around 0.5 mas at  $G = 20$ . Extensive characterisation of the statistical properties of the solutions is provided, including the estimated angular power spectrum of parallax bias from the quasars.

**Key words.** astrometry – parallaxes – proper motions – methods: data analysis – space vehicles: instruments

## 1. Introduction

*Gaia* Early Data Release 3 (EDR3; [Gaia Collaboration 2021a](#)) contains provisional astrometric and photometric data for more than 1.8 billion ( $1.8 \times 10^9$ ) sources based on the first 34 months of observations made by the European Space Agency's *Gaia* mission ([Gaia Collaboration 2016a](#)) since the start of the nominal operations in July 2014. The astrometric data in EDR3 include the five astrometric parameters (position, parallax, and proper motion) for 1.468 billion sources, and the approximate

positions at epoch J2016.0 for an additional 344 million mostly faint sources. All sources have magnitudes in *Gaia*'s unfiltered photometric passband  $G$ , and 1.544 billion have two-colour photometry in the passbands  $G_{BP}$  and  $G_{RP}$  defined by the blue and red photometers (BP and RP; [Riello et al. 2021](#)). The magnitudes of the well-observed sources range from  $G = 6\text{--}21$ . All data are publicly available in the online *Gaia* Archive<sup>1</sup>.

The EDR3 is a subset of the full *Gaia* Data Release 3 (DR3), planned for the first half of 2022. The full release will provide a much wider set of data, including detailed spectrophotometric

<sup>†</sup> Deceased.

<sup>1</sup> <https://archives.esac.esa.int/gaia>

and variability information, additional astrometric data on non-single and extended objects, and the radial velocities, object classification, and astrophysical parameters for many sources. However, the basic astrometric information on the *Gaia* DR3 sources, obtained by treating all of them as single stars, has already been provided in EDR3 and will not change for DR3.

This paper gives an overview of the processing leading up to the EDR3 astrometry, as well as of the main characteristics of the astrometric results. Further details are provided in the online documentation of the *Gaia* Archive and in specialised papers. In particular, the celestial reference frame of *Gaia* (E)DR3 is described in Gaia Collaboration (in prep.), the parallax bias (zero point) is discussed in Lindegren et al. (2021), and the overall properties of the release are reviewed in Fabricius et al. (2021). A general description of the *Gaia* mission can be found in Gaia Collaboration (2016a).

The core astrometric solution for *Gaia*, known as AGIS (astrometric global iterative solution), was comprehensively described in the pre-launch paper by Lindegren et al. (2012). This remains a useful general reference for AGIS in spite of the many modifications and improvements introduced since 2012. We also refer frequently to Lindegren et al. (2018), which describes the astrometric solution for *Gaia* DR2.

## 2. Overview of the astrometric processing

### 2.1. Main processing tasks

In the cyclic processing scheme adopted by the *Gaia* Data Processing and Analysis Consortium (DPAC; Gaia Collaboration 2016a), EDR3 and DR3 are products of the third processing cycle, using observations in the first four data segments called DS0–DS3 in Fig. 1. The data segments are just a convenient, but essentially arbitrary division of the raw data by acquisition time. As suggested in the figure, the cycles treat successively larger chunks of the raw data by including additional segments, but in every cycle the old segments are always reprocessed together with the new ones. This iterative reprocessing of earlier data segments is necessary in order to achieve the uniformly best treatment of all the data, and a consistent assignment of source identifiers to the on-board detections.

In Fig. 1, the boxes labelled PhotPipe represent the complex photometric processing described elsewhere (Riello et al. 2021; Carrasco et al., in prep.; De Angeli et al., in prep.). This is not part of the astrometric processing as such but is included in the diagram because the photometric information, and in particular the colour information encoded in the effective wavenumbers ( $\nu_{\text{eff}}$ ; Sect. 2.3) calculated in PhotPipe, are needed for calibrating the colour-dependent line-spread and point-spread functions (LSF and PSF) of the astrometric instrument. Because PhotPipe runs essentially in parallel with the astrometric solution (AGIS), this implies that the astrometric processing in cycle  $N$  must use photometric information from cycle  $N-1$ .

The boxes in Fig. 1 labelled SDM, CALIPD, and AGIS represent the three main stages in the processing of the raw CCD (charge-coupled device) data that are of immediate relevance for the astrometry.

In the first stage, the SDM (source, detection-classifier, and cross-match) aims to identify all on-board detections belonging to the same source and assign a unique source identifier (source\_id) to each such cluster of detections (Torra et al. 2021). An important part of the process is the identification of spurious detections, created for example by the diffraction spikes of bright stars (Fabricius et al. 2016). Because the updated source

list and table of links to the (genuine) detections created by the SDM is used by all subsequent processes, this is one of the first tasks to be executed in a cycle. The source list from the previous cycle is a starting point for the task, but the new data and improved reconstruction of the satellite attitude (a key element in translating observed transit times into positions) unavoidably require some of the old sources to be split or merged, in addition to creating entirely new ones. For example, EDR3 contains many pairs of sources (most of which are genuine binaries) that are separated by less than 0.4 arcsec, where DR2 had only one. Such cases could lead to the assignment of new source identifiers for both components. The auxiliary table `dr2_neighbourhood` helps to trace the evolution of source identifiers.

The second stage, CALIPD, consists of two parts, calibration (CAL) and image parameter determination (IPD). In CAL, the LSF (for one-dimensional observations) and PSF (for two-dimensional observations) are calibrated as functions of time, colour, and several other variables in order to take into account the optical imperfections of the instrument and their temporal evolution (Rowell et al. 2021). The LSF and PSF describe the shape of the image profile for a point source as well as the small displacement caused by chromatic effects (Sect. 2.3). In IPD, the LSF or PSF relevant for a particular observation is fitted to the sampled CCD image, yielding precise estimates of its one- or two-dimensional location in the pixel stream and of the total flux of the image in the  $G$  band (Fabricius et al. 2016). The resulting image locations constitute the main input data for the astrometric solution, while the flux estimates are used for the determination of  $G$  magnitudes in PhotPipe. Whereas CAL only uses a small fraction of the available observations for the LSF and PSF calibrations, IPD is applied to all observations in the skymapper (SM) and astrometric field (AF).

In the third stage, AGIS performs a simultaneous least-squares estimation of the attitude, instrument calibration, and the five astrometric parameters for a subset of well-behaved primary sources (about 14.3 million in cycle 3). The calibration includes corrections for effects that are not accounted for in the CALIPD, or only partially corrected at that stage. The comprehensive pre-launch description of AGIS in Lindegren et al. (2012) is complemented by specifics of the current models in Sect. 3.

SDM and CALIPD belong to the intermediate data update (IDU) system, which includes several additional tasks such as astrophysical background estimation (Fabricius et al. 2016) and electronic calibrations (Hambly et al. 2018). Compared with DR2, several major improvements of the IDU have been introduced with cycle 3. In SDM the treatment of high-proper motion stars, very bright stars, variable sources, and close pairs has been much improved (Torra et al. 2021). In CALIPD the image profiles (LSF and PSF) are no longer assumed to be independent of time and colour, as was the case in cycle 2, and a much more realistic two-dimensional model (PSF) is used (Rowell et al. 2021). Moreover, as described in Sect. 2.3 and Fig. 1, the CALIPD and AGIS tasks are for the first time iterated in order that CALIPD may benefit from the improved astrometry, attitude, and instrument calibration obtained by including the new data segment (DS3) in AGIS.

### 2.2. Observations used

*Gaia* EDR3 is based on data collected from the start of the nominal observations on 25 July 2014 (10:30 UTC) until 28 May 2017 (08:45 UTC), or 1038 days (data segments DS0–DS3 in Fig. 1). Similarly to the astrometric solution for DR2 (Lindegren et al. 2018), this solution did not use the observations in the first month

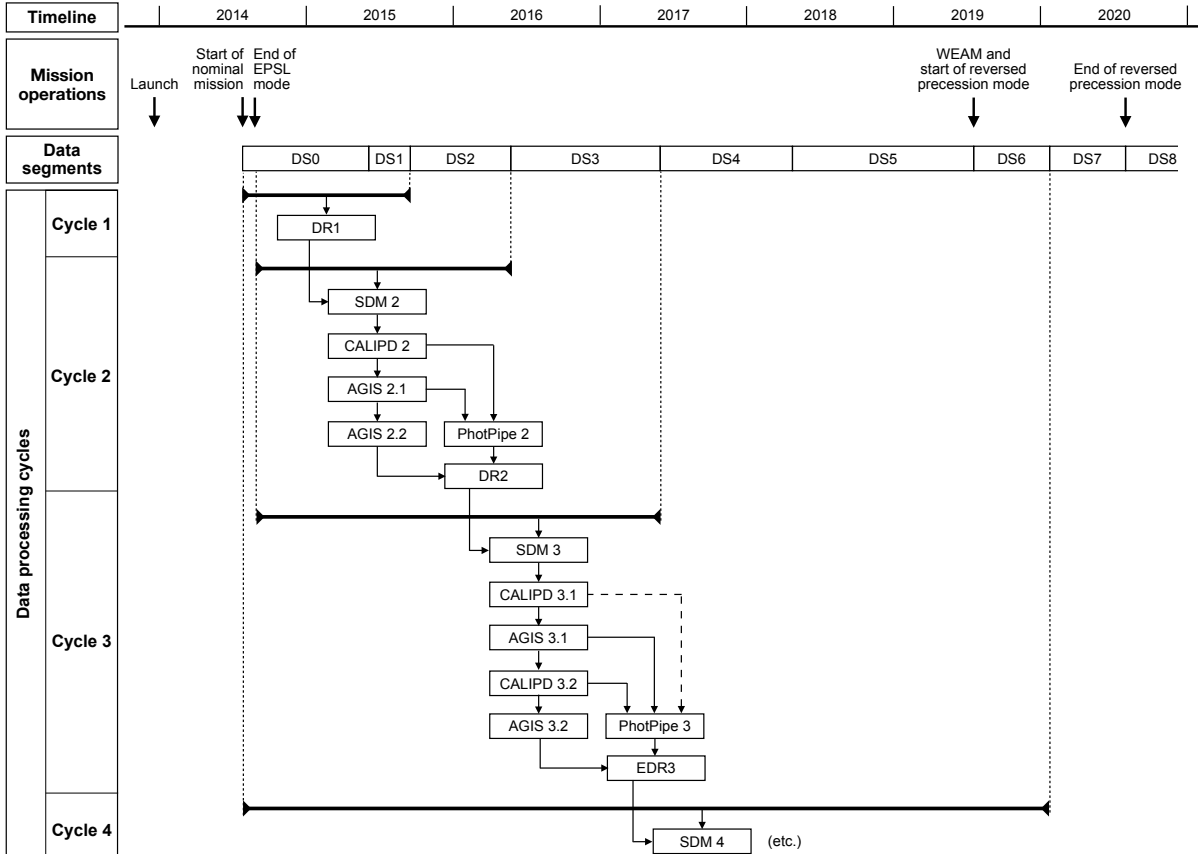


**Fig. 1.** Main steps of the EDR3 astrometry processing and their place in the cyclic processing scheme of DPAC. *Gaia* EDR3 (and DR3) are generated in the third processing cycle (cycle 3). The stretches of observational data processed in the different cycles are indicated by thick horizontal lines. The boxes connected by arrows show the sequence of processing steps and their interdependencies, but they are not placed chronologically on the timeline. Only steps directly relevant for the astrometry are shown, leaving out most of the complexities of the full DPAC processing. No details are given for DR1. The first month of the nominal mission, with observations made in the ecliptic pole scanning law (EPSL) mode, was not used for the astrometry in DR2 and EDR3, but may be incorporated in later releases. The Whitehead eclipse avoidance manoeuvre (WEAM) on 16 July 2019 marks the beginning of the extended mission. In the first year of the extended mission (data segments DS6 and DS7), scanning was made in the reversed precession mode (Sect. 6.4). The processes SDM, CALIPD, AGIS, and PhotPipe are explained in Sect. 2.1.

of the operational phase, when the special ecliptic pole scanning law (EPSL) was employed. The data for the astrometry therefore start on 22 August 2014 (21:00 UTC) and cover 1009 days or 2.76 yr, with some interruptions mentioned below.

The time coverage for this solution is therefore about one year longer than the astrometric solution for *Gaia* DR2, which covered 640 days or 1.75 yr. The expected improvement from the added data and longer time baseline scales as  $T^{-1/2}$  for the parallaxes and positions at the mean epoch of observation, and as  $T^{-3/2}$  for the proper motions; thus uncertainties should be smaller by a factor 0.80 for the parallaxes and positions, and by a factor 0.51 for the proper motions. As shown in Sect. 5.4, the median ratios of the formal uncertainties are slightly better than this thanks to additional improvements in the instrument and attitude modelling. The reference epoch J2016.0 used for the astrometry in *Gaia* EDR3 (Sect. 3.1) is close to the mid-point of the observations.

The on-board mission timeline (OBMT) is conveniently used to label on-board events; it is expressed as the number of nominal revolutions of exactly 21 600 s (6 h) on-board time from an arbitrary origin<sup>2</sup>. The approximate relation between OBMT

(in revolutions) and barycentric coordinate time (TCB, in Julian years) at *Gaia* is

$$\text{TCB} \approx \text{J2015.0} + (\text{OBMT} - 1717.6256 \text{ rev}) / (1461 \text{ rev yr}^{-1}), \quad (1)$$

or as a Julian Date,

$$\text{JD}2457023.75 + (\text{OBMT} - 1717.6256 \text{ rev}) / (4 \text{ rev d}^{-1}). \quad (2)$$

The nominal observations start at OBMT 1078.38 rev. The astrometric solution used data in the interval OBMT 1192.13–5230.09 rev (J2014.64032–J2017.40415), with major gaps as listed in Table 1.

### 2.3. Use of colour information in CALIPD and AGIS

In the focal plane of an all-reflecting telescope, free of wave-front aberrations, the point-spread function (PSF) is completely symmetric. Although the width of the PSF increases with wavelength, because of diffraction, its position does not change and is consequently independent of the spectral composition of the

the data processing (see Sect. 2.4), but ignored when giving intervals in OBMT.

<sup>2</sup> The rubidium atomic clock on board of *Gaia* does not count SI seconds because it is a free-running oscillator with some (very small) time-dependent frequency error. This is calibrated in a special part of

**Table 1.** Major gaps and events affecting the astrometric solution.

$t_{\text{beg}}$	$t_{\text{end}}$	Length	Description
1220.400	1225.200	4.800	VPU reset
1316.490	1389.113	72.623	Decontamination #4
1443.800	1444.200	0.400	Refocus (following FoV)
1653.800	1660.000	6.200	PAA anomaly
1820.900	1830.000	9.100	PAA anomaly
2094.000	2099.000	5.000	PDHU anomaly
2179.125	2191.000	11.875	VPU software update
2192.252	2195.218	2.967	Observation gap
2238.000	2242.000	4.000	Unknown
2322.300	2401.559	79.259	Decontamination #5
2405.967	2408.643	2.676	Observation gap
2408.935	2409.968	1.033	Observation gap
2574.640	2575.400	0.760	Refocus (preceding FoV)
2954.200	2958.000	3.800	Moon eclipse
3045.133	3049.000	3.867	PDHU anomaly
3603.250	3605.227	1.976	Observation gap
3646.800	3650.000	3.200	Moon eclipse
3663.700	3667.000	3.300	Moon eclipse
4074.210	4076.063	1.853	Observation gap
4112.463	4180.000	67.537	Decontamination #6
4271.753	4275.200	3.445	PAA anomaly
4477.441	4481.000	3.550	PAA anomaly
4512.502	4515.000	2.498	PAA anomaly
4545.144	4548.000	2.856	PAA anomaly
5078.547	5080.600	2.053	STR anomaly

**Notes.** The table lists gaps longer than 1 revolution (0.25 day) and some other events of relevance for the calibration model.  $t_{\text{beg}}$  and  $t_{\text{end}}$  are the start and end times of the gap in OBMT revolutions (see Eq. (1)). The third column is the length of the gap in revolutions. Abbreviations: VPU = video processing unit, FoV = field of view, PAA = phased array antenna, PDHU = payload data handling unit, STR = star tracker.

light (achromatic). This is no longer true for a real instrument like *Gaia*. Inevitable coma-like wavefront errors produce asymmetric PSFs, in which both the shape and location depend on the spectrum. Subtle wavelength-dependent effects can also be introduced by the CCD detector itself. We use “chromaticity” as a generic term for these several effects, but especially for the variation of the PSF location with colour. Chromaticity creates colour-dependent biases in the astrometric results, unless it is properly calibrated and corrected for in the processing.

Chromaticity should ideally be completely eliminated already in CALIPD, so that the astrometric solution (AGIS) would not need to care about the sources having different colours. This requires (i) that in CAL both the shape and location of the LSF or PSF are accurately calibrated as functions of the spectral energy distribution (multiplied by the wavelength passband); and (ii) that in IPD the location and flux of the image are estimated using the correct profile, depending on the actual spectrum of the source in each observation. The astrometric parameters determined in the subsequent AGIS solution will then be free from chromatic biases. There is a certain circularity here: To achieve (i), CAL must be able to identify the point in the image profile that corresponds to the achromatic centre of the source, and this can only be done by means of the (achromatic) astrometric parameters determined by AGIS. This strong interdependency between CALIPD and AGIS is dealt with by executing the two tasks alternately, which motivates

the sequence CALIPD 3.1, AGIS 3.1, CALIPD 3.2, AGIS 3.2 in Fig. 1. The CALIPD/AGIS sequence should ideally be iterated until convergence, but in cycle 3 only two iterations (3.1 and 3.2) were made. This appears to be sufficient in practice, because AGIS is able to eliminate most of the chromatic effects left uncorrected in IPD via the colour-dependent terms in the AGIS calibration model (Sect. 3.3).

In cycle 3 two simplifying assumptions are made, both of which may be relaxed at some future time. The first is that the spectral information needed for the chromaticity correction is fully encoded in the effective wavenumber, defined as  $\nu_{\text{eff}} = \langle \lambda^{-1} \rangle$ . Here  $\lambda$  is the wavelength, and angular brackets denote a mean value weighted by the detected photon flux per unit wavelength interval. This quantity was chosen, in preference to (say) the effective wavelength or colour index, based on pre-launch studies using the properties of the *Gaia* instrument as expected at the time. According to these studies, the effective wavenumber provides a good one-dimensional parametrisation of chromaticity for ordinary stellar spectra, but may not be enough to describe shifts at the few  $\mu\text{s}$  level in atypical cases such as quasar spectra. Thus, more complex dependencies on the source spectrum may have to be considered in the future, but for the time being we use  $\nu_{\text{eff}}$  as defined.

The second assumption is that the spectrum (or effective wavenumber) is the same in all observations of a given source. Although this is a sufficiently good approximation for most sources, it may prevent us from reaching the full potential of *Gaia* for some variable objects. The remedy is simple in principle, namely to use the actual colour of the source at each observation, but this may require an additional iteration over PhotPipe and the variability analysis (Holl et al. 2018).

Even with the simplifications mentioned above, the conditions for eliminating chromaticity in CALIPD are not fully met in cycle 3. The main obstacle is that many sources do not have reliable colour information that can be used to select the appropriate image profiles for the IPD. The effective wavenumbers used in CALIPD 3.1 and 3.2 were calculated in PhotPipe 2 directly from the sampled and calibrated mean BP and RP spectra, and are given in EDR3 as `nu_eff_used_in_astrometry`. The analysis of the BP and RP spectra is very challenging in crowded areas and at the faintest magnitudes, owing to the blending of overlapping spectra and the difficulty to estimate the background accurately (De Angeli et al., in prep.). A strict filtering on the quality of  $\nu_{\text{eff}}$  was adopted in order to avoid that biases in the photometric colour might propagate into the astrometry. Of particular concern was the BP+RP flux excess issue (Evans et al. 2018), which in DR2 tended to make faint sources in crowded areas too blue. As a result of the adopted filtering, about two thirds of the sources in EDR3 do not have a valid `nu_eff_used_in_astrometry`. The situation is more favourable for brighter sources, where, for example, only 12% of the sources with  $G < 18$  mag lack a valid  $\nu_{\text{eff}}$ .

For the many sources without a valid  $\nu_{\text{eff}}$ , special procedures were used both in IPD and AGIS. In the IPD, image parameters were estimated by fitting the calibrated LSF or PSF for the default wavenumber  $\nu_{\text{eff}}^{\text{def}} = 1.43 \mu\text{m}^{-1}$ . This value was chosen to be close to the mean  $\nu_{\text{eff}}$  of faint sources, for which the default value is mostly used; thus, the averaged error introduced by the procedure is minimised. In AGIS, a six-parameter solution was computed for these sources, where the sixth unknown, after the standard five astrometric parameters, is the pseudocolour. This quantity, denoted  $\hat{\nu}_{\text{eff}}$ , is an astrometric estimate of the effective wavenumber  $\nu_{\text{eff}}$ . In order to estimate the pseudocolour, it is assumed that the chromatic shift of the image location caused



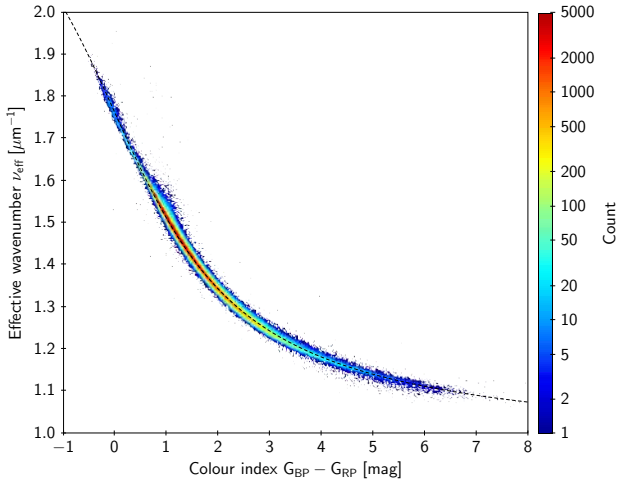


**Fig. 2.** Relation between the colour index and effective wavenumber for a random sample of 1.5 million sources in EDR3 brighter than  $G = 18$ . The dashed curve is the approximate mean relation in Eqs. (3) or (4).

by using the wrong colour (that is, the default colour) in IPD is linearly proportional to  $\nu_{\text{eff}} - \nu_{\text{eff}}^{\text{def}}$ . The constant of proportionality is a property of the instrument that can be determined in a special AGIS calibration solution using sources for which  $\nu_{\text{eff}}$  is known (step 6 in Sect. 4.1).

The sources with six-parameter solutions in EDR3 are identified by the flag `astrometric_params_solved = 95`. The estimated  $\hat{\nu}_{\text{eff}}$  (expressed in  $\mu\text{m}^{-1}$ ) is given as `pseudocolour`; like the other astrometric parameters it comes with a formal uncertainty (`pseudocolour_error`) and correlation coefficients (`ra_pseudocolour_corr`, etc.). The full  $6 \times 6$  covariance matrix can thus be reconstructed, which makes it possible to compute improved estimates of the astrometric parameters if a better estimate of the colour than the `pseudocolour` is available (see Appendix C). We note that `nu_eff_used_in_astrometry` is not given for the sources with six-parameter solutions.

Conversely, sources with a standard five-parameter solution (`astrometric_params_solved = 31`) have the field `nu_eff_used_in_astrometry` set, but no `pseudocolour`. Neither colour field is set for sources that have only a position in EDR3 (`astrometric_params_solved = 3`).

The relation between the colour index  $G_{\text{BP}} - G_{\text{RP}}$  (`bp_rp`) and effective wavenumber  $\nu_{\text{eff}}$  (`nu_eff_used_in_astrometry`) in EDR3 is illustrated in Fig. 2. As shown by the diagram, there is no unique one-to-one relation between the two colour parameters. One reason is that  $\nu_{\text{eff}}$  for cycle 3 was computed in the previous cycle (by PhotPipe 2), and is therefore not completely consistent with other photometric data in EDR3, including the colour indices. But the main reason for the scatter is the very different methods of computation ( $\nu_{\text{eff}}$  as a weighted sum over the sampled BP and RP spectra,  $G_{\text{BP}} - G_{\text{RP}}$  from the integrated BP and RP fluxes), which give slightly different results depending on the detailed spectra. When an approximate relation is needed, the following analytical formulae may be useful:

$$\nu_{\text{eff}} \approx 1.76 - \frac{1.61}{\pi} \operatorname{atan}\left(0.531(G_{\text{BP}} - G_{\text{RP}})\right) \mu\text{m}^{-1}, \quad (3)$$

$$G_{\text{BP}} - G_{\text{RP}} \approx \frac{1}{0.531} \tan\left(\frac{\pi}{1.61} (1.76 - \nu_{\text{eff}})\right) \text{mag}. \quad (4)$$

For  $-0.5 \leq G_{\text{BP}} - G_{\text{RP}} \leq 7$  they represent the mean relation for stellar objects to within  $\pm 0.007 \mu\text{m}^{-1}$  in the effective wavenumber. The `atan/tan` functions conveniently describe the non-linear relation to a useful approximation, and has the additional advantage that  $\nu_{\text{eff}}$  is restricted to the physically plausible interval  $[0.955, 2.565] \mu\text{m}^{-1}$  for arbitrarily large (positive or negative) colour indices.

#### 2.4. Auxiliary data

The processing of *Gaia* data aims at producing the most accurate astrometric catalogue consistent with the observations, using a minimum of external auxiliary data. Some external data are nevertheless needed, for example to align the catalogue with the celestial reference system and correct for stellar aberration. The main auxiliary data used in the processing are described below.

**Reference frame.** The orientation of the axes of the International Celestial Reference System (ICRS) is conventionally defined by means of the accurate positions for extragalactic radio sources observed by very long baseline interferometry. As of 1 January 2019, the defining list is the third realisation of the International Celestial Reference Frame (ICRF3; Charlot et al. 2020) containing 4588 radio sources. The orientation of *Gaia*-CRF3, the celestial reference frame of *Gaia* EDR3 (Gaia Collaboration, in prep.), was fixed by means of 2269 ICRF3 S/X sources, for which optical counterparts have been identified in EDR3 and which have a valid colour information `nu_eff_used_in_astrometry`. In order to correct a specific problem identified with the bright reference frame of EDR3 (Sect. 4.5) we also make use of the positional reference frame of HIPPARCOS at epoch J1991.25 as defined by the revised HIPPARCOS catalogue (van Leeuwen 2007).

**Ephemerides.** Accurate barycentric ephemerides of *Gaia* and of all the major bodies in the solar system, as well as for some moons and minor planets, are needed in order to interpret the directions observed by *Gaia* in terms of astrometric parameters defined in the barycentric system. The solar system ephemeris used for EDR3 is the INPOP10e provided by the IMCCE (Fienga et al. 2016). The orbit of *Gaia* was determined at the Mission Operations Centre (MOC) located at ESOC (Darmstadt, Germany), using conventional Doppler and range tracking as well as Delta-Differential One-way Range (Delta-DOR) measurements, the latter using two tracking stations and calibrated by simultaneous observations of a quasar with known position.

The elementary along-scan (AL) astrometric observation is the precise time,  $t_{\text{obs}}$ , when the centre of a stellar image crosses the calibrated fiducial line on the CCD. This time is initially given as an on-board time (OBT), that is the number of nanoseconds counted by the on-board rubidium clock from an arbitrary origin, but must be transformed to the coordinate time (TCB) of the event before it can be used in the astrometric solution. This transformation, known as the time ephemeris, is derived from an analysis of time couples (the OBT of a signal generated on board and the reading of the ground-station clocks when it was received at the ground station), using a sophisticated model that takes into account *Gaia*'s position relative to the Earth, Earth orientation parameters, relativistic effects in the signal propagation, the influence of the Earth's troposphere, differences between the ground-station clocks and UTC, etc. (Klioner et al. 2017).

**Basic-angle corrector.** The basic angle monitor (BAM) is an interferometric device measuring short-term ( $\lesssim 1$  day)

variations of the basic angle at  $\mu\text{as}$  precision (Mora et al. 2016). BAM measurements are available since before the start of nominal operations and throughout the entire period of observations used for EDR3. They were processed off-line using the same methods as for DR2 (Sect. 2.4 in Lindegren et al. 2018), resulting in a table of basic-angle jumps (with the estimated time and amplitude of each jump) and, in between the jumps, a continuous function of time represented by a spline. The jumps and spline together define the function  $\Delta\Gamma(t)$  in Eq. (12).

### 3. Models

#### 3.1. Source model

The astrometric processing for *Gaia* EDR3 is based on a consistent theory of relativistic astronomical reference systems (Soffel et al. 2003). The primary coordinate system is the Barycentric Celestial Reference System (BCRS) with origin at the solar system barycentre and axes aligned with the International Celestial Reference System (ICRS). The time-like coordinate of the BCRS is the barycentric coordinate time (TCB). The *Gaia* relativity model (Klioner 2003, 2004) provides a rigorous general-relativistic modelling of astrometric observations.

For the purpose of deriving the main astrometric results in EDR3, it is assumed that all sources outside of the solar system move with uniform velocity relative to the solar system barycentre. Thus, non-linear motions caused by binarity and other perturbations are presently ignored, but will be taken into account in future *Gaia* releases. In the present model, which we refer to as the standard model of stellar motion (ESA 1997; Lindegren 2020a), the motion of the source is completely specified by six kinematic parameters, conventionally taken to be the standard five astrometric parameters ( $\alpha$ ,  $\delta$ ,  $\varpi$ ,  $\mu_{\alpha^*} = \mu_{\alpha} \cos \delta$ ,  $\mu_{\delta}$ ) and the radial velocity ( $v_r$ ). All parameters refer to the adopted reference epoch, which for the EDR3 astrometry is J2016.0 = JD 2457 389.0 (TCB) = 1 January 2016, 12:00:00 (TCB). This is exactly 0.5 Julian year (182.625 days) later than the reference epoch J2015.5 adopted for *Gaia* DR2.

In spite of the well-known fact that a large fraction of the stars in the solar neighbourhood are members of double and multiple systems, the standard model of stellar motion is very often a good model for the observed motions of stars in our Galaxy, and further away, at least over the relatively short time span covered by *Gaia*'s observations. In practice, only  $\sim 10\%$  of the stars may have proper motions that are noticeably non-linear over a few years (cf. Söderhjelm 2005). One reason for this is the extremely wide range of periods in physical systems, which means that most of them either have too long periods to show significant curvature over a short time, or they are so close and have such short periods that their photocentric wiggles are small and average out over a few years. The standard model is also very often an excellent approximation for extragalactic sources such as active galactic nuclei (AGNs) or quasars. The astrometric solution for *Gaia* relies heavily on the lucky circumstance that the motions of most point-like sources in the sky can be accurately represented by this simple model.

The standard model takes into account perspective acceleration through terms depending on the radial velocity  $v_r$ . In *Gaia* DR2 this effect was only considered for some 50 nearby HIP-PARCOS sources; for EDR3 it is taken into account whenever possible, using radial-velocity data from *Gaia*'s radial-velocity spectrometer (RVS; Sartoretti et al. 2018) as provided in *Gaia* DR2. For a small number of nearby stars (mainly white dwarfs), this was complemented with radial velocities from the literature.

Apart from the change in reference epoch and the more frequent use of radial velocity data, the source model for EDR3 is exactly the same as was used for DR2.

In the standard model, the radial velocity is needed, in addition to the usual five astrometric parameters, for a complete specification of the six-dimensional phase space vector of a nearby star. Because of this,  $v_r$  (or  $\mu_r = v_r \varpi / A_u$ , where  $A_u$  is the astronomical unit) is sometimes called the sixth astrometric parameter. This is potentially confusing in connection with the six-parameter solutions discussed in Sect. 2.3 and elsewhere, where the sixth parameter is the pseudocolour  $\hat{\nu}_{\text{eff}}$ , that is the astrometrically estimated effective wavenumber (colour) of the source. In contrast to the pseudocolour, the radial velocity is never estimated from *Gaia* data in any of the solutions discussed here, although it will be possible in the future for a small number of nearby high-velocity stars (Dravins et al. 1999).

#### 3.2. Attitude model

The attitude model for *Gaia* EDR3 is the same as was used for DR2, except that AL observations made in window class WC0b (see Sect. 3.3) were not used for the attitude determination. The attitude model includes a pre-computed AL corrective attitude that removes much of the rapid attitude irregularities created by micro-clanks and high-frequency thruster noise. We refer to Sect. 3.2 of Lindegren et al. (2018) for a description of the DR2 model.

#### 3.3. Calibration model

The astrometric calibration model for *Gaia* EDR3 is similar to the one used for DR2, as described in Sect. 3.3 of Lindegren et al. (2018), but with additional dependencies described below. The general principles of the calibration model are described in Sect. 3.4 of Lindegren et al. (2012), and only a few basic concepts are recalled here. At any time, the attitude represents a solid-body rotation from the celestial reference system to *Gaia*'s scanning reference system (SRS), nominally fixed with respect to the CCDs as viewed through the two FoVs (preceding and following). Within a FoV, directions with respect to the SRS are usually expressed by means of the field angles ( $\eta$ ,  $\zeta$ ), with origin at the nominal centre of the FoV (Fig. 3). According to the scanning law, stellar images traverse the FoV in the direction of decreasing  $\eta$  (at the AL rate of approximately 60 arcsec  $\text{s}^{-1}$ ) and at approximately constant  $\zeta$  (the AC rate is at most  $\pm 0.18$  arcsec  $\text{s}^{-1}$ ). The fundamental AL measurement used for the astrometry is the precise time when an image transits across a fiducial ‘‘observation line’’ line fixed to the CCD (Fig. 3, right). The astrometric calibration of the instrument (as opposed to the LSF and PSF calibrations by CAL) is essentially a specification of the location of the observation line in field angles, that is of the functions  $\eta(\mu)$  and  $\zeta(\mu)$ , where  $\mu$  is the AC pixel coordinate.

More precisely, the AL and AC calibration functions are written as the sums of the nominal calibrations and several ‘‘effects’’ that describe the dependence on various quantities, such as time, CCD, and FoV (see Eqs. (12) and (13)). The effects used in the EDR3 calibration model in the AF are listed in Table 2. The skymappers (SM1 and SM2 in Fig. 3) obtain a similar, but simpler, calibration. However, the SM observations are not at all used in the astrometric solution, and their calibration is not discussed in this paper.

Compared with the corresponding table for the DR2 model (Table 2 in Lindegren et al. 2018), Table 2 contains effects with

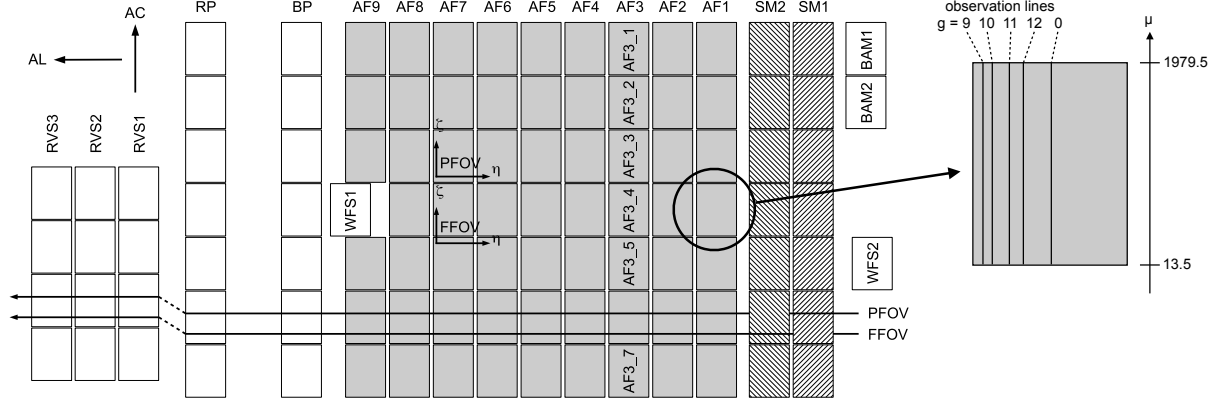


**Fig. 3.** Layout of CCDs in *Gaia*'s focal plane. Star images move from right to left in the diagram, as indicated in the lower part of the drawing by the nominal paths of two images, one in the preceding FoV (PFOV) and one in the following FoV (FFOV). The along-scan (AL) and across-scan (AC) directions are indicated in the top left corner. To the right, one of the CCDs is shown magnified, with the fiducial observation lines indicated for selected gates ( $g$ ). Also indicated is the AC pixel coordinate  $\mu$ , running from 13.5 to 1979.5 across the image area of each CCD. The sky-mappers (SM1, SM2) provide source image detection and FoV discrimination, but their measurements are not used in the astrometric solution. The astrometric field (AF1–AF9) provides accurate AL measurements and (for two-dimensional windows) AC positions. Other CCDs are used for the blue and red photometers (BP, RP), the radial-velocity spectrometer (RVS), wavefront sensing (WFS), and basic-angle monitoring (BAM). One of the CCD strips (AF3) illustrates the system for labelling individual CCDs by strip and row index. The origin of the field angles ( $\eta, \zeta$ ) is at different physical locations on the CCDs in the two fields. (Adapted from Lindegren et al. 2012.)

**Table 2.** Summary of the astrometric calibration model and number of calibration parameters in the astrometric solution for *Gaia* EDR3.

Effect ( $i$ ) and brief description	Basis functions $K_m(\tilde{\mu}, \tilde{t})$	$K_m$	$j$	$f$	Multiplicity of dependencies							Number of parameters			
					$n$	$g$	$b$	$w$	$v_{\text{eff}}$	$G$	$S$		$\phi$	$\Delta t$	$\zeta$
1 AL large-scale geometric	$lm = 00, 10, 20, 01$	4	310	2	62	–	–	4	–	–	–	–	–	–	615 040
2 AL medium-scale gate	$lm = 00, 10$	2	19	2	62	8	9	–	–	–	–	–	–	–	339 264
3 AL large-scale colour	$lm = 00, 01$	2	19	2	62	–	–	4	1	–	–	–	–	–	18 848
4 AL large-scale saturation	$lm = 00$	1	19	2	62	–	–	2	–	–	1	–	–	–	4 712
5 AL large-scale subpixel	$lm = 00$	1	19	2	62	–	–	4	–	–	–	2	–	–	18 848
6 AL large-scale CTI	$lm = 00$	1	19	2	62	–	–	4	–	–	–	–	4	–	37 696
7 AL large-scale AC rate	$lm = 00$	1	19	2	62	–	–	1	–	–	–	–	–	1	2 356
8 AC large-scale geometric	$lm = 00, 10, 20, 01$	4	19	2	62	–	–	2	–	–	–	–	–	–	18 848
9 AC large-scale gate	$lm = 00$	1	19	2	62	8	–	–	–	–	–	–	–	–	18 848
10 AC large-scale colour	$lm = 00$	1	19	2	62	–	–	2	1	–	–	–	–	–	4 712
11 AC large-scale magnitude	$lm = 00$	1	19	2	62	–	–	2	–	1	–	–	–	–	4 712
12 AC large-scale saturation	$lm = 00$	1	19	2	62	–	–	2	–	–	1	–	–	–	4 712

**Notes.** The column Basis functions lists the combinations of indices  $l$  and  $m$  used to model variations with AC coordinate on a CCD ( $\tilde{\mu}$ ) and with time within a time granule ( $\tilde{t}$ ). Multiplicity of dependencies gives the number of distinct functions or values for each dependency, or a dash if there is no dependency: basis functions ( $K_m$ , Eq. (5)), granule index ( $j$ ), field index ( $f$ ), CCD index ( $n$ ), gate ( $g$ ), stitch block ( $b$ ), window class ( $w$ ), effective wavenumber ( $v_{\text{eff}}$ ), magnitude ( $G$ ), saturation ( $S$ ), subpixel phase ( $\phi$ ), time since last charge injection ( $\Delta t$ ), and AC scan rate ( $\zeta$ ). The last column is the product of multiplicities, equal to the number of calibration parameters for the effect. The SMs are not considered here.

several new dependencies ( $S, \phi, \Delta t, \zeta$ ). Their introduction in the model was motivated by systematic trends seen in the residuals from preliminary solutions, in which the calibration model did not include the effects. The complete set of dependencies is as follows.

- AC pixel coordinate  $\mu$  on the CCD, which is a continuous value running from 13.5 to 1979.5 across the AC extent of the CCD image area (Fig. 3). The offset by 13 pixels allows for the presence of pre-scan pixel data.

- Time  $t$ , divided into granules such that  $t_j \leq t < t_{j+1}$  in the granule indexed by  $j$ . Two different time axes are used, with 310 and 19 granules spanning the length of the data; the typical duration of the granules is, respectively, about 3 d and 63 d.

- FoV index  $f$ , specifying preceding or following FoV. We use the convention  $f = +1$  in the PFOV and  $f = -1$  in the FFOV.

- CCD  $n$ , with 62 different values in the astrometric field.
- Gate  $g$ , taking eight different values with  $g = 0$  for ungated observations (Fig. 4). The number of active TDI lines is 4500 for  $g = 0$ , 2900 ( $g = 12$ ), 2048 ( $g = 11$ ), 1024 ( $g = 10$ ), 512 ( $g = 9$ ), 256 ( $g = 8$ ), 128 ( $g = 7$ ), and 16 ( $g = 4$ ). Gates 1–3, 5, and 6 are not used in normal operations.

- Stitch block  $b$ , with nine different values in the AC direction of a CCD.  $b$  is uniquely defined by the AC pixel coordinate through  $b = \lfloor (\mu + 128.5)/250 \rfloor$ , where  $\lfloor \cdot \rfloor$  is the floor function.

- Window class  $w$ , with four values. In the DR2 calibration model, three window classes WC0, WC1, and WC2 were used, approximately corresponding to magnitude ranges  $G \lesssim 13$ ,  $13 \lesssim G \lesssim 16$ , and  $16 \lesssim G$ , respectively. (The WC represents the CCD sampling scheme chosen at detection time, depending mainly on the real-time estimate of the magnitude derived from



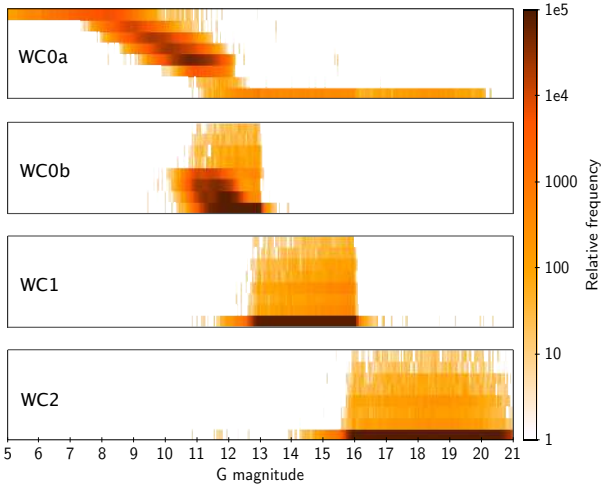


**Fig. 4.** Relative frequency of observations in the various combinations of window class and gate, as a function of magnitude. The four blocks represent the four window classes (WC); within each WC the eight stripes represent (from top to bottom) gate number 4, 7, 8, 9, 10, 11, 12, and 0. The graph was constructed from a random 1% sample of the AF observations of the primary sources. The faint sources observed in WC0a at gate 0 are the Calibration Faint Stars, a small fraction of faint observations receiving full-pixel resolution windows for calibration purposes (Gaia Collaboration 2016a).

the SM observation, but also on several other factors. There is consequently no strict relation between the mean calibrated  $G$  magnitude, given in the catalogue, and the WC.) In the EDR3 model, WC0 was further subdivided into WC0a (for  $G \lesssim 11$ ) and WC0b (for  $11 \lesssim G \lesssim 13$ ), see Fig. 4.

– Effective wavenumber  $\nu_{\text{eff}}$  is the photon-weighted inverse wavelength, calculated from the BP and RP spectra in the photometric processing (De Angeli et al., in prep.) and expressed in  $\mu\text{m}^{-1}$ . The cyclic processing scheme adopted by DPAC implies that the  $\nu_{\text{eff}}$  used for the EDR3 astrometry was generated in the preceding cycle, corresponding to DR2 photometry, and is sometimes missing or inconsistent with the EDR3 photometry. The actual values used for the astrometry (and IDU pre-processing) is given in the Gaia Archive as `nu_eff_used_in_astrometry`. For sources without a reliable  $\nu_{\text{eff}}$  a special calibration was employed (step 6 in Sect. 4.1).

– Magnitude  $G$ : like the effective wavenumber, the magnitude used in the astrometric processing was derived from DR2, but since the differences are generally small and only the (less critical) AC calibration depends on  $G$ , the actual value used is not given in the Archive.

– Saturation  $S$ : this is a flag produced by the IPD as part of the IDU pre-processing. It is set to 1 if the raw observed sample exceeds a pre-defined conservative threshold, as determined from early mission data, for the CCD column and sample binning; otherwise  $S = 0$ . The astrometric effects of the saturation are only calibrated for WC0a and WC0b.

– Subpixel phase  $\phi$ : this is  $2\pi$  times the fractional part of the precise observation time  $t$ , as determined by the IPD and expressed in TDI periods of on-board time. (The TDI period is the time it takes to shift the charges on the CCDs by one pixel AL, or approximately 0.982 ms.) Inaccuracies in the LSF and PSF calibrations used for the IPD may result in systematic AL errors that are periodic functions of  $\phi$ .

– Time since the last charge injection  $\Delta t$ : to minimise the effects of charge transfer inefficiency (CTI) in the CCDs, charge

injections are made at regular time intervals of 2000 TDI periods. CTI may cause systematic AL shifts of the image centroids, which increase with  $\Delta t$ .

– Across-scan (AC) rate  $\dot{\zeta}$ : the nominal scanning law of Gaia (Gaia Collaboration 2016a) produces a quasi-periodic ( $\approx 6$  h period) variation of the AC rate, with an amplitude of approximately  $173 \text{ mas s}^{-1}$ . Imperfections in the PSF modelling may result in systematic AL errors that depend on the AC rate. This dependence is only calibrated for observations in WC0b using gates 11, 12, and 0 (that is, for a CCD exposure time of about 2.0, 2.8, or 4.4 s).

Within a time granule, the variation with  $t$  and  $\mu$  is modelled as a linear combination of basis functions

$$K_{lm}(\tilde{\mu}, \tilde{t}) = \tilde{P}_l(\tilde{\mu})\tilde{P}_m(\tilde{t}), \quad (5)$$

where  $\tilde{P}_l(x)$ ,  $\tilde{P}_m(x)$  are the shifted Legendre polynomials<sup>3</sup> of degree  $l$  and  $m$ ,  $\tilde{\mu} = (\mu - 13.5)/1966$  is the normalised AC pixel coordinate, and  $\tilde{t} = (t - t_j)/(t_{j+1} - t_j)$  the normalised time within granule  $j$ . The third and fourth columns in Table 2 list the combination of indices  $l$  and  $m$  used for a particular effect and the number of basis functions  $K_{lm}$ . Most of the effects only use  $lm = 00$ , meaning that the effect is modelled as constant with  $t$  and  $\mu$  for a given combination of the other indices and variables.

Each combination of indices  $l$ ,  $m$ ,  $j$ ,  $f$ ,  $n$ ,  $g$ ,  $b$ , and  $w$  indicated in Table 2 is a “calibration unit” and receives an independent calibration. Within a calibration unit, effect  $i$  is a linear combination of products  $K_{lm}(\tilde{\mu}, \tilde{t})\Psi_k^{(i)}(x)$ , where  $K_{lm}$  describes the dependence on  $t$  and  $\mu$  according to Eq. (5), and  $\Psi_k^{(i)}(x)$  ( $k = 0, 1, \dots$ ) describe the dependence on some other variable  $x$ , which could be  $\nu_{\text{eff}}$ ,  $G$ ,  $S$ ,  $\phi$ ,  $\Delta t$ , or  $\dot{\zeta}$ . The relevant functions are:

$$\Psi_0^{(3,10)}(\nu_{\text{eff}}) = \nu_{\text{eff}} - 1.43 \mu\text{m}^{-1}, \quad (6)$$

$$\Psi_0^{(11)}(G) = G - 12.6, \quad (7)$$

$$\Psi_0^{(4,12)}(S) = S, \quad (8)$$

$$\Psi_0^{(5)}(\phi) = \cos \phi, \quad \Psi_1^{(5)}(\phi) = \sin \phi, \quad (9)$$

$$\Psi_k^{(6)}(\Delta t) = a_k - \exp(-\Delta t/\tau_k), \quad k = 0 \dots 3, \quad (10)$$

$$\Psi_0^{(7)}(\dot{\zeta}) = |\dot{\zeta}|^2. \quad (11)$$

The function  $\Psi_0^{(11)}(G)$  in Eq. (7) is only used for ungated AC observations; otherwise, it is set to 1. Equation (9) describes a periodic variation with subpixel phase  $\phi$ . In Eq. (10), the variation with time since the last charge injection  $\Delta t$  is assumed to be a linear combination of four exponentials, with e-folding times  $\tau_k = 10, 100, 500,$  and  $2000$  TDI periods. The constants  $a_k = (\tau_k/2000)[1 - \exp(-2000/\tau_k)]$  are such that the mean value of  $\Psi_k^{(6)}(\Delta t)$  over  $0 \leq \Delta t \leq 2000$  is zero. This means that the mean displacement of the images caused by the CTI is not taken out by this calibration, only its variation with  $\Delta t$ . The resulting calibration parameters are thus mainly interesting as diagnostics of the effect (Fig. A.8). The quadratic dependence on the AC rate  $\dot{\zeta}$  in Eq. (11) models a possible bias caused by the AC smearing of the PSF; this effect was not well modelled in the PSF calibration for EDR3 (cf. Sect. 6.4 and Appendix B). Formally,  $\Psi^{(1,2,8,9)} = 1$  for the effects that only depend on  $t$  and  $\mu$ .

<sup>3</sup> The shifted Legendre polynomials  $\tilde{P}_n(x)$  are related to the (ordinary) Legendre polynomials  $P_n(x)$  by  $\tilde{P}_n(x) = P_n(2x - 1)$ . Specifically,  $\tilde{P}_0(x) = 1$ ,  $\tilde{P}_1(x) = 2x - 1$ , and  $\tilde{P}_2(x) = 6x^2 - 6x + 1$ . The shifted Legendre polynomials are orthogonal on  $0 \leq x \leq 1$ .

The complete AL calibration model is

$$\eta(\mu, t, v_{\text{eff}}, \dots) = \eta_{ng}^{(0)}(\mu) + \frac{f}{2} \Delta\Gamma(t) + \sum_{i=1}^7 \sum_{l,m,k} \Delta\eta_{lmk}^{(i)} K_{lm} \Psi_k^{(i)} + \delta\eta(f, t, \eta, \zeta), \quad (12)$$

where the first term is the nominal location of the fiducial observation line for CCD  $n$ , gate  $g$  (Eq. (14) in Lindegren et al. 2012); the second contains the basic angle correction  $\Delta\Gamma(t)$  derived from BAM data (Sect. 2.4); the third is the sum of the seven effects  $i$  in the upper part of Table 2, with calibration parameters  $\Delta\eta_{lmk}^{(i)}$ ; and the last term is the spin-related distortion model fitted as global parameters (Sect. 3.4). For brevity, the dependences on  $f$ ,  $n$ ,  $g$ ,  $b$ , and  $w$  and the arguments of  $K_{lm}$  and  $\Psi_k^{(i)}$  have been suppressed. This gives a total of 1 036 764 AL parameters (not counting the spin-related distortion parameters), which is more than three times as many as used for the DR2 calibration model (see Table 1 in Lindegren et al. 2018). Besides the longer time interval covered by the data, this reflects the more complex modelling made necessary (and possible) thanks to the generally improved quality of the input data and resulting solution. Several new effects have been introduced (saturation, subpixel, CTI, and AC rate), and the AL large-scale geometric calibration now depends also on the window class. Some of these effects should eventually be taken out by the LSF and PSF calibrations, but that was not yet possible in the present cycle.

The AC calibration model is

$$\zeta(\mu, t, v_{\text{eff}}, \dots) = \zeta_{fng}^{(0)}(\mu) + \sum_{i=8}^{12} \sum_{l,m,k} \Delta\zeta_{lmk}^{(i)} K_{lm} \Psi_k^{(i)} + \delta\zeta(f, t, \eta, \zeta), \quad (13)$$

where  $\zeta_{fng}^{(0)}(\mu)$  is the nominal calibration and  $\Delta\zeta_{lmk}^{(i)}$  the calibration parameter for the five effects in the bottom part of Table 2. The last term is the spin-related distortion in AC; but as explained in Sect. 3.4 this is not used for EDR3, and is therefore put within square brackets in Eq. (13). This gives a total of 51 832 AC calibration parameters, which is 10% smaller than in DR2, in spite of the longer time period covered. The main reason for this is that the dependences on time and AC coordinate were found to be overly complicated in DR2 and have been simplified.

Selected results of the astrometric calibration are given in Appendix A.4.

### 3.4. Spin-related distortion model

Thermo-mechanical perturbations of the instrument over time scales close to and below the rotational period of 6 h present a special problem for the AGIS calibrations. Such variations will be called “quick” below. It is known that it is impossible to fully calibrate the quick variations of the instrument (Butkevich et al. 2017). The reason for this is a degeneracy between the source parameters, attitude parameters, and calibration parameters for the quick variations of the instrument. This is known as the VBAC degeneracy (Velocity error and effective Basic Angle Calibration)<sup>4</sup>. A special case of this is the well-known

<sup>4</sup> The mention of velocity here may seem surprising. For an astrometric satellite such as *Gaia*, the observational effects of a small error in the translational velocity, as used in the modelling of stellar aberration, is found to be indistinguishable from a certain combination of errors in the attitude and in the basic angle. This aspect of the data processing plays no role for EDR3, where velocity is taken to be known (Sect. 2.4).

degeneracy between the global parallax zero point and a specific form of basic-angle and attitude variations (Butkevich et al. 2017), but the VBAC degeneracy is much more general: Any time-dependent distortion of the celestial positions is observationally indistinguishable from some specific combination of attitude errors and quick instrument variations. In the design considerations for *Gaia* it was indeed a fundamental requirement that the instrument must either be extremely stable on time scales shorter than a few times the spin period, or have the means to monitor the variations continuously to a very high precision.

However, the VBAC degeneracy does not imply that arbitrary quick instrument variations are degenerate with the source and attitude parameters. On the contrary, most such variations are not degenerate, and therefore in principle possible to calibrate from the astrometric observations themselves, that is, without the need for special procedures or metrology devices like the BAM. Over the last decade, a considerable effort has been put into investigating how, and to what extent, quick variations of the *Gaia* instrument can be calibrated from the astrometric observations. The spin-related distortion model presented here is a limited version of more general models that may be used for future *Gaia* releases. It nevertheless represents a significant advance over the DR2 model (Sect. 3.4 in Lindegren et al. 2018). Although the distortion model logically belongs to the instrument calibration model, it is fitted as part of the global block in AGIS for purely implementation-technical reasons.

#### 3.4.1. General model

We begin by formulating the spin-related distortion model in its most general form. At any moment of time an arbitrary distortion of the AL and AC field angles  $(\eta, \zeta)$  for a source in a given FoV  $f$  can be represented as a two-dimensional expansion over a family of orthogonal functions  $\Phi_{lm}(\eta, \zeta)$ :

$$\delta\eta(f, t, \eta, \zeta) = \sum_{l \geq 0} \sum_{m \geq 0} \delta\eta_f^{lm}(t) \Phi_{lm}(\eta, \zeta), \quad (14)$$

$$\delta\zeta(f, t, \eta, \zeta) = \sum_{l \geq 0} \sum_{m \geq 0} \delta\zeta_f^{lm}(t) \Phi_{lm}(\eta, \zeta). \quad (15)$$

For the nominally rectangular AF of *Gaia*, a convenient set of orthogonal functions are the products of the Legendre polynomials  $P_k(x)$  for the AL and AC coordinates:

$$\Phi_{lm}(\eta, \zeta) = P_l(\tilde{\eta}) P_m(\tilde{\zeta}), \quad (16)$$

where  $\tilde{\eta}$  and  $\tilde{\zeta}$  are the field angles  $\eta$  and  $\zeta$  linearly scaled to the interval  $[-1, 1]$ . (Although not apparent in these equations, the scaling of  $\zeta$  is actually different in the two FoVs, owing to the offset of the AC origins indicated in Fig. 3.)

We use Eqs. (14) and (15) to model the spin-related distortion terms in Eqs. (12) and (13). Their time-variations are defined by the functions  $\delta\eta_f^{lm}(t)$  and  $\delta\zeta_f^{lm}(t)$  to be specified below.

Full-scale simulations of the AGIS solution have shown that the terms in Eqs. (14) and (15) with  $l + m \geq 1$  are not degenerate with the source parameters and attitude, and can therefore safely be determined from the observations. For example, simulated variations in which  $\delta\eta_f^{lm}(t)$  and  $\delta\zeta_f^{lm}(t)$  for  $1 \leq l + m \leq 5$  were represented as B-splines, with a knot interval of 10 min and random coefficients, could be completely recovered with no rank-deficiency and only a moderate slowdown of the convergence of the iterative solution. The terms with  $l = m = 0$ , on the other hand, involve the VBAC degeneracy, and the time variation of these terms need to be chosen with care in order not to jeopardise the source parameters. It is therefore natural to split the

further specification of the general spin-related distortion model in two parts, corresponding to VBAC (for  $l = m = 0$ ) and FOC (for  $l + m \geq 1$ ). Here, FOC stands for Focal length and Optical distortion Calibration, since the calibration for  $l + m \geq 1$  obviously covers also a variation of the focal length of the instrument.

The general model in Eqs. (14) and (15) can also describe slow variations of the instrument and is in principle degenerate with certain parts of the calibration model described in Sect. 3.3. As this degeneracy does not involve the source parameters it is harmless for the astrometry, but since it could slow down the convergence of the AGIS iterations it should nevertheless be avoided if practically feasible. One such case is the near-degeneracy mentioned below between effect 7 in Table 2 and the Fourier terms of order  $p = 2$  in Eqs. (17) and (19).

### 3.4.2. FOC

Because the FOC calibration ( $l + m \geq 1$ ) has no degeneracy with the source and attitude parameters, we are quite free to choose the maximum degree  $l + m$  of the basis functions  $\Phi_{lm}(\eta, \zeta)$  and the parametrisation of the time dependency of the functions  $\delta\eta_f^{lm}(t)$  and  $\delta\zeta_f^{lm}(t)$ . Of course, it is always necessary to limit the degree and time resolution so that the number of parameters is reasonable in relation to the number of observations, keeping the overall solution numerically and practically tractable. For example, because the AF has nine strips of CCDs (see Fig. 3), it is not numerically feasible to have the AL degree  $l > 9$ . Numerous test solutions using EDR3 data were made to explore some of the many possible options, and the configuration finally adopted for AGIS 3.2 is in some sense the best one found in the limited time available.

One conclusion from the test solutions was that the FOC correction in AC does not bring any improvement at this stage and it is therefore not used for EDR3; hence the bracketed term in Eq. (13). It was also found that the polynomials in Eq. (14) can be restricted to  $1 \leq l + m \leq 3$ , which gives 18 coefficients  $\delta\eta_f^{lm}(t)$  to be considered (nine per FoV). Similarly to the AL calibration model in Sect. 3.3, it was found necessary to determine FOC separately for each window class. For WC0a, WC1, and WC2, the ten coefficients with  $1 \leq l + m \leq 2$  were determined as cubic splines with a knot interval of 20 min. The remaining eight coefficients with  $l + m = 3$  were fitted as Fourier polynomials

$$\delta\eta_f^{lm}(t) = d(t)^{-2} \sum_{p=1}^8 (c_{fplm} \cos p\Omega(t) + s_{fplm} \sin p\Omega(t)), \quad (17)$$

where  $d(t)$  is the Sun–*Gaia* distance in au,  $\Omega(t)$  is the heliotropic spin phase (Lindegren et al. 2018), and  $c_{fplm}$  and  $s_{fplm}$  are the free parameters fitted to the data. The scaling by  $d(t)^{-2}$  here and in the following equations accounts for the variation in solar irradiance. For WC0b, all 18 coefficients  $\eta_f^{lm}(t)$  were fitted as Fourier polynomials, as in Eq. (17), but omitting the terms with  $p = 2$  to avoid the near-degeneracy with effect 7 in Table 2. Furthermore, all Fourier polynomials for FOC were fitted independently for the two time intervals before and after OBMT 4513 rev. That moment of time (one of the gaps in Table 1) was found to be a boundary between slightly different behaviours of the residuals in test solutions; ultimately, this behaviour can be traced back to a particular change of LSF and PSF models in CALIPD 3.1 at that moment. The resulting FOC model has a total of 2 033 184 parameters.

### 3.4.3. VBAC

The terms in Eqs. (14) and (15) with  $l = m = 0$  represent the distortion averaged over each FoV. It is readily seen that this is equivalent to a combination of four time dependent variations, namely, (i) of the AL attitude by  $\frac{1}{2}(\delta\eta_{+1}^{0,0} + \delta\eta_{-1}^{0,0})$ ; (ii) of the AC attitude in the PFoV by  $\delta\zeta_{+1}^{0,0}$ ; (iii) of the AC attitude in the FFoV by  $\delta\zeta_{-1}^{0,0}$ ; and (iv) of the basic angle by  $\delta\Gamma = \delta\eta_{+1}^{0,0} - \delta\eta_{-1}^{0,0}$ . The flexibility of the attitude modelling means that the first three variations are completely degenerate with the attitude determination, and should not be further considered in the VBAC model. Therefore, the only variation to consider for  $l = m = 0$  is a time-dependent basic angle variation,  $\delta\Gamma(t)$ .

$\delta\Gamma(t)$  can be regarded as an additive correction to the basic angle variation  $\Delta\Gamma(t)$  in Eq. (12) that comes from the analysis of BAM data (Sect. 2.4). It should be recalled that  $\Delta\Gamma(t)$  includes both basic angle jumps (due to sudden structural changes in the optics) and a smooth representation of the basic angle variations between jumps, including a very good approximation of the quick variations. However, because the CCDs for the BAM are located outside of the AF (Fig. 3), we cannot assume that the variations measured with the BAM are fully representative for the whole FoV – indeed, in the presence of FOC distortion this is not to be expected. Moreover, the BAM device itself may be subject to perturbations that are not relevant for the astrometric observations. For these reasons it is highly desirable to calibrate as much as possible of the basic angle variations directly from the astrometric observations, which can be done with VBAC. Owing to the VBAC degeneracy there are nevertheless components of the basic angle variations that cannot be determined from the observations, and the BAM signal remains indispensable as the only handle we may have on those components.

For EDR3, the same representation of  $\delta\Gamma(t)$  was used as for DR2 (Eq. (10) in Lindegren et al. 2018), but split in two parts,

$$\delta\Gamma(t) = \delta\Gamma_A(t) + \delta\Gamma_B(t), \quad (18)$$

with

$$\begin{aligned} \delta\Gamma_A(t) = d(t)^{-2} \sum_{p=2}^8 [\delta C_{p,0} + (t - t_{\text{ep}})\delta C_{p,1}] \cos p\Omega(t) \\ + d(t)^{-2} \sum_{p=1}^8 [\delta S_{p,0} + (t - t_{\text{ep}})\delta S_{p,1}] \sin p\Omega(t) \end{aligned} \quad (19)$$

and

$$\delta\Gamma_B(t) = d(t)^{-2} [\delta C_{1,0} + (t - t_{\text{ep}})\delta C_{1,1}] \cos \Omega(t). \quad (20)$$

Here  $d(t)$  and  $\Omega(t)$  have the same meaning as in Eq. (17),  $t_{\text{ep}} = \text{J2016.0}$ , and  $\delta C_{p,q}$ ,  $\delta S_{p,q}$  are the constant coefficients determined from the data. The split in Eq. (18) is motivated by the near-degeneracy of  $\delta C_{1,0}$  with a global parallax shift (Butkevich et al. 2017; Lindegren et al. 2018), which necessitates a special treatment of this term; this is deferred till Sect. 3.4.4. The parameter  $\delta C_{1,1}$  is included in  $\delta\Gamma_B(t)$  only because it naturally belongs together with  $\delta C_{1,0}$ ; it is not strongly correlated with other parameters and could instead have been fitted with the other VBAC parameters in Eq. (19).

The representation of  $\delta\Gamma_A(t)$  in Eq. (19) contains 30 parameters describing linear variations of the  $d(t)^{-2}$ -scaled Fourier coefficients in  $\Omega(t)$ . Analysis of the test AGIS solutions and



their residuals has shown that the effective basic angle variations obtained with this model are substantially different for the different window classes. A separate set of Fourier coefficients was therefore fitted for each window class. Moreover, similarly as for the Fourier coefficients in the FOC model, separate fits were made for the time intervals before and after OBMT 4513 rev, and the coefficients for  $p=2$  were omitted for WC0b. The resulting model for  $\delta\Gamma_A(t)$  has a total of 232 parameters.

#### 3.4.4. Treatment of the near-degeneracy with parallax ( $\delta C_{1,0}$ )

Here we consider the VBAC correction  $\delta\Gamma_B(t)$  in Eq. (20), containing the two additional parameters  $\delta C_{1,0}$  and  $\delta C_{1,1}$ . Unlike the parameters in  $\delta\Gamma_A(t)$ , which were fitted per window class and separately before and after OBMT 4513 rev, there is only a single set of these two parameters. They are fitted using all data except WC0b.

As already mentioned, the parameter  $\delta C_{1,0}$  cannot be easily fitted in an iterative solution like AGIS because it is highly correlated to a global shift of all parallaxes (Butkevich et al. 2017). However, this also means that if the correction  $\Delta\Gamma(t)$  to the basic angle derived from BAM data has an error described by  $\delta C_{1,0}$ , there will be a global shift of the parallaxes. Owing to the profound scientific importance of the parallax zero point, every effort should be made to avoid such an error. To this end a method has been developed to calibrate  $\delta C_{1,0}$  directly from the astrometric observations of *Gaia*. The method was thoroughly tested in a series of detailed end-to-end simulations of the iterative solution, which demonstrated the feasibility of the method and probed the limits of its applicability. It was tested with cycle 2 data (but not used in the solution for *Gaia* DR2), and finally employed in the primary astrometric solution for EDR3. Full details of the method will be published elsewhere; here we describe only its most important elements.

The possibility to fit  $\delta C_{1,0}$  is based on the small but not completely negligible differences between heliocentric and barycentric quantities, and the fact that the solar irradiance and parallax factor scale differently with the varying distance from the Sun or solar system barycentre. Based on physical considerations, the model for the basic angle variations in Eqs. (19) and (20) scales as  $d(t)^{-2}$  and is periodic in  $\Omega(t)$ , where  $d(t)$  and  $\Omega(t)$  are heliocentric, that is, reckoned with respect to the Sun. On the other hand, the AL parallax effect depends on the corresponding barycentric quantities  $d_b(t)$  and  $\Omega_b(t)$  measured relative to the solar system barycentre. More precisely, the ability to determine absolute parallaxes depends on the AL parallax factor being different in the two FoVs (see Fig. 2 in *Gaia* Collaboration 2016a). Relevant for the parallax zero point is therefore the differential AL parallax factor  $d_b(t) \sin \xi_b(t) \cos \Omega_b(t)$  (see footnote 9 in Appendix B), where  $\xi_b(t)$  is the angle between *Gaia*'s spin axis and the direction to the barycentre. Thus, in our model for  $\delta\Gamma(t)$ , only the term proportional to  $\cos \Omega(t)$ , that is the one containing  $\delta C_{1,0}$ , has a strong correlation with the parallax zero point. The differences between the heliocentric and barycentric quantities, of the order of 0.01 au and 0.01 rad, and the annual variations in  $d$  and  $d_b$ , by about  $\pm 1.7\%$ , all contribute towards a decorrelation of the parallax zero point from  $\delta C_{1,0}$ .

For the actual cycle 3 data, the correlation coefficient between  $\delta C_{1,0}$  and the parallax zero point is  $\approx 0.99992$ . Such a high degree of correlation (collinearity) in a least-squares estimation problem would normally be considered crippling, but it need not be so if the number of observations is very high, which it is in this case, and the modelling is sufficiently accurate, which we strive for. If all the  $\sim 85$  million unknowns

in the primary astrometric solution could be obtained by direct solution of the normal equations, a valid solution for  $\delta C_{1,0}$  would be obtained because the full normal equations take into account the correlations among all parameters. However, we are forced to use iterative solution methods, and it turns out that the introduction of  $\delta C_{1,0}$  in AGIS effectively prevents the convergence of the block-iterative solution in its original form. The non-convergence is however not caused by the strong correlation itself, but by the circumstance that the correlated parameters are in different blocks. In AGIS the different blocks of source, attitude, calibration, and global parameters are treated as independent least-squares problems in a given iteration, thus ignoring correlations between, for example, the global block (containing  $\delta C_{1,0}$ ) and the source blocks (containing the parallaxes) when updates for the next iteration are computed.

We nevertheless found a way to obtain a converged solution including  $\delta C_{1,0}$ , by using a special option in the global block of AGIS, called “consider parameters”. This device was originally introduced for a different purpose<sup>5</sup>, but here it is used to allow the AGIS iterations to converge in a reasonable time. This particular use of consider parameters has been thoroughly tested in simulations, and we are therefore confident in its fundamental correctness. Briefly, here is how it works. In the global block, we introduce three more unknowns (consider parameters) that are strongly correlated with  $\delta C_{1,0}$ , namely one additive constant to all parallaxes, and two parameters for certain variations of the attitude (see Eq. (15) in Butkevich et al. 2017). All three consider parameters are fully degenerate with the parallaxes and the ordinary attitude parameters, but because their updates are ignored in each iteration they remain at their initial zero values and do not affect the computation of the right-hand side of the observation equations (the residuals). Their inclusion in the left-hand side of the global block does however modify the updates to the regular global parameters, including  $\delta C_{1,0}$ , and this is what allows the iterations to converge. Because the three consider parameters remain at zero, it does not matter that they are degenerate with other parameters, and the solution, after convergence, must be the same as a solution without them – if such a solution could be obtained by some different algorithm. The role of the consider parameters in the block-iterative primary AGIS solution can formally be understood as a modification of the preconditioner of the adjustment scheme (e.g. Saad 2003; Bombrun et al. 2012).

The condition number of the normal matrix for the fit of  $\delta C_{1,0}$  is about  $10^5$ , so its inversion using normal 64-bit arithmetic is quite accurate. Although somewhat delicate, the fit works in practice and delivers a reasonably stable value of  $\delta C_{1,0}$  after a number of AGIS iterations. The formal uncertainty of  $\delta C_{1,0}$  from the fit is about  $1 \mu\text{as}$ . However, the fragile character of the fitting of  $\delta C_{1,0}$  necessitates certain precautions: (i)  $\delta C_{1,0}$  and the consider parameters should only be introduced at the very last stage of the AGIS iterations (see Table 3); (ii) only AL data should be used in the fit; (iii) in EDR3, the observations in window class

<sup>5</sup> The term “consider parameter” has various meanings in the literature. Here we refer to a parameter that is included in the estimation of updates to the current parameter values, but for which no actual update is applied to the parameter. The consider parameter thus remains at its original value (in this case zero), but the solution computes updates to the other parameters, and uncertainties and correlations among all parameters, exactly as if the consider parameter had been included in the fit. As the name suggests, consider parameters are intended to help the researcher decide whether a particular signal, modelled by the consider parameters, exists in the data, and how the covariance of the solution would be affected if they were included in the fit.



**Table 3.** Iteration sequences for the primary solutions of AGIS 3.2.

Iterations	Blocks active	Algorithm	Remark
1–27	SAC	Hybrid	Warm up run
1–89	SACG	Hybrid	$\delta C_{1,0} = 0$
90–126	SACG	Simple	$\delta C_{1,0} = 0$
127–141	SACG	Hybrid	$\delta C_{1,0}$ free
142–165	SAG	Simple	$\delta C_{1,0}$ free, ad hoc corr.
166–181	C	Simple	Step 6 (calibration $C'$ )

**Notes.** Columns 2 and 3 describe the AGIS configuration for the sequence of iterations in the first column (see text).  $\delta C_{1,0}$  is the global parameter discussed in Sect. 3.4.4. Iterations 1–165 correspond to step 5 in Sect. 4.1. Between iterations 141 and 142 the ad hoc correction to the calibration parameters for the bright sources (Sect. 4.5) was applied, after which the calibration was not updated. Iterations 166–181 correspond to step 6, computing the special calibration  $C'$  needed for sources with default colour in IPD.

WC0b have larger systematics and were therefore omitted from the fit.

In the primary AGIS solution for EDR3,  $\delta C_{1,0}$  shifted the parallax zero point by about  $+20 \mu\text{as}$  compared with the same solution without  $\delta C_{1,0}$ , and by about  $+10 \mu\text{as}$  compared with DR2. The global parallax zero point of EDR3 is about  $-17 \mu\text{as}$  (Lindegren et al. 2021). Although the inclusion of  $\delta C_{1,0}$  in the global model for EDR3 did not bring the global parallax zero point to zero, the partial success of the method is very encouraging and fosters the hope that the zero point issue can be resolved, at the level of a few  $\mu\text{as}$ , in future releases that will benefit from much improved calibration models.

## 4. Astrometric solutions

### 4.1. Main steps of the solutions

The tasks labelled AGIS 3.1 and AGIS 3.2 in Fig. 1 each consists of several steps, the most important ones being:

1. Preprocess the input data (transits) from IDU: this includes filtering (removing transits that are unmatched or of poor quality according to IPD flags, or outside the specified time interval) and sorting the transits by position. Sorting uses the healpix index (Górski et al. 2005) encoded in the `source_id`.

2. Select a set of primary sources to ensure a sufficient density of well-behaved sources with a good coverage in magnitude and colours.

3. Fit an initial attitude for the required time interval, using source parameters from a previous cycle or phase; also define data gaps where transits are missing or of poor quality.

4. Generate the corrective attitude from rate data as described in Sect. 3.2 of Lindegren et al. (2018).

5. Calculate a primary solution by simultaneously estimating source (S), attitude (A), calibration (C), and global (G) parameters in an iterative least-squares solution involving only the primary sources. See Sect. 4.2 for a brief explanation.

6. Compute a separate set of calibration parameters ( $C'$ ) for sources where IPD used the default colour  $\nu_{\text{eff}}^{\text{def}} = 1.43 \mu\text{m}^{-1}$ . This calibration is based on a subset of the primary sources where image parameters were determined by IPD using both the actual colours and the default value.

7. Calculate secondary solutions for all sources (Sect. 4.3). The computation is equivalent to the S block in step 5, except that sources with default colour obtain six-parameter solutions

using calibration  $C'$ . In this step the acceptance criteria detailed in Sect. 4.4 are checked and, if necessary, a fallback solution computed.

8. Postprocess the results: this includes calculating various statistics such as the renormalised unit weight error (RUWE).

9. Regenerate attitude and calibration data for use by downstream processes such as PhotPipe. This fills some time gaps and intervals (including the EPSL) that were excluded for the astrometry, but where the observations may still be useful for other processes. The skymapper (SM) geometry is also calibrated at this point. Although the SM observations are not used in the astrometric solution, they are needed in downstream processes.

10. Regenerate attitude and astrometric calibration data for the LSF and PSF calibrations in the CALIPD of the next processing cycle or phase. This uses the same calibration model as for the primary solution, but including only the purely geometric part of the model, that is the effects numbered 1, 2, 8, and 9 in Table 2. This is known as the “NoCoMaRa” calibration: no dependency on colour, magnitude, or rate (as opposed to the normal, “CoMaRa”, calibration including all the effects). The rationale for this is that all dependencies on colour, magnitude, AC rate, saturation, subpixel phase, and CTI effects should ultimately be accounted for by the LSF and PSF calibrations, so that AGIS can be a purely geometric solution. This goal will never be reached if the AGIS calibration used for the LSF and PSF calibrations already removes (part of) the dependencies. By using NoCoMaRa for the LSF and PSF calibrations, the latter processes see the full extent of the dependencies. (In principle the attitude generated in steps 5 and 9 is already purely geometric, but owing to the non-orthogonality of some CoMaRa and NoCoMaRa effects, the best-fitting geometric attitude is slightly different for the two calibrations.) The NoCoMaRa calibration and attitude are not used by any downstream processes, only by IDU.

11. Export all results to the main database, making them available to other processes.

The same steps were executed in AGIS 3.1 and 3.2, but with many differences in the details. In particular, the selection of primary sources and the calibration models were different in the two phases, and numerous improvements and bug fixes were implemented in between. The models described in Sect. 3, and all other details given hereafter, refer to AGIS 3.2.

### 4.2. Primary solution for AGIS 3.2

Although all steps listed in the previous section are needed for a successful astrometric solution, the primary solution (step 5) is by far the most important and difficult one. As described elsewhere (Lindegren et al. 2012), the primary solution iteratively updates the four kinds of unknowns (source, attitude, calibration, and global parameters). The algorithm can be described in terms of four separate blocks, designated S, A, C, and G. In S the astrometric parameters of the primary sources are updated based on current values for the other unknowns; in A the attitude parameters are updated based on current source, calibration, and global parameters; and so forth. The blocks are normally executed in a cyclic manner, for example S-A-C-G-S-A-C-G-S-A-..., where S-A-C-G constitutes one iteration. (For specific purposes, some of the blocks may be left out, meaning that the corresponding unknowns are kept fixed.) In the simple iteration (SI) algorithm, there is no memory of the updates in previous iterations that can be used to optimise the next update; this algorithm reliably converges in all relevant cases and is numerically very stable, but may require many iterations for complete convergence. The

conjugate gradient (CG) algorithm (Bombrun et al. 2012) speeds up convergence considerably, but is less stable and (unlike SI) does not allow observation weights to be changed from one iteration to the next. Weight adjustment is necessary for a good treatment of outliers and for estimating the excess noise. Most often AGIS employs a hybrid scheme consisting of three SI iterations during which the weights are adjusted, followed by three CG iterations with fixed weights; this sequence is then repeated as many times as required. A complete run typically ends with a sequence of simple iterations, confirming that the solution is sufficiently converged.

The primary solution for AGIS 3.2 processed about 6.5 billion ( $6.5 \times 10^9$ ) CCD observations for 14.3 million primary sources. The solution determined 71.5 million source parameters together with 10.7 million attitude parameters, 1.1 million calibration parameters, and 2.0 million global parameters; the redundancy factor (mean number of observations per unknown) is  $\approx 76$ . (This does not count the corrective attitude, for which a largely different set of observations was used to estimate some 17 million parameters.)

The sequence of iterations executed in the primary solution for AGIS 3.2 is detailed in Table 3. After a warm-up run to obtain good starting values, a total of 165 iterations were made using the global model described in Sect. 3.4. In the last 39 iterations the global parameter  $\delta C_{1,0}$  was also adjusted, resulting in a significant reduction of the (negative) parallax bias (Sect. 3.4.4).

#### 4.3. Secondary solutions

In this step the astrometric parameters were computed for all sources, including the primary sources. Depending on the colour information used in the IPD for a particular source, it received a five- or six-parameter solution as described in Sect. 2.3, but otherwise the treatment was identical. The five-parameter solutions used calibration C obtained in step 5 of Sect. 4.1, while the six-parameter solutions used calibration C' obtained in step 6. For sources with an insufficient number of observations, or where the astrometric results failed to meet the acceptance criteria for a five- or six-parameter solution (Sect. 4.4), only the mean position at the reference epoch (J2016.0) is published.

The secondary solutions processed nearly 78 billion FoV transits, generating converged solutions for 2.495 billion sources (of which 585 million five-parameter, 883 million six-parameter, and 1027 million two-parameter solutions). Subsequently some of the five- and six-parameter solutions and most of the two-parameter solutions were removed because they failed to meet the acceptance criteria (Sect. 4.4). The final number of sources and other statistics are given in Sect. 5.

#### 4.4. Acceptance criteria and fallback (two-parameter) solutions

The decision whether a converged, non-duplicated secondary solution is accepted as a five- or six-parameter solution, or at all retained for publication, depends on the four quantities  $N_{\text{tr, astr}}$ ,  $N_{\text{vpu}}$ ,  $\sigma_{\text{pos, max}}$ , and  $\sigma_{5\text{d, max}}$  calculated in the course of the source update process. Here,  $N_{\text{tr, astr}}$  is the number of FoV transits (detections) used in the AGIS solution; in the *Gaia* Archive it is given as `astrometric_matched_transits`.  $N_{\text{vpu}}$  (`visibility_periods_used`) is the number of distinct observation epochs (visibility periods) used in the solution, where a visibility period is a group of observations separated from other groups by a gap of at least four days.  $\sigma_{\text{pos, max}}$  (not in the *Gaia* Archive) is the semi-major axis of the error ellipse in position

at the reference epoch J2016.0 (Eq. (B1) in Lindegren et al. 2018). Finally,  $\sigma_{5\text{d, max}}$  (`astrometric_sigma5d_max`) is the five-dimensional equivalent to  $\sigma_{\text{pos, max}}$ , calculated as described in Sect. 4.3 of Lindegren et al. (2018) but with  $T = 2.76383$  yr for the time coverage of the data used in the solution and ignoring the pseudocolour for six-parameter solutions.

For every source, a solution with five or six parameters (depending on the colour information used in IPD) was first tried. This was accepted if it converged and satisfied the criterion

$$G \leq 21.0 \quad \text{and} \quad N_{\text{vpu}} \geq 9 \quad \text{and} \quad \sigma_{5\text{d, max}} < (1.2 \text{ mas}) \times \gamma(G), \quad (21)$$

where  $\gamma(G) = 10^{0.2 \max(6-G, 0, G-18)}$ . This is similar to the DR2 criterion (Eq. (11) in Lindegren et al. 2018), except that the minimum  $N_{\text{vpu}}$  is higher and the upper limit on  $\sigma_{5\text{d, max}}$  was increased for  $G < 6$  to accommodate the sharply rising uncertainty for the brightest sources (Fig. 7). The present threshold on  $N_{\text{vpu}}$  removes most cases where a lower threshold might produce spurious solutions, like the ones found in DR2 with very large (positive or negative) parallaxes. We note that the  $G$  used in Eq. (21) is not the EDR3 value, which was unavailable at the time, but the value from DR2, or the real-time magnitude estimate from the on-board object detection if the source was not in DR2. In EDR3 there are 143 546 sources with five- or six-parameter solutions and EDR3 magnitude  $G > 21$ , and conversely some sources with two-parameter solutions that would have passed Eq. (21) if the EDR3 magnitude had been used. (Elsewhere in this paper  $G$  stands for the EDR3 value `phot_g_mean_mag`.)

If the five- or six-parameter solution did not converge, or failed to satisfy Eq. (21), prior information on the parallax and proper motion was added, based on the Galactic model described in Michalik et al. (2015) and Sect. 4.3 of Lindegren et al. (2018). In such cases only the position parameters ( $\alpha$ ,  $\delta$ ) at epoch J2016.0 and their covariances were retained out of the full five- or six-parameter solution. As explained in Michalik et al. (2015), the purpose of the Galactic prior is to provide more realistic uncertainties for the positions of sources with a very small number of observations, by making some reasonable assumption about the sizes of their parallaxes and proper motions. The resulting position is called a two-parameter solution (`astrometric_params_solved` = 3), although in reality all five or six parameters are estimated. A two-parameter solution was accepted for publication if it satisfied the criterion

$$N_{\text{tr, astr}} \geq 5 \quad \text{and} \quad \sigma_{\text{pos, max}} < 100 \text{ mas}. \quad (22)$$

It can be noted that any solution that satisfies Eq. (21) also satisfies Eq. (22), which therefore holds for all sources in EDR3. In contrast to the corresponding criterion for *Gaia* DR2 (Eq. (12) in Lindegren et al. 2018), Eq. (22) puts no upper limit on the `astrometric_excess_noise`, because it was found that such a limit rejects many partially resolved binaries that should be retained in the catalogue for completeness, even though they do not have full astrometric data.

Finally, all sources, irrespective of the kind of solution, must be solitary in the sense that there is no other source within a radius of 0.18 arcsec, as calculated from the position parameters ( $\alpha$ ,  $\delta$ ) at the reference epoch. If multiple sources are found at smaller separations, only one source is kept, namely, in order of precedence: (i) a source previously identified as relevant for the extragalactic reference frame; (ii) the five- or six-parameter solution with the smallest  $\sigma_{5\text{d, max}}$ ; or (iii) the two-parameter solution with the smallest  $\sigma_{5\text{d, max}}$ . In such cases the retained source has the flag `duplicated_source` set in the *Gaia* Archive.

#### 4.5. Ad hoc correction of WC0 calibration

Between iterations 141 and 142 an ad hoc correction was applied to the WC0 calibration parameters in order to mitigate a known problem with the bright ( $G \lesssim 13$ ) reference frame. The motivation and procedure for this correction, which should not be needed in future processing cycles, are briefly as follows.

During the internal validation of the AGIS 2.2 solutions, carried out by the astrometry team prior to the publication of *Gaia* DR2, it was found that the reference frame of the bright sources ( $G \lesssim 12\text{--}13$ ) in DR2 was rotating, relative to the frame defined by the fainter quasars, at a rate of about  $0.15 \text{ mas yr}^{-1}$  (Sect. 5.1 of Lindegren et al. 2018). The problem was confirmed by Brandt (2018) in a comparison with proper motions calculated from the position differences between the DR2 and HIPPARCOS catalogues, and by Lindegren (2020a,b) in a comparison with radio-interferometric (VLBI) observations of bright radio stars. The likely cause of the effect is explained in Appendix B of Lindegren (2020a).

A similar effect was seen during the production of AGIS 3.1. A major concern then was that these systematics, if left uncorrected in AGIS 3.1, would propagate into the time-dependent LSF and PSF calibrations of WC0 sources in CALIPD 3.2, only to appear again in AGIS 3.2. It was therefore decided to implement an ad hoc correction to the calibration parameters of WC0 in AGIS 3.1, counteracting the effect. This procedure successfully fixed the bright reference frame in AGIS 3.1, but the problem nevertheless reappeared in AGIS 3.2, albeit with different values. A similar ad hoc correction was therefore made after iteration 141 in the AGIS 3.2 iteration sequence (Table 3). Because the calibration was not updated in the subsequent iterations, the correction remained effective in the final results.

To explain the correction it is useful to consider how the AL astrometric measurements are affected by a change in the source positions corresponding to a small error in the celestial reference frame. The orientation error at a certain time is given by the (numerically small) rotation vector  $\boldsymbol{\varepsilon}$ , such that the change in the unit vector  $\boldsymbol{u}$  towards a source is  $\Delta\boldsymbol{u} = \boldsymbol{\varepsilon} \times \boldsymbol{u}$ . Let  $\boldsymbol{z}$  be the unit vector, at the same instant, along the nominal spin axis of *Gaia* (more precisely,  $\boldsymbol{z}$  is the third axis of the scanning reference system SRS; e.g. Fig. 2 in Lindegren et al. 2012).  $\boldsymbol{z}$  and  $\boldsymbol{u}$  must be nearly orthogonal for the source to be observed in one of the FoVs, and for simplicity we assume  $\boldsymbol{z}'\boldsymbol{u} = 0$ . The tangent vector of the AL field angle  $\eta$  at the source is then the unit vector  $\boldsymbol{z} \times \boldsymbol{u}$ , and the component of  $\Delta\boldsymbol{u}$  in the AL direction is  $\Delta\eta = (\boldsymbol{z} \times \boldsymbol{u})' \Delta\boldsymbol{u} = \boldsymbol{z}'\boldsymbol{\varepsilon} - (\boldsymbol{z}'\boldsymbol{u})(\boldsymbol{u}'\boldsymbol{\varepsilon}) = \boldsymbol{z}'\boldsymbol{\varepsilon}$ . Both  $\boldsymbol{\varepsilon}$  and  $\boldsymbol{z}$  are functions of time, thus  $\Delta\eta(t) = \boldsymbol{z}(t)' \boldsymbol{\varepsilon}(t)$ . Here  $\boldsymbol{z}(t)$  is set by the scanning law, while the standard model of stellar motion (Sect. 3.1) requires that the frame orientation error is a linear function of time,  $\boldsymbol{\varepsilon}(t) = \boldsymbol{\varepsilon}(t_{\text{ep}}) + (t - t_{\text{ep}})\boldsymbol{\omega}$ . The function  $\Delta\eta(t)$  therefore has six degrees of freedom corresponding to the components of the vectors  $\boldsymbol{\varepsilon}(t_{\text{ep}})$  and  $\boldsymbol{\omega}$ . The important conclusion from this brief discussion is that only very specific forms of time-dependent AL displacements in the calibration model could be mistaken for a reference frame error.

In the astrometric calibration model (Sect. 3.3), the AL large-scale calibration for WC1 ( $G \approx 13$  to  $16$ ) has a fixed origin, when averaged over both FoVs, but for WC0 and WC2 it is necessary to permit time-dependent displacements relative to WC1. This means that each WC could in principle have its own reference frame, namely if the relative displacement between their calibrations can be described in the form of the function  $\Delta\eta(t)$  introduced above for some vectors  $\boldsymbol{\varepsilon}(t_{\text{ep}})$  and  $\boldsymbol{\omega}$ . In practice this should not be a problem, because many primary sources around

magnitude 13 and 16 are not always observed in the same WC, and they will only obtain consistent solutions if the reference frame is the same in all WC. This mechanism apparently works as expected for the transition between WC1 and WC2 around  $G = 16$ , but not for the transition between WC1 and WC0 around  $G = 13$ . The probable reason for this is the generally problematic calibrations in WC0, both in CALIPD and AGIS.

The ad hoc correction amounts to adding the time-dependent correction  $\Delta\eta(t) = (t - t_{\text{ep}})\boldsymbol{z}(t)'\boldsymbol{\omega}$  to the WC0a and WC0b calibrations, where  $\boldsymbol{\omega} = [-0.0166, -0.0950, +0.0283]' \text{ mas yr}^{-1}$  was estimated from a comparison of the proper motions of HIPPARCOS stars, as obtained in iteration 141 from the *Gaia* observations, and as derived from the positional differences between *Gaia* DR2 and the HIPPARCOS catalogue (van Leeuwen 2007). For lack of better information, it was necessary to assume that the positional systems of the different window classes agreed at the reference epoch, in other words that  $\boldsymbol{\varepsilon}(t_{\text{ep}}) = \mathbf{0}$ . In effect, the applied correction implies that the bright reference frame of EDR3, when extrapolated to the HIPPARCOS epoch J1991.25, agrees with the HIPPARCOS reference frame. The uncertainty in the alignment of the HIPPARCOS reference frame to the ICRS at epoch J1991.25 was  $\pm 0.6 \text{ mas}$  in each axis (Kovalevsky et al. 1997), which gives a systematic uncertainty of at least  $(0.6 \text{ mas}) / (24.75 \text{ yr}) \approx 0.024 \text{ mas yr}^{-1}$  per axis in the spin of the bright reference frame of *Gaia* EDR3.

It is important to note that the ad hoc correction does not adjust the proper motions individually for agreement with the HIPPARCOS positions (as was done for the *Gaia* DR1 TGAS solution; Gaia Collaboration 2016b); only the reference frame is adjusted via the WC0 calibration parameters. Nevertheless, resorting to this procedure is very unsatisfactory and hopefully exceptional: improved calibrations in CALIPD and AGIS for the WC0 observations should eliminate the need for it in future releases. However, it highlights the need for independent means to verify the consistency of the *Gaia* reference frame over the full range of magnitudes, for example by means of VLBI observations of radio stars (Lindegren 2020a).

## 5. Results: astrometric properties of EDR3

### 5.1. Overview of the data

The main table of *Gaia* EDR3, *gaia\_source*, gives astrometric data for more than 1.8 billion sources. The exact numbers are 585 416 709 sources with five-parameter solutions (*astrom\_params\_solved*=31), 882 328 109 with six-parameter solutions (*astrom\_params\_solved*=95), and 343 964 953 with two-parameter solutions (*astrom\_params\_solved*=3). In total there are 1 811 709 771 sources. Their distribution in  $G$  magnitude (*photometric\_g\_mean\_mag*) is shown in Fig. 5.

In the following we give statistics related to the quantities listed below with their brief explanations.

- *ra\_error* = standard uncertainty in right ascension at epoch J2016.0,  $\sigma_{\alpha^*} = \sigma_{\alpha} \cos \delta$
- *dec\_error* = standard uncertainty in declination at epoch J2016.0,  $\sigma_{\delta}$
- *parallax\_error* = standard uncertainty in parallax,  $\sigma_{\varpi}$
- *pmra\_error* = standard uncertainty of proper motion in right ascension,  $\sigma_{\mu\alpha^*} = \sigma_{\mu\alpha} \cos \delta$
- *pmdec\_error* = standard uncertainty of proper motion in declination,  $\sigma_{\mu\delta}$
- *pseudocolour\_error* = standard uncertainty of the pseudocolour,  $\sigma_{\text{peff}}$



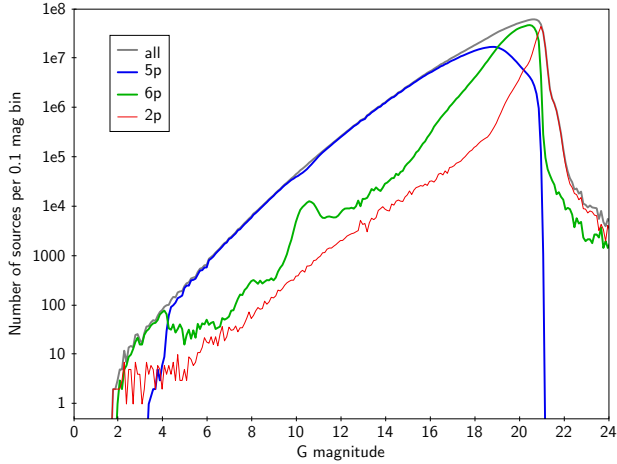


**Fig. 5.** Magnitude distribution of sources in *Gaia* EDR3. The grey denotes all sources, the blue denotes sources with five-parameter solutions, the green denotes sources with six-parameter solutions, and the red denotes sources with two-parameter solutions.

- semi-major axis of error ellipse in position at epoch J2016.0,  $\sigma_{\text{pos,max}}$  (Eq. (B.1) in Lindegren et al. 2018)

- semi-major axis of error ellipse in proper motion,  $\sigma_{\text{pm,max}}$  (Eq. (B.2) in Lindegren et al. 2018)

- `ruwe` = renormalised unit weight error (RUWE). The unit weight error (UWE) is the square root of the normalised chi-square of the astrometric fit to the AL observations,  $\text{UWE} = [\chi^2/(n - n_p)]^{1/2}$ , where  $n$  is the number of good CCD observations of the source (see below) and  $n_p = 5$  or  $6$  the number of parameters fitted.  $\text{UWE} \approx 1.0$  is expected for a well-behaved source, but that is often not the case owing to calibration errors. The RUWE is calculated by empirical scaling of the UWE, depending on  $G$  and  $v_{\text{eff}}$  or  $\hat{v}_{\text{eff}}$ , such that  $\text{RUWE} \approx 1.0$  for well-behaved sources (see also Sect. 5.3). This statistic is not given for two-parameter solutions.

- `astrometric_excess_noise` = excess source noise,  $\epsilon_i$ : This is the extra noise per observation that must be postulated to explain the scatter of residuals in the astrometric solution for the source (see also Sect. 5.3). The excess source noise is considered to be statistically significant if `astrometric_excess_noise_sig`  $> 2$

- `visibility_periods_used` = number of visibility periods of the source, that is, groups of observations separated by at least four days

- `astrometric_matched_observations` = number of FoV transits of the source used in the astrometric solution

- `astrometric_n_good_obs_al` = number of good CCD observations AL of the source used in the astrometric solution

- fraction of outliers (bad CCD observations AL) = `astrometric_n_bad_obs_al/astrometric_n_obs_al`

- `ipd_gof_harmonic_amplitude` = amplitude of the natural logarithm of the goodness-of-fit obtained in the IPD versus position angle of scan

- `ipd_frac_multi_peak` = fraction of CCD observations where IPD detected more than one peak

- `ipd_frac_odd_win` = fraction of FoV transits with truncated windows or multiple gates

The last three statistics were generated at the image parameter determination (IPD) stage prior to the astrometric solution, and may include transits that were not used for the astrometry. They are listed here because they provide information on (potentially) problematic sources, complementary to what is obtained

from the astrometric fit (see Sect. 5.3). We refer to the *Gaia* Archive on-line documentation for further explanation of these statistics.

Although both the five- and six-parameter solution provides estimates of the five astrometric parameters (position, parallax, and proper motion), the six-parameter solution (with pseudocolour as the sixth parameter) is intrinsically less accurate because the default colour had to be used for the IPD. Moreover, the six-parameter solution is normally only used for sources that are problematic in some respect, for example in very crowded areas, which tends to reduce its accuracy even more. It is therefore usually relevant to give separate statistics for the two kinds of solution. In Tables 4–6 we report the mean or median values of most of the statistics listed above, as functions of magnitude and separated by the kind of solution. The median is used for quantities that have a long-tailed distribution, for which the mean value might be less representative.

## 5.2. Angular resolution

Resolution here refers to the minimum angular separation between distinct sources in *Gaia* EDR3, that is between objects with different `source_id`. As explained in Sect. 4.4, the separation will by construction never be smaller than 0.18 arcsec, but relatively few sources are found with separations less than about 0.6 arcsec owing to other limitations. In a given situation, the effective resolution (however it is defined) depends on many different factors such as the magnitudes of both components in a pair, their relative orientation on the sky, and the kinds of solutions involved (with five, six, or two parameters). The complex situation is illustrated in Fig. 6, which shows the neighbourhood of all sources in EDR3 of magnitude  $G \approx 15$ , subdivided by the kind of solution. Clearly most neighbours at separation 0.18–0.6 arcsec only have two-parameter solutions, while neighbours with five-parameter solutions are usually either the brighter of the two sources or more distant than 2 arcsec. The six-parameter solutions partly fill the gap for separations between 0.6 and 2 arcsec. Additional statistics on the small-scale completeness of EDR3 are given in Fabricius et al. (2021).

## 5.3. Goodness-of-fit statistics

Several of the statistics listed in Sect. 5.1 quantify the goodness-of-fit of the single-star model to the observations, either at the image parameter determination (IPD), where a model LSF or PSF is fitted to the CCD samples, or in the subsequent astrometric solution, where the standard model of stellar motion (Sect. 3.1) is fitted to the resulting image locations. A few remarks should be made concerning the interpretation of these statistics and their interrelations.

For the user, the most relevant goodness-of-fit statistics from the IPD are `ipd_gof_harmonic_amplitude`, `ipd_frac_multi_peak`, and `ipd_frac_odd_win`; and from the astrometric fit, the RUWE and the excess source noise with its significance. (The fraction of outliers is probably less useful: The outlier detection is designed to remove occasional large deviations, caused by temporary perturbations that are usually unrelated to the source.) All of them describe (real or spurious) deviations from the simplest possible point-source model, but they are sensitive to different kinds of modelling errors, and all of them are more or less sensitive to calibration errors. The sensitivity is usually a strong function of the magnitude of the source, and may also depend on geometric factors such as the distribution of scans across the source. All of this complicates the



**Table 4.** Summary statistics for the 585 million sources in *Gaia* EDR3 with five-parameter solutions.

Quantity	Value at $G =$										Unit
	9–12	13	14	15	16	17	18	19	20	21	
Fraction of sources with 5-param. solution	92.9	97.0	97.1	96.7	93.8	87.5	76.7	49.7	14.5	1.4	%
Median standard uncertainty in $\alpha$ ( $\sigma_{\alpha^*}$ ) at J2016.0	0.014	0.012	0.015	0.022	0.034	0.054	0.094	0.175	0.374	1.006	mas
Median standard uncertainty in $\delta$ ( $\sigma_{\delta}$ ) at J2016.0	0.013	0.011	0.013	0.019	0.030	0.049	0.086	0.161	0.335	0.977	mas
Median standard uncertainty in $\varpi$ ( $\sigma_{\varpi}$ )	0.018	0.015	0.019	0.027	0.042	0.069	0.120	0.221	0.459	1.320	mas
Median standard uncertainty in $\mu_{\alpha^*}$ ( $\sigma_{\mu_{\alpha^*}}$ )	0.018	0.016	0.019	0.028	0.044	0.071	0.123	0.229	0.487	1.445	mas yr <sup>-1</sup>
Median standard uncertainty in $\mu_{\delta}$ ( $\sigma_{\mu_{\delta}}$ )	0.016	0.014	0.017	0.024	0.038	0.063	0.111	0.208	0.428	1.401	mas yr <sup>-1</sup>
Median renormalised unit weight error (RUWE)	1.039	1.023	1.016	1.013	1.012	1.011	1.010	1.010	1.010	1.016	
Fraction with significant excess source noise	97.3	59.4	19.2	16.8	13.8	10.6	7.5	5.0	5.0	11.7	%
Median excess source noise (when significant)	0.113	0.089	0.188	0.224	0.285	0.409	0.606	0.976	1.801	3.668	mas
Mean number of visibility periods used	20.9	21.0	20.9	20.8	20.7	20.7	20.7	20.5	19.2	13.1	
Mean number of FoV transits used	43.7	43.7	43.6	43.4	43.2	43.2	43.4	42.6	38.7	20.5	
Mean number of good CCD observations AL	378	378	377	376	374	374	376	368	334	175	
Mean fraction of bad CCD observations AL	1.2	0.4	0.5	0.5	0.5	0.4	0.4	0.4	0.5	0.6	%
Median ipd_gof_harmonic_amplitude	0.018	0.021	0.020	0.020	0.020	0.020	0.020	0.022	0.029	0.073	
Mean ipd_frac_multi_peak	1.9	1.5	1.5	1.7	0.9	0.6	0.3	0.2	0.1	0.9	%
Mean ipd_frac_odd_win	0.0	0.0	0.0	0.0	0.0	0.0	0.1	0.1	0.2	0.8	%

**Table 5.** Summary statistics for the 882 million sources in *Gaia* EDR3 with six-parameter solutions.

Quantity	Value at $G =$										Unit
	9–12	13	14	15	16	17	18	19	20	21	
Fraction of sources with 6-param. solution	6.2	2.4	2.2	2.7	5.6	11.9	22.4	48.6	77.7	27.5	%
Median standard uncertainty in $\alpha$ ( $\sigma_{\alpha^*}$ ) at J2016.0	0.017	0.026	0.025	0.033	0.052	0.081	0.131	0.225	0.430	1.031	mas
Median standard uncertainty in $\delta$ ( $\sigma_{\delta}$ ) at J2016.0	0.016	0.024	0.023	0.030	0.045	0.069	0.112	0.194	0.382	1.025	mas
Median standard uncertainty in $\varpi$ ( $\sigma_{\varpi}$ )	0.023	0.033	0.031	0.040	0.061	0.093	0.151	0.266	0.526	1.390	mas
Median standard uncertainty in $\mu_{\alpha^*}$ ( $\sigma_{\mu_{\alpha^*}}$ )	0.023	0.034	0.033	0.042	0.065	0.102	0.167	0.291	0.565	1.469	mas yr <sup>-1</sup>
Median standard uncertainty in $\mu_{\delta}$ ( $\sigma_{\mu_{\delta}}$ )	0.021	0.031	0.029	0.036	0.051	0.078	0.132	0.240	0.490	1.470	mas yr <sup>-1</sup>
Median standard uncertainty in $\hat{\nu}_{\text{eff}}$ ( $\sigma_{\hat{\nu}_{\text{eff}}}$ )	0.004	0.006	0.006	0.008	0.012	0.019	0.031	0.055	0.109	0.281	$\mu\text{m}^{-1}$
Median renormalised unit weight error (RUWE)	1.127	1.362	1.167	1.104	1.102	1.085	1.053	1.033	1.029	1.048	
Fraction with significant excess source noise	99.6	95.1	75.4	68.3	64.0	58.3	45.5	27.8	17.7	19.6	%
Median excess source noise (when significant)	0.169	0.275	0.387	0.405	0.471	0.569	0.809	1.343	2.153	3.838	mas
Mean number of visibility periods used	21.4	21.1	20.7	20.1	18.9	18.2	18.4	18.5	18.1	13.3	
Mean number of FoV transits used	46.1	44.6	44.0	42.6	39.3	38.2	37.9	37.8	36.6	21.1	
Mean number of good CCD observations AL	400	384	379	366	339	331	328	327	315	181	
Mean fraction of bad CCD observations AL	1.3	1.5	1.9	2.1	1.5	1.0	0.7	0.6	0.6	0.6	%
Median ipd_gof_harmonic_amplitude	0.020	0.033	0.032	0.030	0.035	0.034	0.032	0.030	0.031	0.071	
Mean ipd_frac_multi_peak	9.4	25.4	21.6	18.3	10.7	7.0	5.5	3.2	1.0	0.5	%
Mean ipd_frac_odd_win	0.0	4.8	7.9	8.1	6.3	5.2	4.4	4.2	3.8	2.1	%

**Table 6.** Summary statistics for the 344 million sources in *Gaia* EDR3 with two-parameter solutions.

Quantity	Value at $G =$										Unit
	9–12	13	14	15	16	17	18	19	20	21	
Fraction of sources with 2-param. solution	0.8	0.7	0.7	0.6	0.6	0.6	0.9	1.7	7.8	71.1	%
Median standard uncertainty in $\alpha$ ( $\sigma_{\alpha^*}$ ) at J2016.0	1.771	1.260	1.127	1.116	1.060	1.008	0.979	1.436	2.579	3.250	mas
Median standard uncertainty in $\delta$ ( $\sigma_{\delta}$ ) at J2016.0	1.703	1.211	1.078	1.067	0.994	0.925	0.888	1.252	2.106	2.847	mas
Mean number of visibility periods used	17.9	18.4	18.2	18.0	17.7	17.0	15.7	10.9	8.0	6.9	
Mean number of FoV transits used	35.2	36.3	35.9	35.4	34.7	33.6	30.7	19.7	13.3	10.0	
Mean number of good CCD observations AL	299	306	304	300	294	285	261	167	113	85	
Mean fraction of bad CCD observations AL	4.3	3.5	3.5	3.5	3.5	3.4	3.1	2.5	1.6	0.9	%
Median ipd_gof_harmonic_amplitude	0.217	0.251	0.258	0.261	0.279	0.273	0.256	0.259	0.175	0.096	
Mean ipd_frac_multi_peak	59.2	53.0	44.8	43.6	36.0	27.8	20.8	14.2	6.8	0.3	%
Mean ipd_frac_odd_win	0.0	12.5	19.2	19.8	27.2	31.1	33.3	35.6	25.2	3.1	%

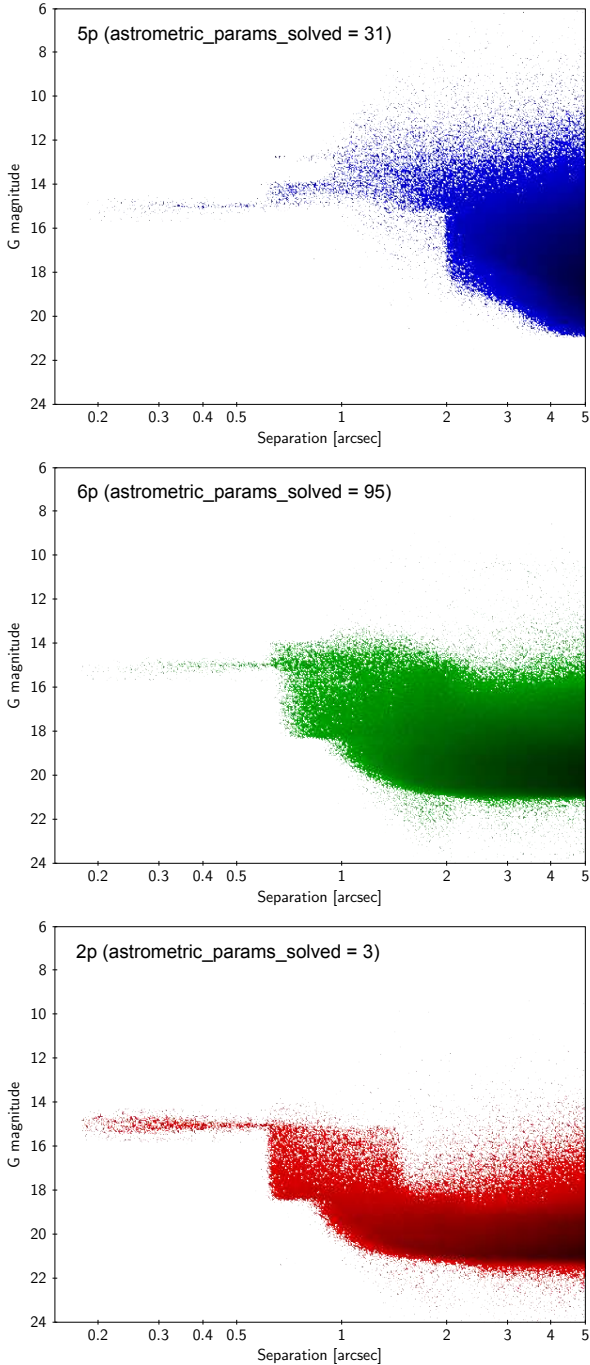


**Fig. 6.** Neighbourhood of 15th magnitude sources in *Gaia* EDR3. The diagrams show all sources within 5 arcsec from any one of the 2.8 million sources in EDR3 with  $14.95 < G < 15.05$  mag. *Top*: five-parameter solutions. *Middle*: six-parameter solutions. *Bottom*: two-parameter solutions.

interpretation of the statistics. For example, there is no simple way to convert them into  $p$ -values, using the single-star model as a null hypothesis; instead, the relevant distributions must be determined empirically, if it is at all possible.

The IPD statistics may be quite powerful for detecting certain kinds of binaries. `ipd_gof_harmonic_amplitude` is normally small but could become large for sources that have elongated images, such as partially resolved binaries, provided that their position angles are relatively fixed. In such cases `ipd_gof_harmonic_phase` indicates the position angle of the

major axis modulo  $180^\circ$ . `ipd_frac_multi_peak` is sensitive to resolved binaries that in some scan directions produce more than one peak in the window. Finally, `ipd_frac_odd_win` is sensitive to the presence of another (usually brighter) source causing the window to be “odd”, that is truncated or with multiple gating modes. The source causing the gating could however be quite far away on the CCD, or even in the other FoV. Transits with odd windows were not used in the astrometric solution for EDR3. From Tables 4–6 it is seen that sources with five-parameter solutions are usually very clean, as indicated by the IPD statistics, while the six-parameter solutions have higher fractions of observations with multiple peaks or odd windows (which partially explains why they did not have sufficiently good BP and RP photometry for the calculation of  $\nu_{\text{eff}}$ ), and the two-parameter solutions are even worse. Towards the faint magnitudes the `ipd_frac_multi_peak` is always decreasing, because the diminishing signal-to-noise ratio (S/N) makes the detection of secondary peaks increasingly difficult.

The astrometric goodness-of-fit measures RUWE and excess source noise (`astrometric_excess_noise`) quantify the same thing, namely how much the motion of the image centre (as determined by the IPD) deviates from the standard model of stellar motion fitted in the astrometric solution. However, while the `astrometric_excess_noise` gives the discrepancy in angular measure (mas) per AL observation (ideally = 0 for a good fit), the RUWE gives the discrepancy as a dimensionless factor (ideally = 1.0). The RUWE was obtained from the unit weight error  $\text{UWE} = [\chi^2 / (n - n_p)]^{1/2}$  by applying an empirical scaling factor to compensate for calibration errors, which tend to increase the UWE for bright, blue, and very red sources. A corresponding correction was not applied to the `astrometric_excess_noise`, which must therefore be interpreted with some caution for sources with  $G \lesssim 13$ ,  $\nu_{\text{eff}} \gtrsim 1.65$  ( $G_{\text{BP}} - G_{\text{RP}} \lesssim 0.4$ ), or  $\nu_{\text{eff}} \lesssim 1.24$  ( $G_{\text{BP}} - G_{\text{RP}} \gtrsim 3.0$ ). The significance (S/N) of the excess source noise is given by `astrometric_excess_noise_sig`: `astrometric_excess_noise` should be regarded as insignificant (that is, effectively zero) if `astrometric_excess_noise_sig`  $\lesssim 2$ . Alternatively, `astrometric_excess_noise / astrometric_excess_noise_sig` may be taken as an estimate of the uncertainty of the excess source noise. The RUWE and excess source noise are sensitive to the photocentric motions of unresolved objects, such as astrometric binaries, which are not revealed by the IPD statistics, and therefore complement the latter in binary detection.

The standard uncertainties given in EDR3 have been adjusted to take into account the excess noise, whether it represents an astrometric mismatch or a calibration issue; they should not be further inflated based on the goodness-of-fit statistics.

#### 5.4. Formal uncertainties

Tables 4–6 give the median uncertainties of the astrometric parameters at selected magnitudes for the different kinds of solutions. No statistics are given for  $G < 9$  owing to the relatively few sources and rapidly declining quality at this end (see Fig. 7). Compared with DR2 (Tables B.1 and B.2 in Lindegren et al. 2018), the gain in median uncertainty at  $G = 15$  is a factor 0.71 for the positions and parallaxes, and 0.44 for the proper motions. This is slightly better than the factors 0.80 and 0.51 expected purely from the increased length of the data included in the solutions (Sect. 2.2). The extra gain comes mainly from the improved robustness and homogeneity of results made possible by the higher redundancy of observations in the EDR3 solutions.

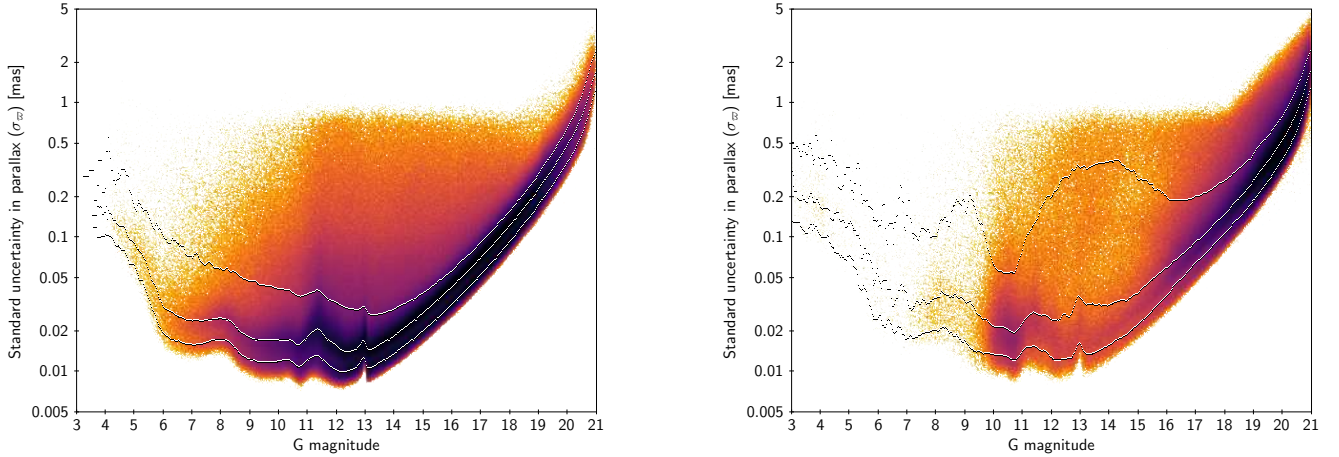


**Fig. 7.** Uncertainty in parallax versus magnitude. *Left:* five-parameter solutions. *Right:* six-parameter solutions. The plots include all sources with  $G < 11.5$  and a geometrically decreasing random fraction of the fainter sources, so as to give a roughly constant number of sources per magnitude interval. The colour scale from yellow to black indicates an increasing density of data points in the diagram. The curves show the 10th, 50th, and 90th percentiles of the distribution at a given magnitude.

For  $G = 9\text{--}12$  the gain in median uncertainty from DR2 to EDR3 is even more impressive thanks to the improved calibrations, which are relatively more important for the bright sources (cf. Appendix A.1): The factor is 0.43 for the positions and parallaxes, and 0.27 for the proper motions.

The comparison between the two releases is however complicated by the circumstance that in EDR3 there are three kinds of solutions (five, six, and two parameters), while in DR2 there are only five- and two-parameter solutions. At  $G = 15$  the five-parameter solutions comprised 99.0% of the sources in DR2 and 96.7% of the sources in EDR3, and the comparison above used the statistics for these subsets. At  $G = 15$  the median uncertainties in EDR3 are a factor 1.5 higher for the 2.7% of the sources with six-parameter solutions than for the 96.7% with five-parameter solutions. This large ratio in the uncertainties reflects the generally more problematic nature of the sources receiving six-parameter solutions, also seen in the various goodness-of-fit statistics discussed in Sect. 5.3.

The fraction of sources that receive five-parameter solutions is higher than 90% down to  $G \simeq 17$ , but decreases rapidly for fainter sources. The fraction with six-parameter solutions correspondingly increases down to  $G \simeq 20$ , after which there is instead a steep increase in the fraction of two-parameter solutions.

At any magnitude there is a considerable spread in the uncertainties caused by variations in the number of observations and the properties of the scanning law. For  $G \leq 12$  there are additional variations depending on the window classes and gates used for a particular source, and the onset of saturation for the brightest sources. The spread is illustrated in Fig. 7 for the parallaxes in the five- and six-parameter solutions. The uncertainties in position and proper motion follow similar distributions.

Figure 8 shows the median uncertainties in position, parallax, and proper motions at  $G \simeq 15$  as functions of position. For the position and proper motion data the semi-major axes of the error ellipses  $\sigma_{\text{pos,max}}$ ,  $\sigma_{\text{pm,max}}$  are plotted. The patterns are very similar at other magnitudes, only scaled according to the general dependence on  $G$  in Table 4 or Fig. 7. These patterns are mainly set by variations in the number, direction, and temporal distribution of the scans across a given position, as governed by the scanning law. In very crowded areas, such as along the Galactic plane and in the general direction of the Galactic

Centre, the increased level of excess source noise from background sources gives a local rise in the median uncertainties, which becomes more important at fainter magnitudes. Some relevant statistics are shown in Fig. 9. A comparison with the corresponding maps for DR2 (Figs. B.3 and B.4 in Lindegren et al. 2018) clearly shows an improved homogeneity in the uncertainties in the ecliptic belt, and the smaller importance of the excess noise in EDR3.

### 5.5. Correlation coefficients

*Gaia* EDR3 gives the complete set of correlation coefficients  $\rho$  between the astrometric parameters provided for a given source. For a source with  $n_p = 5, 6$ , or 2 parameters, we thus have  $n_p(n_p - 1)/2 = 10, 15$ , or 1 non-redundant coefficients. In the *Gaia* Archive they are called `ra_dec_corr`, etc.; here we use the notation  $\rho(\alpha, \delta)$ , etc. The correlations allow the elements of the  $n_p \times n_p$  covariance matrix  $\mathbf{K}$  to be reconstructed as

$$\begin{aligned} K_{00} &= \sigma_{\alpha^*}^2, & K_{11} &= \sigma_{\delta}^2, & \dots, \\ K_{01} &= K_{10} = \rho(\alpha, \delta) \sigma_{\alpha^*} \sigma_{\delta}, & \dots \end{aligned} \quad (23)$$

where indices 0, 1, ... represent the parameters in the usual order,  $\alpha, \delta, \varpi, \mu_{\alpha^*}, \mu_{\delta}, \hat{v}_{\text{eff}}$ .

The correlation coefficients for a given source are mainly determined by the distribution of scan directions and transit times among the observations of the source, which are governed by the scanning law. The correlation coefficients are therefore practically independent of magnitude, and we give here only statistics for sources with  $G = 13$  to 16 mag. Figures 10 and 11 show the median correlation coefficients for five- and six-parameter solutions. We note that the scanning law is (approximately) symmetric with respect to the ecliptic, which is reflected in many features depending on ecliptic latitude ( $\beta$ ) rather than declination ( $\delta$ ). Furthermore, the patterns are often distinctly different for  $|\beta| \lesssim 45^\circ$  (the ecliptic belt) and  $|\beta| \gtrsim 45^\circ$  (the ecliptic caps).

Certain features of predominantly positive or negative correlations are caused by the choice of ICRS (equatorial) coordinates for the position and proper motion parameters, and are much less pronounced if ecliptic coordinates are used. This is the case, for example, with the mainly positive correlations  $\rho(\alpha, \delta)$  and



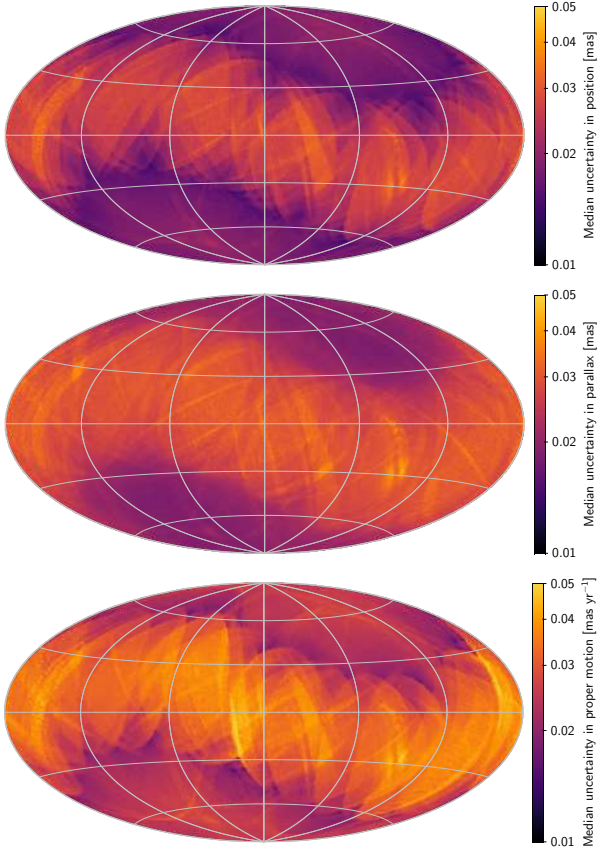


**Fig. 8.** Formal uncertainties at  $G \simeq 15$  for sources with a five-parameter solution in EDR3. *Top*: semi-major axis of the error ellipse in position at epoch J2016.0. *Middle*: standard deviation in parallax. *Bottom*: semi-major axis of the error ellipse in proper motion. These and all other full-sky maps in the paper except Fig. 12 use a Hammer–Aitoff projection in equatorial (ICRS) coordinates with  $\alpha = \delta = 0$  at the centre, north up, and  $\alpha$  increasing from right to left.

$\rho(\mu_{\alpha^*}, \mu_\delta)$  in the ecliptic belt for  $\alpha = 270^\circ - 90^\circ$ , and their mainly negative values for  $\alpha = 90^\circ - 270^\circ$ . Geometrically, this can be understood in terms of the orientation of the error ellipses in position and proper motion: In the ecliptic belt their major axes are approximately aligned with the ecliptic, and consequently tilted by up to  $\pm 23.5^\circ$  with respect to the equator, corresponding to non-zero correlations in the equatorial components. As shown in Fig. 12,  $\rho(\lambda, \beta)$  and  $\rho(\mu_{\lambda^*}, \mu_\beta)$  (here shown on an ecliptic projection) are generally smaller than  $\rho(\alpha, \delta)$  and  $\rho(\mu_{\alpha^*}, \mu_\delta)$ .

The correlations  $\rho(\alpha, \mu_{\alpha^*})$  and  $\rho(\delta, \mu_\delta)$  are related to the mean epoch of observations contributing to the different parameters. A mean epoch later than the reference epoch J2016.0 gives a positive correlation between the position and proper motion, and vice versa. This is especially pronounced for  $\rho(\delta, \mu_\delta)$ , where regions of positive and negative correlations alternate along the ecliptic. The correlations among  $\alpha$ ,  $\delta$ ,  $\varpi$ ,  $\mu_{\alpha^*}$ , and  $\mu_\delta$  are almost the same for the five- and six-parameter solutions. In the six-parameter solutions, the correlations between  $\hat{v}_{\text{eff}}$  and the other five parameters are generally small (RMS values around 0.1) compared with the correlations among the five parameters (RMS values of 0.2–0.3).

The generally small correlations between pseudocolour and the other five parameters is a consequence of the variation in chromaticity along the path of the stellar image through the AF, and between successive observations in either FoV in a

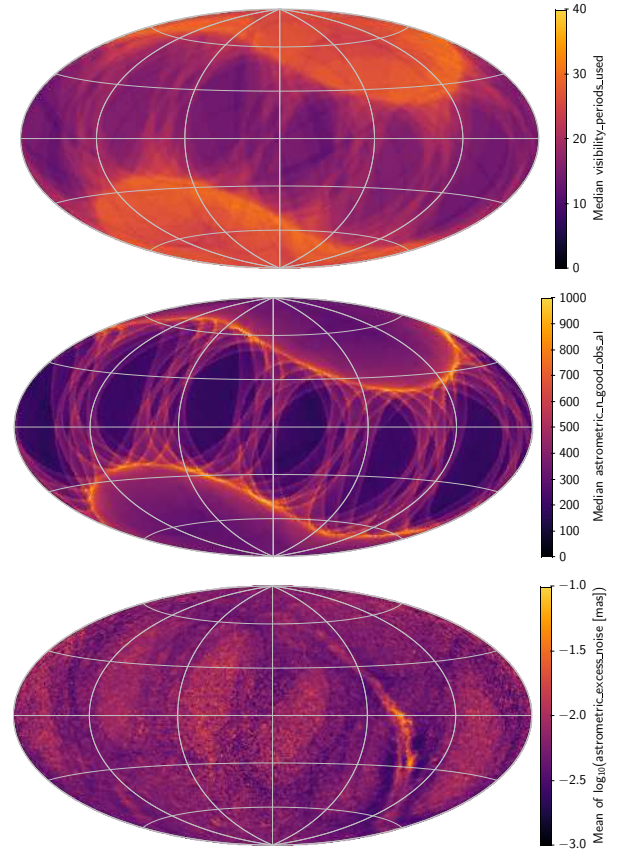


**Fig. 9.** Selected observation statistics at  $G \simeq 15$  for sources with a five-parameter solution in EDR3. These statistics are main factors governing the formal uncertainties of the astrometric data. *Top*: number of visibility periods used. *Middle*: number of good CCD observations AL. (The number of FoV transits used in the solution looks very similar, only with a factor nine smaller numbers.) *Bottom*: mean of  $\log_{10}[\max(0.001, \text{astrometric\_excess\_noise})]$ .

few revolutions; by contrast, the scan directions and observation epochs relevant for the other correlations do not change much over several revolutions. The sizes of the correlations with pseudocolour are important for the potential to improve the six-parameter solutions by incorporating external colour information (Appendix C).

### 5.6. Systematic errors

Several aspects of the systematic errors (biases) in the astrometric data are examined in the EDR3 catalogue validation paper (Fabricius et al. 2021). The bias in parallax, and its variation with magnitude, colour, and ecliptic latitude, is extensively discussed in a separate paper (Lindegren et al. 2021). The global properties of the system of positions and proper motions are discussed in the EDR3 celestial reference frame paper (Gaia Collaboration, in prep.).

In this section we focus on the statistical variations of parallax and proper motion biases on various angular scales, as revealed by the quasars and (for parallaxes on scales  $\lesssim 1^\circ$ ) by sources in the direction of the Large Magellanic Cloud (LMC). We also illustrate the improvements achieved since DR2. The results presented here are derived using relatively faint sources ( $G \simeq 16 - 20$ ), and little is known about small- and medium-scale variations at brighter magnitudes, in particular for  $G < 13$ ,



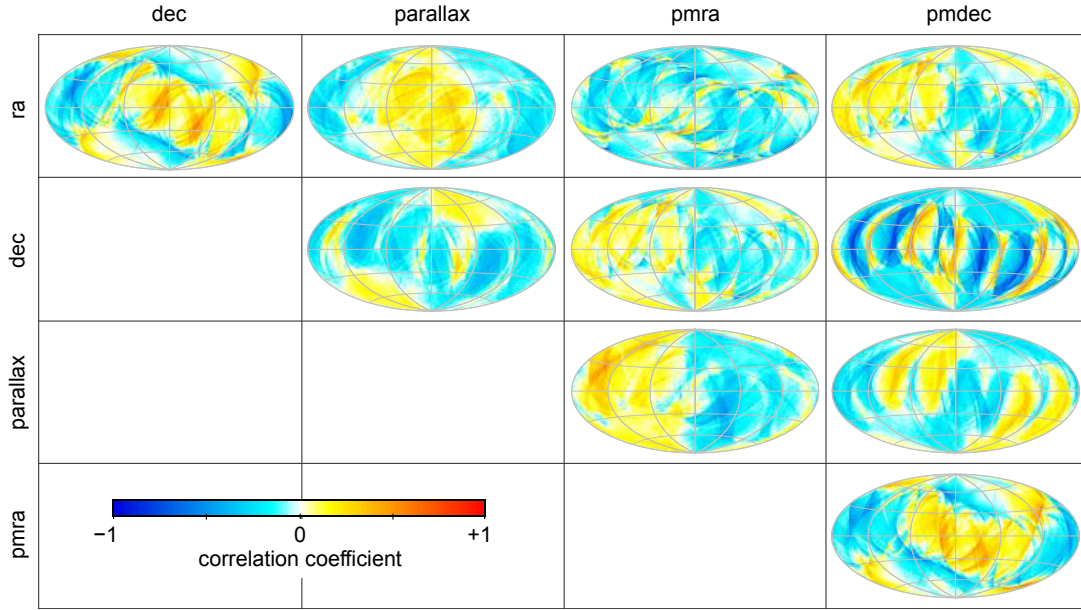


**Fig. 10.** Median correlation coefficients among the astrometric parameters for five-parameter solutions in *Gaia* EDR3. The plots were made from a random selection of five-parameter sources with  $G$  magnitude between 13 and 16. The correlations at other magnitudes are very similar.

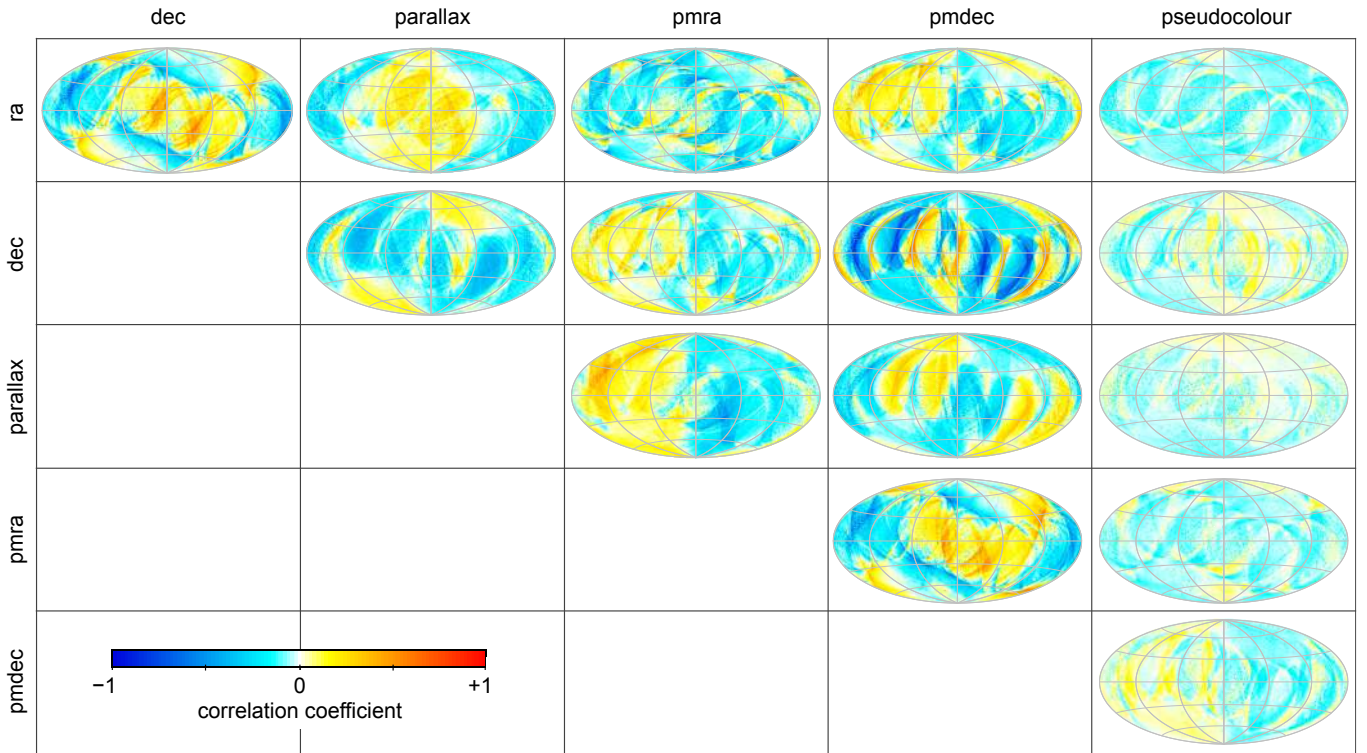


**Fig. 11.** Median correlation coefficients among the astrometric parameters for six-parameter solutions in *Gaia* EDR3. The plots were made using all six-parameter sources with  $G$  magnitude between 13 and 16. The correlations at other magnitudes are very similar.

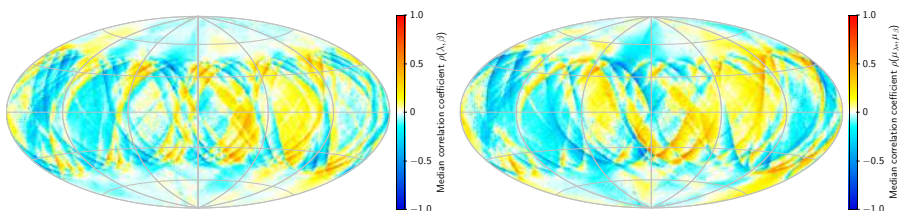


**Fig. 12.** Correlations in ecliptic coordinates (five-parameter solutions,  $G = 13\text{--}16$ ). *Left:* median correlation coefficient between errors in ecliptic longitude ( $\lambda$ ) and latitude ( $\beta$ ). *Right:* same for the proper motion components ( $\mu_\lambda$ ,  $\mu_\beta$ ). Contrary to other sky maps in the paper, these two use a projection in ecliptic coordinates with  $\lambda = \beta = 0$  in the centre.

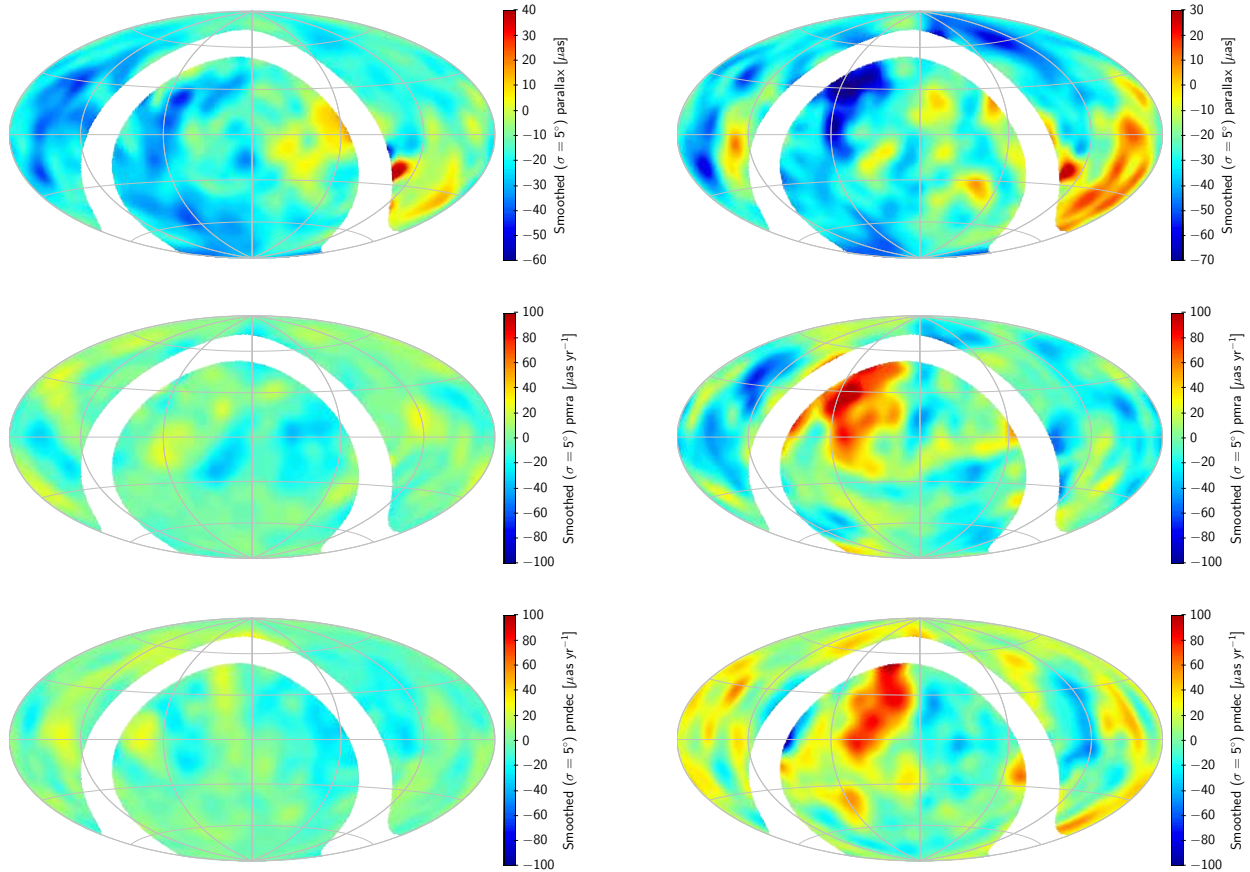


**Fig. 13.** Smoothed maps of quasar parallaxes and proper motions. *Left column:* *Gaia* EDR3, using data for about 1.2 million quasars. *Right column:* *Gaia* DR2, using data for the 94% of the quasars in the left column that have full astrometric solutions also in DR2. From top to bottom the maps show parallax, proper motion in right ascension, and proper motion in declination. The maps were smoothed using a Gaussian kernel with standard deviation  $5^\circ$ . No data are shown for  $|b| < 10^\circ$ , where  $b$  is Galactic latitude.

where the sources in many respects behave differently from the fainter sources. Furthermore, we only give results for the five-parameter solutions, which are used for most sources brighter than  $G \simeq 19$  (Fig. 5). In general the six-parameter solutions are probably worse than the five-parameter solutions in terms of systematics, but it is difficult to know whether this is an intrinsic property of the solutions or a consequence of the faintness and more problematic nature of most of the sources getting a six-parameter solution (Sect. 2.3).

Figure 13 (left) shows smoothed maps of the parallaxes and proper motion components for a sample of 1 215 942 quasars, namely the subset of sources in *Gaia* EDR3 Archive table `agn_cross_id` with five-parameter solutions in `gaia_source` (median  $G = 19.9$ ). The selection of quasars in `agn_cross_id` is discussed in *Gaia* Collaboration (in prep.). Smoothed values were computed using a Gaussian kernel of  $5^\circ$  standard deviation<sup>6</sup>. The smoothed points in the Galactic zone ( $|b| < 10^\circ$ ) are not displayed, as they are dominated by noise from small-number statistics. The standard deviations of the smoothed maps (for  $|b| > 10^\circ$ ) are  $10.8 \mu\text{as}$  in  $\varpi$ ,  $11.2 \mu\text{as yr}^{-1}$  in  $\mu_{\alpha^*}$ , and  $10.7 \mu\text{as yr}^{-1}$  in  $\mu_\delta$ .

For comparison, we show in the right column of Fig. 13 the corresponding maps for *Gaia* DR2 astrometry, calculated in the

same manner for the 1 141 470 of the sources in the EDR3 quasar sample that have full astrometric data also in DR2. To facilitate comparison, the maps use the same colour scales as for the EDR3 data, only shifted by  $10 \mu\text{as}$  in parallax to compensate for the different mean biases. The standard deviations in the DR2 maps are  $15.5 \mu\text{as}$ ,  $26.2 \mu\text{as yr}^{-1}$ , and  $23.5 \mu\text{as yr}^{-1}$ . Thus, in EDR3 the systematics are reduced by the factors 0.70 ( $\varpi$ ), 0.41 ( $\mu_{\alpha^*}$ ), and 0.46 ( $\mu_\delta$ ), that is very nearly the same factors as for the random uncertainties (Sect. 5.4).

On much smaller scales, down to  $0.1^\circ$ , Fig. 14 shows the characteristic “checkered pattern” that was very prominent in the DR2 astrometry for the LMC and in maps of the median parallax in the Galactic bulge area (Sect. 4.2 in Arenou et al. 2018). In EDR3 there is a similar pattern, but with a different structure and smaller amplitude as shown in Fig. 14. The RMS amplitude of the smoothed variations in these plots is  $7.7 \mu\text{as}$  for EDR3 and  $14.3 \mu\text{as}$  for DR2.

The maps in Figs. 13 and 14 were smoothed in order to bring out clearly the pattern of systematic errors. Although the random errors are strongly attenuated by the smoothing, they still contribute to the standard deviations quoted above, which are therefore somewhat higher than the actual RMS systematics on the relevant angular scales. In order to correct for this bias, we randomly divided the sources into two subsets (A and B) of roughly equal size and computed separate smoothed maps  $s_A(\alpha, \delta)$ ,  $s_B(\alpha, \delta)$  for the subsets. Because the random errors are uncorrelated between A and B, while the systematics are the same, an unbiased estimate of the mean square systematics is

<sup>6</sup> More precisely, the smoothed value at a given point is computed as the weighted median of the individual values within a radius of  $15^\circ$ , using weights proportional to  $\exp[-\frac{1}{2}(\theta/5^\circ)^2]$ , where  $\theta$  is the angle between the quasar and the smoothed point.



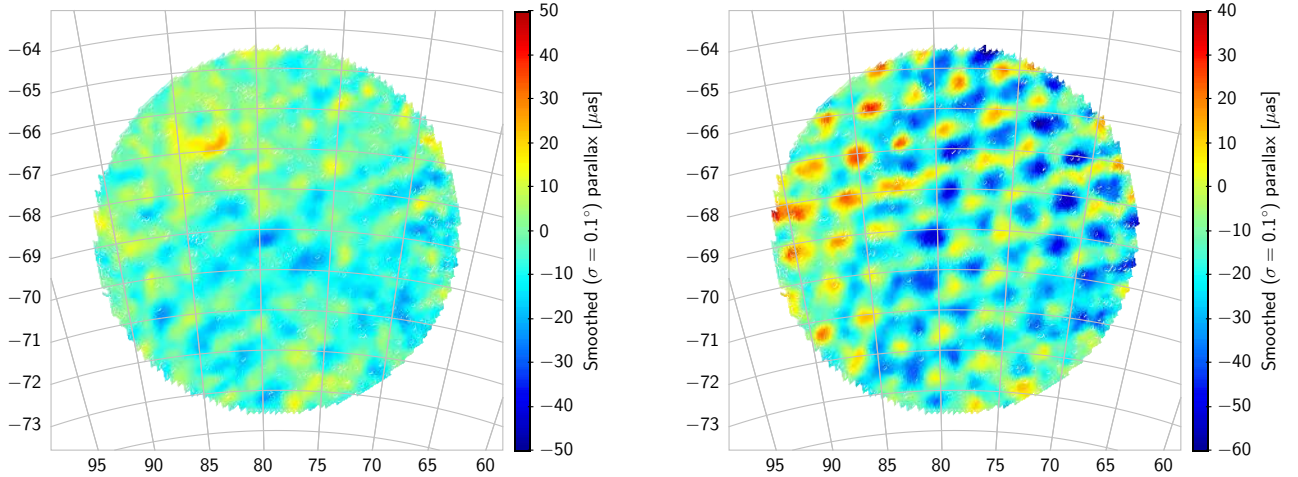


**Fig. 14.** Smoothed maps of parallaxes in the LMC area, visualising small-scale systematics (the “checkered pattern”) in *Gaia* EDR3 and DR2. *Left:* smoothed parallaxes in EDR3 for sources in the magnitude range  $G = 16$ –18 (median  $G = 17.4$ ), kinematically selected as probable members of the system (see Appendix B in [Lindegren et al. 2021](#) for details). *Right:* smoothed parallaxes in DR2 for the same sample of sources. Both maps were smoothed using a Gaussian kernel with standard deviation  $0.1^\circ$ . While the sample includes about 730 000 sources within  $5^\circ$  radius of the adopted centre, only smoothed points within a radius of  $4.5^\circ$  are shown to avoid unwanted edge effects. Comparison between the two diagrams is facilitated by the use of the same colour scale, only shifted by  $10 \mu\text{as}$  to compensate for the mean difference in parallax between DR2 and EDR3.

**Table 7.** RMS level of systematic errors in the quasar and LMC samples at different angular scales for EDR3 and (in brackets) DR2.

Sample	Angular scales	Parallax [ $\mu\text{as}$ ]	Proper motion [ $\mu\text{as yr}^{-1}$ ]
QSO	$>10^\circ$	8.1 (11.3)	7.7 (17.7)
QSO	$>7^\circ$	8.7 (12.6)	8.8 (20.1)
QSO	$>5^\circ$	9.4 (13.6)	9.6 (22.6)
QSO	$>3^\circ$	10.6 (14.8)	10.8 (24.>7)
QSO	$>2^\circ$	11.6 (15.5)	11.6 (26.3)
QSO	$>1^\circ$	13.5 (16.9)	12.8 (26.0)
QSO	$>0.5^\circ$	14.3 (23.2)	17.2 (23.2)
LMC	$0.1$ – $4.5^\circ$	6.9 (13.1)	

**Notes.** The lower limit in the second column is the standard deviation of the Gaussian smoothing kernel; the upper limit (for LMC) is the diameter of the area examined. Columns 3 and 4 give unbiased estimates of the RMS variations of the systematics, computed as described in the text. In brackets are the corresponding estimates for DR2, using as far as possible the same samples. For the proper motion, the values refer to a single component (the mean of the RMS in  $\mu_{\alpha^*}$  and  $\mu_\delta$ ).

obtained as the sample covariance between the smoothed values,  $\text{RMS} = \langle (s_A - \langle s_A \rangle)(s_B - \langle s_B \rangle) \rangle^{1/2}$ . Here  $\langle \rangle$  denotes an average over the positions (for the quasars, only  $|b| > 10^\circ$  was used; for the LMC, points within a radius of  $4.5^\circ$ ). Averaging over 50 different random divisions, we obtain the RMS values in Table 7. Compared with DR2 (values in brackets), the RMS systematics have improved by a factor 0.7 in the quasar parallaxes and 0.44 in the proper motions. For the small-scale parallax systematics in the LMC the improvement is a factor 0.53.

The RMS values in Table 7 for the quasars were computed using the full sample down to  $G = 21.0$  (median  $G = 19.9$ ), without taking into account that the individual uncertainties increase rapidly towards the faint end. This was done in order to benefit maximally from the large number of faint quasars in the sample. Unfortunately there are not enough of the brighter quasars to determine with any certainty how the systematics depend

on magnitude, but it appears that they improve marginally for brighter sources. For example, if the sample is restricted to the 16% quasars brighter than  $G = 19$  (median  $G = 18.4$ ), the RMS systematics are 10–15% smaller than in Table 7.

For the LMC, the RMS values in Table 7 were computed after subtraction of the mean observed parallax in the area, which means that they do not include systematics on angular scales  $\gtrsim 4.5^\circ$ . This explains why the RMS values in the last line break the increasing trends from the previous lines. The magnitude dependence mentioned above could also play a role here, the LMC sources being on average brighter than the quasars, as well as the geometrically favourable location near the south ecliptic pole.

Similarly to what was done for DR2, angular covariance functions of the parallaxes and proper motions,  $V_\varpi(\theta)$  and  $V_\mu(\theta)$ , have been computed for the EDR3 quasar sample. See Sect. 5.4 in [Lindegren et al. \(2018\)](#) for their definition<sup>7</sup>. The results (Fig. 15) are qualitatively similar to the DR2 results, but the covariances are smaller by a factor 2–4, consistent with other improvements. The black dashed curves in the upper panels are exponential fits for  $0.5^\circ \lesssim \theta \lesssim 80^\circ$ , namely

$$V_\varpi(\theta) \simeq (142 \mu\text{as}^2) \times \exp(-\theta/16^\circ), \quad (24)$$

$$V_\mu(\theta) \simeq (292 \mu\text{as}^2 \text{ yr}^{-2}) \times \exp(-\theta/12^\circ). \quad (25)$$

The corresponding amplitudes for DR2 were  $285 \mu\text{as}^2$  and  $800 \mu\text{as}^2 \text{ yr}^{-2}$ , with  $e$ -folding angles  $14^\circ$  and  $20^\circ$ . Taking the first bin ( $0 < \theta < 0.125^\circ$ ) to represent the covariance of the systematic errors at zero separation, we have

$$V_\varpi(0) \simeq 700 \mu\text{as}^2, \quad (26)$$

$$V_\mu(0) \simeq 550 \mu\text{as}^2 \text{ yr}^{-2}. \quad (27)$$

Corresponding values for DR2 were, respectively,  $1850 \mu\text{as}^2$  and  $4400 \mu\text{as}^2 \text{ yr}^{-2}$ .

<sup>7</sup> In the DR2 paper these functions were called spatial covariance functions. However, “angular” is a better qualifier, consistent with the established term “angular power spectrum” and avoiding the association to (three-dimensional) spatial coordinates.



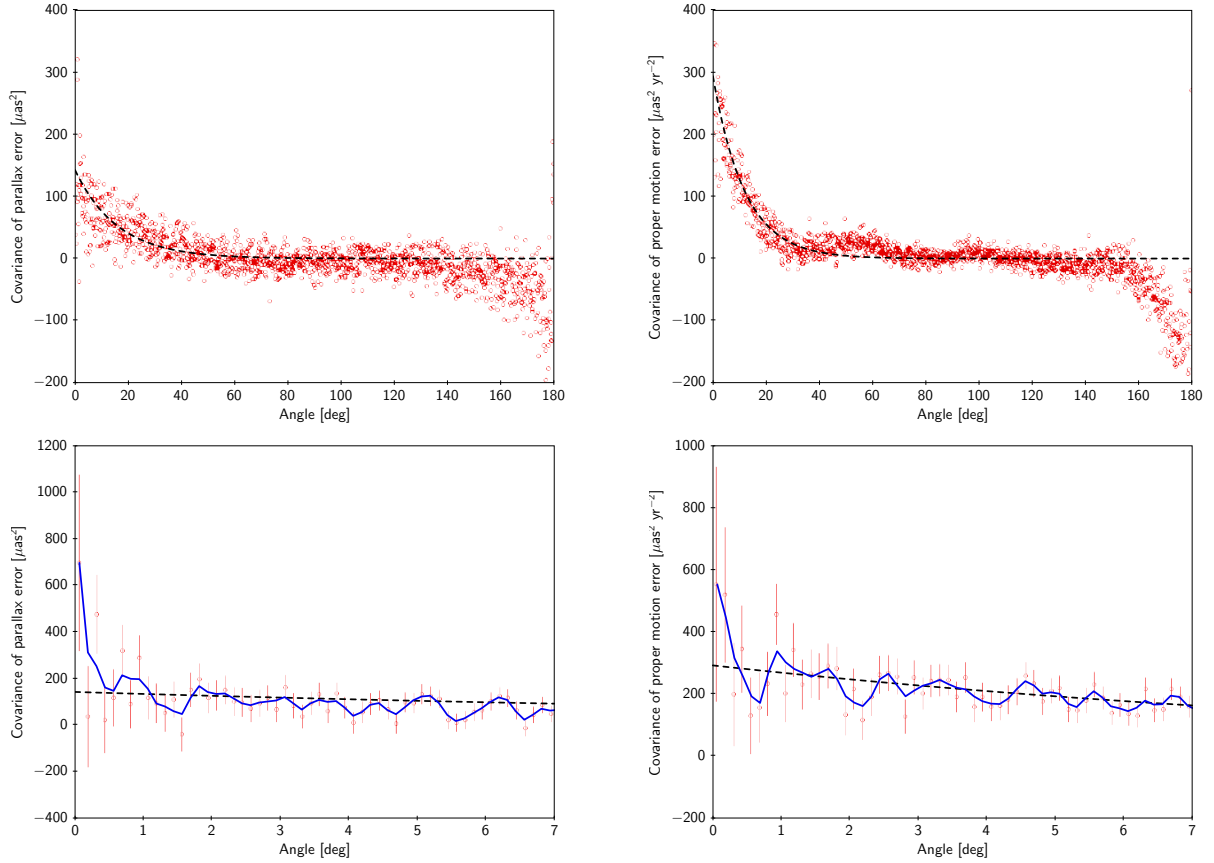


**Fig. 15.** Angular covariances of the five-parameter quasar sample. *Left:* covariance in parallax,  $V_{\varpi}(\theta)$ . *Right:* covariance in proper motion,  $V_{\mu}(\theta)$ . The red circles are the individual estimates; the dashed black curves are fitted exponential functions. The *bottom panels* show the same data as in the top panels, but for small separations only, with errors bars (68% confidence intervals) and running triangular mean values (blue curves).

Both  $V_{\varpi}(\theta)$  and  $V_{\mu}(\theta)$  show oscillations with a period of the order of a degree, corresponding to the checkered pattern. Consistent with the other findings, the oscillations in Fig. 15 have significantly smaller amplitudes than their counterparts in DR2.

### 5.7. Angular power spectrum of parallax bias

A comprehensive quantification of the positional variations of systematics on all angular scales can be given in the form of an angular power spectrum. This section is an attempt to estimate the power spectrum of parallax bias from EDR3 quasar data.

In astrophysics, the angular power spectrum is perhaps best known in the context of the cosmic microwave background (CMB; e.g. Hu Dodelson 2002). Any scalar field  $z(\alpha, \delta)$  defined on the full sky (temperature for the CMB; or in our case, the quasar parallaxes) can be decomposed in spherical harmonics (SH)  $Y_{\ell m}(\alpha, \delta)$  as

$$z(\alpha, \delta) = \sum_{\ell=0}^{\infty} \sum_{m=-\ell}^{\ell} a_{\ell m} Y_{\ell m}(\alpha, \delta), \quad (28)$$

where  $\ell$  is the degree of the SH (also known as multipole),  $m$  is the order (or mode), and  $a_{\ell m}$  are the (complex) coefficients

$$a_{\ell m} = \int_{\Omega} z(\alpha, \delta) Y_{\ell m}^* d\Omega. \quad (29)$$

Here  $*$  is the complex conjugate and  $\int_{\Omega}$  denotes integration over the full sphere with solid angle element  $d\Omega = \cos \delta d\alpha d\delta$ . The equivalence of Eqs. (28) and (29) can be verified using the orthonormality of the SH,  $\int_{\Omega} Y_{\ell m} Y_{\ell' m'}^* d\Omega = \delta^{\ell \ell'} \delta^{m m'}$ , where  $\delta^{ij}$  is the Kronecker symbol. By means of Eq. (28) it is seen that the mean square value of  $z$  on the sky is

$$\begin{aligned} \overline{z^2} &= \frac{1}{4\pi} \int_{\Omega} |z|^2 d\Omega = \frac{1}{4\pi} \int_{\Omega} \left( \sum_{\ell, m} a_{\ell m} Y_{\ell m} \right) \left( \sum_{\ell', m'} a_{\ell' m'}^* Y_{\ell' m'}^* \right) d\Omega \\ &= \frac{1}{4\pi} \int_{\Omega} \sum_{\ell, m} |a_{\ell m}|^2 |Y_{\ell m}|^2 d\Omega = \frac{1}{4\pi} \sum_{\ell=0}^{\infty} \sum_{m=-\ell}^{\ell} |a_{\ell m}|^2. \end{aligned} \quad (30)$$

The observed angular power spectrum, defined as

$$C_{\ell} = \frac{1}{2\ell + 1} \sum_{m=-\ell}^{\ell} |a_{\ell m}|^2 \quad (31)$$

(Peebles 1973; Hinshaw et al. 2003), thus measures the mean power of the SH components of degree  $\ell$ , that is on angular scales  $\sim 180^\circ/\ell$ , integrated over the sphere. For our purpose it is convenient to plot the cumulative quantity

$$R(\ell_{\max}) = \sqrt{\frac{1}{4\pi} \sum_{\ell=1}^{\ell_{\max}} (2\ell + 1) C_{\ell}}. \quad (32)$$

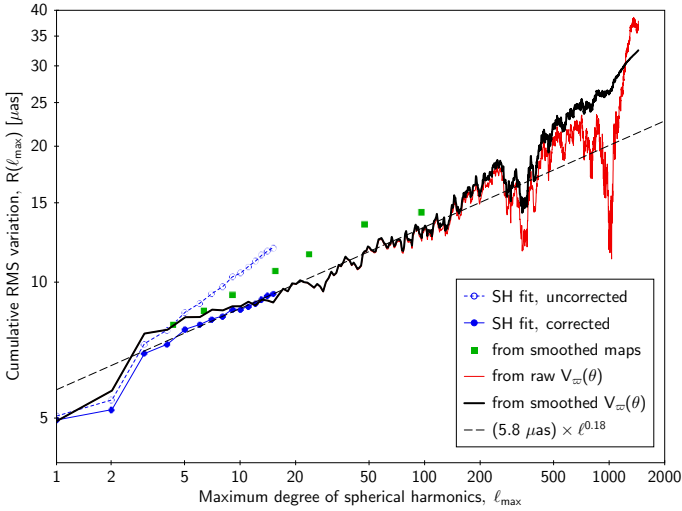


**Fig. 16.** Cumulative angular power spectrum of systematics in quasar parallaxes.

The spherical harmonic of degree  $\ell=0$ , corresponding to the mean quasar parallax of about  $-20 \mu\text{as}$ , is not included in the sum.  $R(\ell_{\text{max}})$  can therefore be interpreted as the RMS variation of the parallax systematics on angular scales  $\geq 180^\circ/\ell_{\text{max}}$ .

Figure 16 presents our estimates of the angular power spectrum of the parallax bias in EDR3, derived from the five-parameter quasar sample using several different methods. Most straightforward is to determine the coefficients  $a_{\ell m}$  by a weighted least-squares fit of Eq. (28) directly to the quasar parallaxes, truncating the first sum at  $\ell=L$  (that is, using  $L^2$  unknowns). Owing to the lack of quasars at low Galactic latitudes ( $|\sin b| < 0.1$ ), this gives stable results only for  $L \lesssim 15$  (angular scales  $\geq 12^\circ$ ), where the fit manages to bridge the no-data gap. Even so, the RMS values computed in this way (shown as open circles in Fig. 16) overestimate the true variations, as they include a contribution from the random errors in the parallaxes. If the random errors are assumed to have standard deviations equal to the formal parallax uncertainties, we can estimate their contribution to  $C_\ell$  by means of Monte Carlo simulations, and subtract from the power obtained in the fit. (Alternatively, the noise contributions could be estimated from the formal variances obtained in the least-squares fits.) This gives the corrected RMS estimates shown as filled circles in Fig. 16.

The smoothed maps offer an alternative method to estimate the angular power spectrum that is not restricted to  $\ell_{\text{max}} \lesssim 15$ , as was the case for the SH fit owing to the no-data gap along the Galactic equator. The RMS values in Table 7 were computed using only the smoothed points with  $|\sin b| > 0.1$ , and are therefore not strongly affected by the gap. However, the Gaussian smoothing does not correspond to a well-defined cut-off in  $\ell$ , and the comparison of the smoothed RMS values with  $R(\ell_{\text{max}})$  is not entirely straightforward. In Fig. 16 we have put the RMS values from the table at the degree where the Gaussian beam transfer function,  $\exp[-(\ell + \frac{1}{2})^2 \sigma^2]$  (White 1992), equals  $\frac{1}{2}$ , that is at  $\ell_{\text{max}} \approx 47.7^\circ/\sigma - 0.5$ . The RMS values, shown as green squares, roughly continue the power-law trend of the corrected SH fit to higher  $\ell_{\text{max}}$ , but at RMS values that are 10–15% higher. We have no explanation for this discrepancy, but conclude that the agreement is reasonable considering the approximations involved.

The angular covariance function  $V_\omega(\theta)$  and the angular power spectrum  $C_\ell$  contain equivalent information, and are related by the transformations (Peebles 1973)

$$C_\ell = 2\pi \int_{-1}^1 V_\omega(\theta) P_\ell(\cos \theta) d(\cos \theta), \quad (33)$$

$$V_\omega(\theta) = \frac{1}{4\pi} \sum_\ell (2\ell + 1) C_\ell P_\ell(\cos \theta), \quad (34)$$

where  $P_\ell(x)$  are Legendre polynomials. Using the angular covariance function in Fig. 15 (left) and replacing the integral in Eq. (33) by a sum over the 1440 covariance values, one can easily compute  $C_\ell$  for arbitrary  $\ell$ . The result is the red solid curve in Fig. 16. Using the smoothed covariance values (blue in Fig. 15, left) gives instead the black curve in Fig. 16. Both curves show some unphysical fluctuations: the cumulative RMS values cannot decrease for increasing  $\ell$ . The fluctuations are caused by sampling noise and must be disregarded when interpreting the RMS values, although they give an impression of the statistical uncertainties in  $R(\ell_{\text{max}})$ .

After accounting for estimation bias in the SH fit there is generally good agreement between the different methods where they overlap. On the smallest scales,  $\ell_{\text{max}} \geq 100$ , only the angular covariance function provides an estimate. As indicated by the dashed line in Fig. 16, the overall trend can be described by a simple power law

$$R(\ell_{\text{max}}) \approx (5.8 \mu\text{as}) \times \ell^{0.18}, \quad (35)$$

at least for  $\ell=3$  to  $\approx 150$  (angular scales from  $1.2^\circ$  to  $60^\circ$ ). For  $\ell=1$  and 2 the RMS is significantly smaller than according to this relation. In particular, the power at  $\ell=2$  (angle  $\sim 90^\circ$ ) is remarkably small, which could be related to the basic angle ( $\Gamma = 106.5^\circ$ ) providing a firm connection between areas separated by angles of the order of  $90^\circ$ . For  $\ell \geq 150$  the RMS is higher than according to the power law, corresponding to the “checkered pattern” in Fig. 14 (left). The value  $V_\omega(0) \approx 700 \mu\text{as}^2$  in Eq. (26) for  $\theta < 0.125^\circ$  suggests that  $R(\ell_{\text{max}})$  saturates at  $\approx 26 \mu\text{as}$  for  $\ell_{\text{max}} \geq 1440$ . Using a suitable (monotonic) model function  $R(\ell_{\text{max}})$  one can estimate the values  $C_\ell$ , which may be of interest in studies where the statistical variation of parallax bias with position is a concern.

No angular power spectrum is given for the systematics in quasar proper motions. Large-scale systematics (for small  $\ell$ ) are discussed in Gaia Collaboration (in prep.) and Gaia Collaboration (2021b).

## 6. Improvements for Gaia DR4 and beyond

Although EDR3 brings huge improvements over DR2 in terms of the overall quality of the astrometric results, including systematics, it is obvious that the limits of *Gaia*’s capability have not been reached. At the time of writing (September 2020), *Gaia* has already accumulated more than twice the amount of observations included in EDR3, and a solution using all these data, even without any improved modelling, will almost certainly bring down the random errors by a factor 0.7 for the positions and parallaxes, and by a factor 0.35 for the proper motions. Some of the systematics will also be reduced simply from the improved coverage in time and scan directions. But important advances will also come from dedicated efforts to improve and consolidate the calibration models. In this context it is positive that many model deficiencies stand out clearly in the residuals (e.g. Appendices A.2 and

A.3): it shows that the modelling errors are not degenerate with the astrometry and can be used to design better models. Below we list some areas where significant advances should be possible as a result of further model developments and analysis of the data.

### 6.1. LSF and PSF modelling

The processing of CCD samples in CALIPD is intimately connected to the AGIS calibrations through the many instrumental effects that influence the shape and location of the image profiles. As detailed by Rowell et al. (2021), significant improvements to the LSF and PSF modelling are being implemented or planned for DR4 and subsequent cycles. These include improved basis functions for the LSF and PSF modelling, with an analytical representation of AL and AC smearing effects and a clear separation between parameters representing a shift of the profile and its shape; modelling of magnitude-dependent non-linear effects, caused for example by CTI; and a new bootstrapping of the attitude and geometric calibrations that will make the initial CALIPD in a cycle more independent of the previous cycle, thus reducing the risk of propagating systematics from one cycle to the next. It is expected that these many developments will further reduce systematics in the location and flux estimates per CCD coming from the IPD. This will benefit the astrometry and photometry of all sources, but in particular the bright ones ( $G \lesssim 13$ ).

### 6.2. CTI modelling

As shown in Appendix A.3, the AL and AC residuals exhibit strong trends with magnitude that can be interpreted as a manifestation of CTI. CTI effects are also diagnosed, but not corrected, by the CTI calibration parameters displayed in Fig. A.3. The effects may already have some impact on the astrometry, and this will become more important with time as the accumulated radiation dose increases while random errors in the astrometric results continue to improve. Whereas ultimately a detailed, physics-based modelling of CTI effects is desirable (Prod'homme et al. 2011; Short et al. 2013), much progress is still possible simply by better mapping of the empirical effect as a function of the main variables of the observation. On this macroscopic level, CTI is comparatively easy to separate from other effects, thanks to the periodic charge injection, and a wealth of additional calibration data are available to support the modelling (Crowley et al. 2016).

### 6.3. Time variations

With the exception of the spin-related (quasi-periodic) distortion discussed in Sect. 3.4, all instrument calibrations are assumed to be constant or at most linearly varying over a time interval that could be as long as 63 days. For the AL large-scale geometry the time interval is at most 3 days. The residual normal points in Fig. A.2 show that this resolution is adequate most of the time, but not always and especially not after thermal upsets such as the (partial) eclipses of the Sun by the Moon. Clearly a quadratic model (or perhaps an exponential model with fixed time constant) would be a big improvement at these times. The spin-related periodicity of the residuals, visible along most of the time axis in the diagram, may be removed by the more extended VBAC/FOC modelling hinted at in Sect. 3.4.

### 6.4. AC rate dependency

The AC rate has a big impact on the PSF by smearing the images in the AC direction during a CCD exposure. The width of the PSF in the AC direction is increased by the smearing, and the number of photoelectrons per pixel is reduced, which affects saturation and CTI. The AC rate is therefore relevant for the calibration of both bright and faint sources. To first order, the smearing is proportional to  $|\dot{\zeta}|^2$ , which is the only dependence considered in the AGIS calibration model for EDR3 (effect 7 in Table 2). Owing to the non-linearity of saturation and CTI effects, it is likely that the AL centroid biases they produce also have a component that is linear in  $\dot{\zeta}$ . Such terms were not included in the AL calibration model for EDR3, as they might be difficult to disentangle from the parallax in view of the correlation between  $\dot{\zeta}$  and the AL parallax factor described in Appendix B. This correlation is positive throughout the data segments used for EDR3, but negative in data segments DS6 and DS7 where reversed precession was used. The reversed precession during one year (2019.536–2020.576; cf. Fig. 1) was introduced precisely to address this and similar issues related to the non-symmetry of the nominal scanning law. Together with the much improved PSF modelling mentioned above, this should allow the main effects of AC rate variations to be resolved already in the data analysis for DR4, which includes data segment DS6 obtained in reversed precession mode.

### 6.5. Use of colour information

A rather unsatisfactory aspect of EDR3 is the division of sources with full astrometric information into two distinct subsets, namely the five- and six-parameter solutions. This was a consequence of the unavailability of good colour information for some sources, which necessitated their special treatment in IPD and AGIS. Although much more and better colour information from the BP and RP spectra is available for DR4 through PhotPipe 3 (cf. Fig. 1), it is unavoidable that this information is missing or of poor quality for some sources. A more uniform treatment of all sources in IPD and AGIS can be achieved by consistently using the available colour information, weighted according to its uncertainty. For AGIS this means that all sources obtain six-parameter solutions, but with available BP and RP data used as prior for the pseudocolour.

## 7. Conclusions

Compared with *Gaia* DR2, the number of sources in EDR3 that have a parallax and proper motion is only 10% higher. However, the average improvement on the standard uncertainties is roughly a factor 0.8 for the positions and parallaxes, and 0.5 for the proper motions. These factors reflect the higher number of observations per source, by more than 50% on average, and the longer time span of the data, which make the astrometric results considerably more robust and help to reduce systematic errors. The astrometric solution for EDR3 is also the first one in the cyclic processing of DPAC to benefit from a full reprocessing of the LSF and PSF calibrations and the image parameter determination. The next full-scale astrometric solution, for *Gaia* DR4, will be based on twice as many observations as EDR3. Considerable efforts are required and planned to ensure a matching development of models and analysis methods.

*Acknowledgements.* We thank the anonymous referee for constructive comments on the manuscript and C. Babusiaux for pointing out a significant error in the



original version. This work has made use of data from the European Space Agency (ESA) mission *Gaia* (<https://www.cosmos.esa.int/gaia>), processed by the *Gaia* Data Processing and Analysis Consortium (DPAC, <https://www.cosmos.esa.int/web/gaia/dpac/consortium>). Funding for the DPAC has been provided by national institutions, in particular the institutions participating in the *Gaia* Multilateral Agreement. This work was financially supported by the European Space Agency (ESA) in the framework of the *Gaia* project; the German Aerospace Agency (Deutsches Zentrum für Luft- und Raumfahrt e.V., DLR) through grants 50QG0501, 50QG0601, 50QG0901, 50QG1401 and 50QG1402; the Spanish Ministry of Economy (MINECO/FEDER, UE) through grants ESP2016-80079-C2-1-R, RTI2018-095076-B-C21 and the Institute of Cosmos Sciences University of Barcelona (ICCUB, Unidad de Excelencia “María de Maeztu”) through grants MDM-2014-0369 and CEX2019-000918-M; the Swedish National Space Agency (SNSA/Rymdstyrelsen); and the United Kingdom Particle Physics and Astronomy Research Council (PPARC), the United Kingdom Science and Technology Facilities Council (STFC), and the United Kingdom Space Agency (UKSA) through the following grants to the University of Bristol, the University of Cambridge, the University of Edinburgh, the University of Leicester, the Mullard Space Sciences Laboratory of University College London, and the United Kingdom Rutherford Appleton Laboratory (RAL): PP/D006511/1, PP/D006546/1, PP/D006570/1, ST/I000852/1, ST/J005045/1, ST/K00056X/1, ST/K000209/1, ST/K000756/1, ST/L006561/1, ST/N000595/1, ST/N000641/1, ST/N000978/1, ST/N001117/1, ST/S000089/1, ST/S000976/1, ST/S001123/1, ST/S001948/1, ST/S002103/1, and ST/V000969/1. The authors gratefully acknowledge the use of computer resources from MareNostrum, and the technical expertise and assistance provided by the Red Española de Supercomputación at the Barcelona Supercomputing Center, Centro Nacional de Supercomputación. We thank the Centre for Information Services and High Performance Computing (ZIH) at the Technische Universität (TU) Dresden for generous allocations of computer time. Diagrams were produced using the astronomy-oriented data handling and visualisation software TOPCAT (Taylor 2005).

## References

- Arenou, F., Luri, X., Babusiaux, C., et al. 2018, *A&A*, **616**, A17
- Bombrun, A., Lindegren, L., Hobbs, D., et al. 2012, *A&A*, **538**, A77
- Brandt, T. D. 2018, *ApJS*, **239**, 31
- Butkevich, A. G., Klioner, S. A., Lindegren, L., Hobbs, D., & van Leeuwen, F. 2017, *A&A*, **603**, A45
- Charlot, P., Jacobs, C. S., Gordon, D., et al. 2020, *A&A*, **644**, A159
- Crowley, C., Kohley, R., Hambly, N. C., et al. 2016, *A&A*, **595**, A6
- Dravins, D., Lindegren, L., & Madsen, S. 1999, *A&A*, **348**, 1040
- ESA 1997, *ESA SP*, **1200**
- Evans, D. W., Riello, M., De Angeli, F., et al. 2018, *A&A*, **616**, A4
- Fabrigius, C., Bastian, U., Portell, J., et al. 2016, *A&A*, **595**, A3
- Fabrigius, C., Luri, X., Arenou, F., et al. 2021, *A&A*, **649**, A5 (*Gaia* EDR3 SI)
- Fienga, A., Manche, H., Laskar, J., Gastineau, M., & Verma, A. 2016, *Notes Scientifiques et Techniques de l’Institut de Mécanique Céleste*, 104
- Gaia Collaboration (Prusti, T., et al.) 2016a, *A&A*, **595**, A1
- Gaia Collaboration (Brown, A. G. A., et al.) 2016b, *A&A*, **595**, A2
- Gaia Collaboration (Brown, A. G. A., et al.) 2021a, *A&A*, **649**, A1 (*Gaia* EDR3 SI)
- Gaia Collaboration (Klioner, S. A., et al.) 2021b, *A&A*, **649**, A9 (*Gaia* EDR3 SI)
- Górski, K. M., Hivon, E., Banday, A. J., et al. 2005, *ApJ*, **622**, 759
- Hambly, N. C., Cropper, M., Boudreault, S., et al. 2018, *A&A*, **616**, A15
- Hinshaw, G., Spergel, D. N., Verde, L., et al. 2003, *ApJS*, **148**, 135
- Holl, B., Audard, M., Nienartowicz, K., et al. 2018, *A&A*, **618**, A30
- Hu, W., & Dodelson, S. 2002, *ARA&A*, **40**, 171
- Klioner, S. A. 2003, *AJ*, **125**, 1580
- Klioner, S. A. 2004, *Phys. Rev. D*, **69**, 124001
- Klioner, S. A., Geyer, R., Steidelmüller, H., & Butkevich, A. G. 2017, *Space Sci. Rev.*, **212**, 1423
- Kovalevsky, J., Lindegren, L., Perryman, M. A. C., et al. 1997, *A&A*, **323**, 620
- Lindegren, L. 2020a, *A&A*, **633**, A1
- Lindegren, L. 2020b, *A&A*, **637**, C5
- Lindegren, L., Lammers, U., Hobbs, D., et al. 2012, *A&A*, **538**, A78 (The AGIS paper)
- Lindegren, L., Hernández, J., Bombrun, A., et al. 2018, *A&A*, **616**, A2
- Lindegren, L., Bastian, U., Biermann, M., et al. 2021, *A&A*, **649**, A4 (*Gaia* EDR3 SI)
- Michalik, D., Lindegren, L., Hobbs, D., & Butkevich, A. G. 2015, *A&A*, **583**, A68
- Mora, A., Biermann, M., Bombrun, A., et al. 2016, *Proc. SPIE*, **9904**, 99042
- Peebles, P. J. E. 1973, *ApJ*, **185**, 413
- Press, W., Teukolsky, S., Vetterling, W., & Flannery, B. 2007, *Numerical Recipes 3rd Edition: The Art of Scientific Computing* (Cambridge: Cambridge University Press)
- Prod’homme, T., Brown, A. G. A., Lindegren, L., Short, A. D. T., & Brown, S. W. 2011, *MNRAS*, **414**, 2215
- Riello, M., De Angeli, F., Evans, D. W., et al. 2021, *A&A*, **649**, A3 (*Gaia* EDR3 SI)
- Rowell, N., Davidson, M., Lindegren, L., et al. 2021, *A&A*, **649**, A11 (*Gaia* EDR3 SI)
- Saad, Y. 2003, *Iterative Methods for Sparse Linear Systems*, 2nd edn. (Philadelphia: Society for Industrial and Applied Mathematics)
- Sartoretti, P., Katz, D., Cropper, M., et al. 2018, *A&A*, **616**, A6
- Short, A., Crowley, C., de Bruijne, J. H. J., & Prod’homme, T. 2013, *MNRAS*, **430**, 3078
- Söderhjelm, S. 2005, *ESA SP*, **576**, 97
- Soffel, M., Klioner, S. A., Petit, G., et al. 2003, *AJ*, **126**, 2687
- Taylor, M. B. 2005, *ASP Conf. Ser.*, **347**, 29
- Torra, F., Castañeda, J., Fabricius, C., et al. 2021, *A&A*, **649**, A10 (*Gaia* EDR3 SI)
- van Leeuwen, F. 2007, *Hipparcos, the New Reduction of the Raw Data, Astrophysics and Space Science Library*, 350
- White, M. 1992, *Phys. Rev. D*, **46**, 4198

<sup>1</sup> Lund Observatory, Department of Astronomy and Theoretical Physics, Lund University, Box 43, 22100 Lund, Sweden  
e-mail: [lennart@astro.lu.se](mailto:lennart@astro.lu.se)

<sup>2</sup> Lohrmann Observatory, Technische Universität Dresden, Mommsenstraße 13, 01062 Dresden, Germany

<sup>3</sup> European Space Agency (ESA), European Space Astronomy Centre (ESAC), Camino bajo del Castillo, s/n, Urbanización Villafraanca del Castillo, Villanueva de la Cañada, 28692 Madrid, Spain

<sup>4</sup> HE Space Operations BV for European Space Agency (ESA), Camino bajo del Castillo, s/n, Urbanización Villafraanca del Castillo, Villanueva de la Cañada, 28692 Madrid, Spain

<sup>5</sup> Vitrociset Belgium for European Space Agency (ESA), Camino bajo del Castillo, s/n, Urbanización Villafraanca del Castillo, Villanueva de la Cañada, 28692 Madrid, Spain

<sup>6</sup> Astronomisches Rechen-Institut, Zentrum für Astronomie der Universität Heidelberg, Mönchhofstr. 12-14, 69120 Heidelberg, Germany

<sup>7</sup> Telespazio Vega UK Ltd for European Space Agency (ESA), Camino bajo del Castillo, s/n, Urbanización Villafraanca del Castillo, Villanueva de la Cañada, 28692 Madrid, Spain

<sup>8</sup> DAPCOM for Institut de Ciències del Cosmos (ICCUB), Universitat de Barcelona (IEEC-UB), Martí i Franquès 1, 08028 Barcelona, Spain

<sup>9</sup> Institute for Astronomy, University of Edinburgh, Royal Observatory, Blackford Hill, Edinburgh EH9 3HJ, UK

<sup>10</sup> Institut de Ciències del Cosmos (ICCUB), Universitat de Barcelona (IEEC-UB), Martí i Franquès 1, 08028 Barcelona, Spain

<sup>11</sup> Gaia DPAC Project Office, ESAC, Camino bajo del Castillo, s/n, Urbanización Villafraanca del Castillo, Villanueva de la Cañada, 28692 Madrid, Spain

<sup>12</sup> INAF – Osservatorio Astrofisico di Torino, via Osservatorio 20, 10025 Pino Torinese (TO), Italy

<sup>13</sup> SYRTE, Observatoire de Paris, Université PSL, CNRS, Sorbonne Université, LNE, 61 avenue de l’Observatoire 75014 Paris, France

<sup>14</sup> ATG Europe for European Space Agency (ESA), Camino bajo del Castillo, s/n, Urbanización Villafraanca del Castillo, Villanueva de la Cañada, 28692 Madrid, Spain

<sup>15</sup> Max Planck Institute for Astronomy, Königstuhl 17, 69117 Heidelberg, Germany

<sup>16</sup> INAF – Osservatorio Astrofisico di Catania, via S. Sofia 78, 95123 Catania, Italy

<sup>17</sup> Center for Research and Exploration in Space Science and Technology, University of Maryland Baltimore County, 1000 Hilltop Circle, Baltimore MD, USA

- <sup>18</sup> GSFC – Goddard Space Flight Center, Code 698, 8800 Greenbelt Rd, 20771 MD Greenbelt, USA
- <sup>19</sup> EURIX S.r.l., Corso Vittorio Emanuele II 61, 10128 Torino, Italy
- <sup>20</sup> Leiden Observatory, Leiden University, Niels Bohrweg 2, 2333 CA Leiden, The Netherlands
- <sup>21</sup> University of Turin, Department of Computer Sciences, Corso Svizzera 185, 10149 Torino, Italy
- <sup>22</sup> Laboratoire d’astrophysique de Bordeaux, Univ. Bordeaux, CNRS, B18N, allée Geoffroy Saint-Hilaire, 33615 Pessac, France
- <sup>23</sup> Leibniz Institute for Astrophysics Potsdam (AIP), An der Sternwarte 16, 14482 Potsdam, Germany
- <sup>24</sup> Aurora Technology for European Space Agency (ESA), Camino bajo del Castillo, s/n, Urbanizacion Villafranca del Castillo, Villanueva de la Cañada, 28692 Madrid, Spain
- <sup>25</sup> RHEA for European Space Agency (ESA), Camino bajo del Castillo, s/n, Urbanizacion Villafranca del Castillo, Villanueva de la Cañada, 28692 Madrid, Spain
- <sup>26</sup> Université Côte d’Azur, Observatoire de la Côte d’Azur, CNRS, Laboratoire Géoazur, Bd de l’Observatoire, CS 34229, 06304 Nice Cedex 4, France
- <sup>27</sup> IMCCE, Observatoire de Paris, Université PSL, CNRS, Sorbonne Université, Univ. Lille, 77 av. Denfert-Rochereau, 75014 Paris, France
- <sup>28</sup> TRUMPF Photonic Components GmbH, Lise-Meitner-Straße 13, 89081 Ulm, Germany
- <sup>29</sup> SRON, Netherlands Institute for Space Research, Sorbonnelaan 2, 3584CA Utrecht, The Netherlands
- <sup>30</sup> University of Turin, Department of Physics, Via Pietro Giuria 1, 10125 Torino, Italy
- <sup>31</sup> Las Cumbres Observatory, 6740 Cortona Drive Suite 102, Goleta, CA 93117, USA
- <sup>32</sup> Astrophysics Research Institute, Liverpool John Moores University, 146 Brownlow Hill, Liverpool L3 5RF, UK
- <sup>33</sup> Université Côte d’Azur, Observatoire de la Côte d’Azur, CNRS, Laboratoire Lagrange, Bd de l’Observatoire, CS 34229, 06304 Nice Cedex 4, France
- <sup>34</sup> School of Physics and Astronomy, University of Leicester, University Road, Leicester LE1 7RH, UK
- <sup>35</sup> GEPI, Observatoire de Paris, Université PSL, CNRS, 5 Place Jules Janssen, 92190 Meudon, France
- <sup>36</sup> Department of Astrophysical Sciences, 4 Ivy Lane, Princeton University, Princeton NJ 08544, USA
- <sup>37</sup> LESIA, Observatoire de Paris, Université PSL, CNRS, Sorbonne Université, Université de Paris, 5 Place Jules Janssen, 92190 Meudon, France
- <sup>38</sup> naXys, University of Namur, Rempart de la Vierge, 5000 Namur, Belgium

## Appendix A: Properties of the astrometric solution

This Appendix illustrates properties of the primary astrometric solution in AGIS 3.2 that cannot be derived from the published *Gaia* EDR3 results but require access to (unpublished) data internal to AGIS, such as calibration data and the residuals of individual CCD observations. Obviously, only a very limited selection from the available material can be shown.

### A.1. Dispersion of residuals

In Fig. A.1 we compare the photon-statistical uncertainties of the individual AL angular measurements with the scatter (RSE<sup>8</sup>) of post-fit residuals in the astrometric solution. For convenience, the corresponding curves for the DR2 astrometry (Fig. 10 in Lindegren et al. 2018) are shown by the dashed curves. While the formal precision of the individual observations is practically unchanged from DR2, the actual residuals have been reduced roughly by a factor two for  $G \lesssim 13$ , thanks to the improved calibration models in IDU and AGIS. This will surely continue to improve in future releases. For the fainter magnitudes, the improvement is successively smaller; for  $G \gtrsim 17$  it is negligible because the residuals are completely dominated by photon-statistical errors.

Plotting the along-scan residuals of the individual observations from the primary solution (Sect. 4.2) versus quantities such as time and magnitude is a powerful way to check the modelling of attitude and calibration in AGIS. For meaningful results, it is usually necessary to divide the data according to different categories such as FoV, CCD, window class, and gate. As the modelling errors are typically much smaller than the random errors, it is also necessary to reduce the random scatter, for example by plotting mean or median values. In the following sections we give examples of such plots versus time, magnitude, and AC rate, illustrating some known inadequacies of the calibration models used for EDR3.

### A.2. Mean residual versus time

Figure A.2 shows residual normal points, separately for the two FoVs, for the entire time interval covered by the solution. The normal points are weighted averages of the AL residuals in the AGIS 3.2 primary solution, calculated in time bins of 87 s using the same weights as in the solution (Eq. (62) in Lindegren et al. 2012). All residuals were used, except those in window class WC0b, which have a distinctly different (and worse) behaviour than the other window classes. The mean number of residuals per (non-empty) bin is  $\sim 2800$ , yielding a statistical uncertainty of about  $4 \mu\text{as}$  per normal point. The figure shows at a glance not only the major gaps in the data (cf. Table 1), but also specific intervals where the modelling was clearly inadequate. By zooming in on the plot, a wealth of interesting details can be seen. Most conspicuous are the large (up to  $\pm 100 \mu\text{as}$ ) systematic differences between the preceding and following FoVs seen for example after the phased array antenna anomalies (e.g. for OBMT 1661–1672 rev) and eclipses by the Moon (e.g. for OBMT 2958–2970 rev), where the AL large-scale calibration model (effect 1 in Table 2), assuming linear variations over an interval of 3 days (12 rev), cannot represent the non-linear

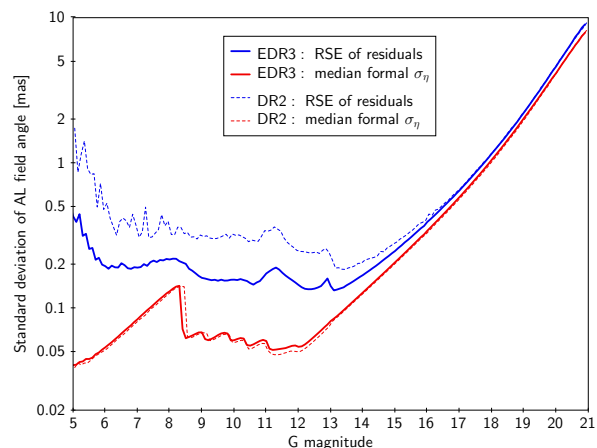


**Fig. A.1.** Precision of along-scan astrometric measurements as a function of magnitude. Solid curves are for EDR3, dashed for DR2. The red (lower) curves show the median formal precisions from the image parameter determination; the blue (upper) curves are robust estimates<sup>8</sup> of the actual standard deviations of the post-fit residuals.

behaviour of the instrument while it is striving towards thermal equilibrium. (Not much of this effect is seen after the decontaminations, which are much more severe thermal upsets, because data were discarded in a much longer interval after these events.) The distinctly higher noise around OBMT 1908–1911 and 2525–2534 rev coincides with intervals where the corrective attitude (Sect. 3.2) was missing because of a processing error. The overall dispersion of the normal points, as measured by the RSE, is  $14.9 \mu\text{as}$  in the PFoV and  $16.6 \mu\text{as}$  in the FFoV. The slightly better performance in the PFoV is a common feature in much of the *Gaia* data (see, for example, several plots in Rowell et al. 2021). At most times a small residual of the 6 h and 3 h basic angle variations can be seen.

The increased residuals at certain times, shown in Fig. A.2, are reflected in the AL excess attitude noise, which is the mechanism in AGIS for applying a time-dependent adjustment of the statistical weight of observations. (As explained in Sect. 3.6 of Lindegren et al. 2012, the excess noise is the additional RMS noise that must be postulated in the AL error budget in order to account for the post-fit residuals. It consists of two parts: the excess source noise, which is linked to a particular source, and the excess attitude noise, which is linked to a particular time. While the excess attitude noise is meant to represent attitude modelling errors, it can just as well represent calibration errors that affect the observations of all sources at a given time.) This is illustrated in Fig. A.3, where the AL excess attitude noise is shown versus time for two 25-day intervals. In the top panel, which is the same time interval as row five in Fig. A.2, the excess attitude noise is seen to exactly mirror the amplitude of the residual normal points at OBMT 1660–1672 rev. In the bottom panel of Fig. A.3, which corresponds to row eight in Fig. A.2, the absence of a corrective attitude at OBMT 1908–1911 rev triples the excess attitude noise compared with neighbouring times. A 6 h (or 3 h) periodicity is very often apparent in the excess attitude noise, as in OBMT 1940–1950 rev. The overall median AL excess attitude noise in EDR3 is  $76 \mu\text{as}$ , which represents the average total instrument modelling error for WC1 observations.

### A.3. Mean residual versus magnitude

The left panel of Fig. A.4 shows the mean AL residual versus  $G$  magnitude for the 14.3 million primary sources in AGIS 3.2

<sup>8</sup> The robust scatter estimate (RSE) is defined as  $[2\sqrt{2}\text{erf}^{-1}(4/5)]^{-1} \approx 0.390152$  times the difference between the 90th and 10th percentiles of the distribution of the variable. For a Gaussian distribution it equals the standard deviation. The RSE is used as a standardised, robust measure of dispersion in CU3.



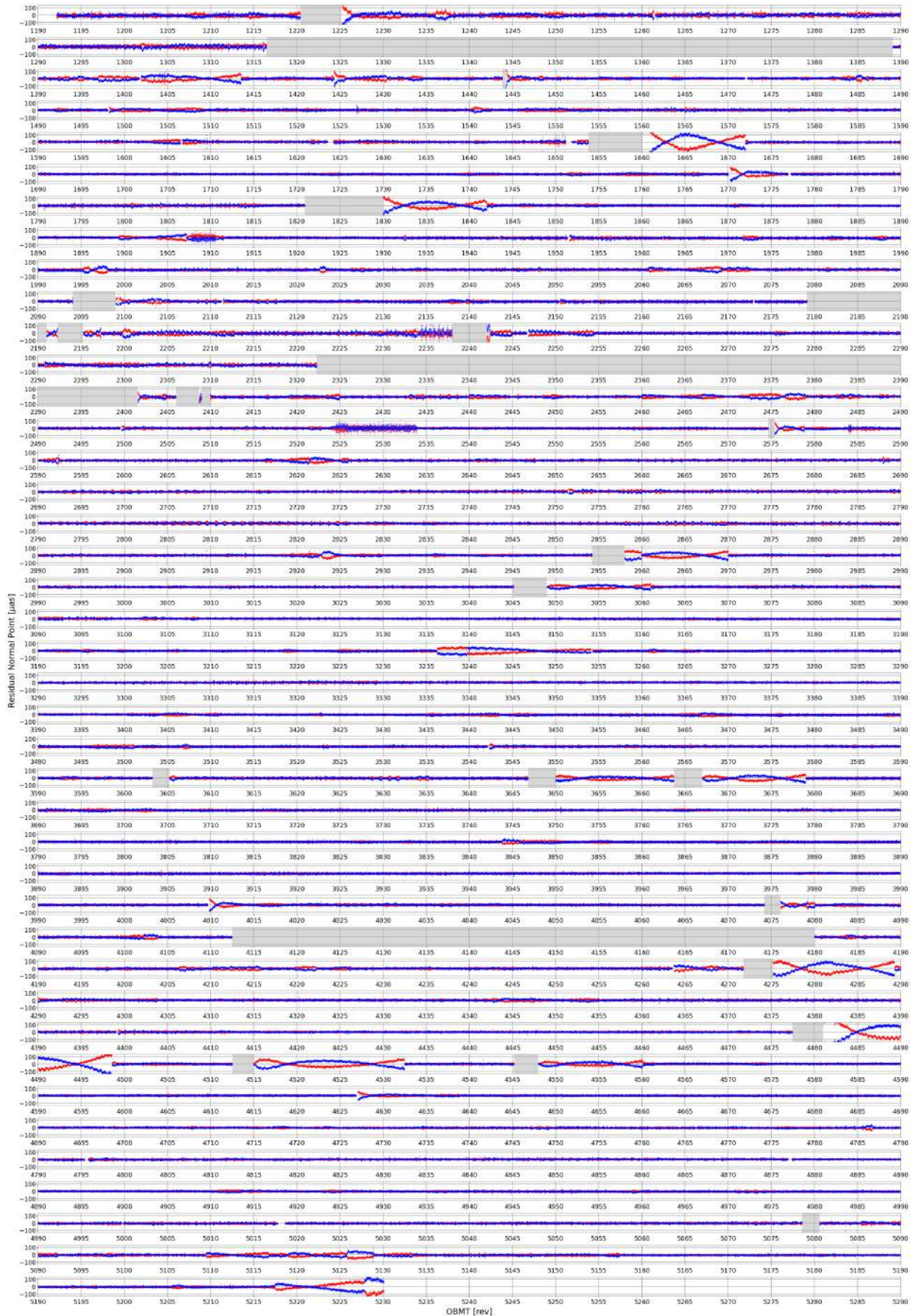


**Fig. A.2.** Residual normal points vs. time (OBMT). Blue and red points are, respectively, for the PFoV and FFoV. Each of the 41 rows covers a time interval of 100 revolutions or 25 days. The grey areas correspond to the gaps in Table 1.

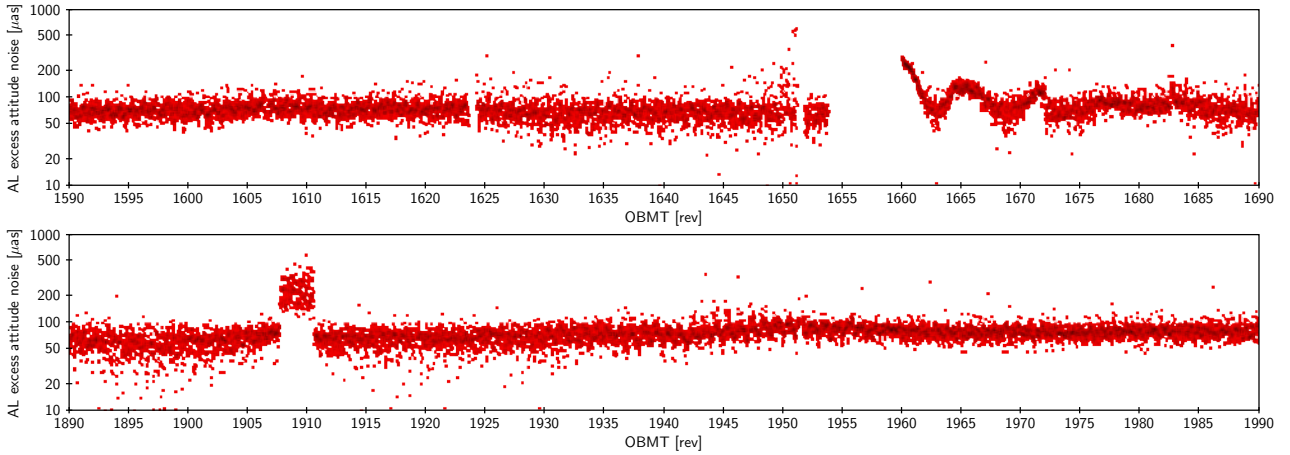


**Fig. A.3.** Excess attitude noise in two 25-day intervals.

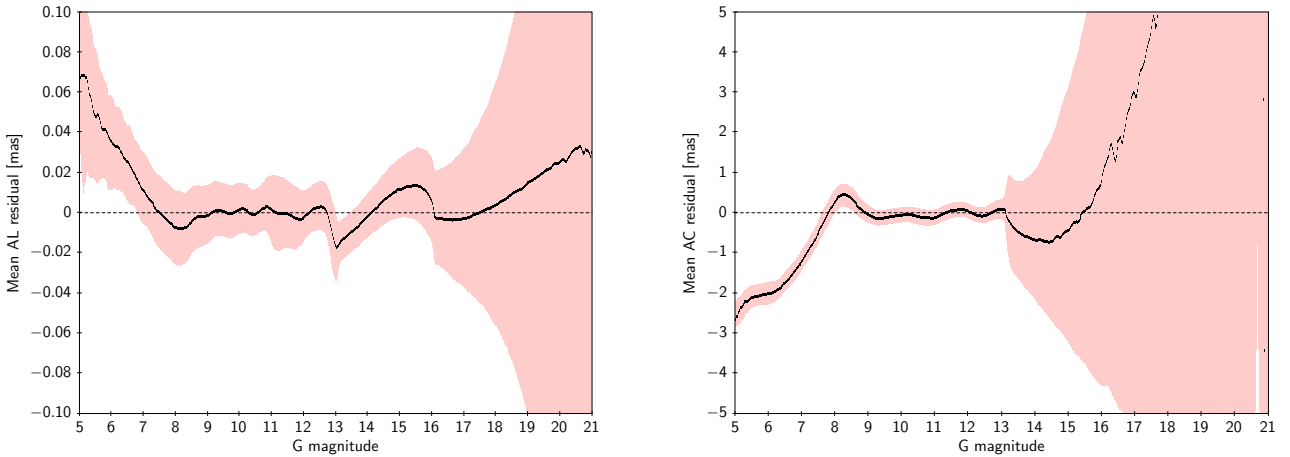


**Fig. A.4.** Mean residual AL (*left*) and AC (*right*) vs. magnitude for the primary sources. A mean residual (AL and AC) is computed for each source. The black curve is the median of these values, and the shaded areas indicates their 16th and 84th percentiles.

(Sect. 4.2). The plot actually shows quantiles of the mean residual per source, so the dispersion indicated by the shaded area is nearly 20 times smaller than the dispersion of individual residuals as shown in Fig. A.1 (on average there are 363 AL observations per source).

The right panel of Fig. A.4 is the corresponding plot for the AC residuals. AC observations require two-dimensional windows (WC0), which are normally used only for sources brighter than  $G \approx 13$ . Only occasionally do the fainter sources by chance get two-dimensional windows and AC observations, which explains the sudden increase in the dispersion at that magnitude: The mean number of AC observations per source is 357 for  $G < 13$  and 0.5 for  $G > 13$ . The AC calibration is reasonably good in the magnitude interval 9–13, which includes most of the AC observations needed for the attitude determination.

The mean AL residual is non-zero on a level of a few tens of  $\mu\text{as}$ , with clear and strong trends versus magnitude. Discontinuities are seen at the WC0/1/2 boundaries at  $G = 13$  and 16. It is likely that CTI is a major factor in producing these systematics. This effect is expected to produce a delay of the charge packages transported along the CCDs, creating a positive bias in the observed AL field angle  $\eta$  that generally increases with magnitude. This is consistent with the main trends seen within WC1 ( $G = 13$ –16) and WC2 ( $G > 16$ ). For  $G < 13$  the situation is more complex because of the gates and (for  $G \lesssim 8$ ) the partial

saturation of images. An interpretation in terms of CTI is supported by the similarity of the effect in the two FoVs, in spite of the considerable variation among the different CCDs (Fig. A.5). This suggests that the effect is not primarily driven by the shape of the LSF or PSF, which is usually quite different in the two FoVs, but by intrinsic properties of the CCDs.

#### A.4. Astrometric calibration

Of the various calibration effects summarised in Table 2, only selected results on the AL chromaticity and CTI effect are shown here and briefly commented on.

Figures A.6 and A.7 show the AL large-scale colour calibration (effect 3 in Table 2) as a function of time for five of the CCDs (in the centre of the AF and in the four corners), with separate plots for the four window classes (left to right) and two FoVs (top and bottom). Figure A.6 shows the AGIS calibration for observations where the IPD used colour information ( $v_{\text{eff}}$ ) from PhotPipe to remove chromatic variations already before the data reached AGIS. Ideally, therefore, the remaining chromaticity found by AGIS should be negligible. As shown by the figure, this is almost the case for the one-dimensional images (WC1 and WC2), but not for the two-dimensional windows (WC0a and WC0b) used for the bright ( $G \lesssim 13$ ) sources. Thus CALIPD was not fully successful in removing chromaticity by means of the



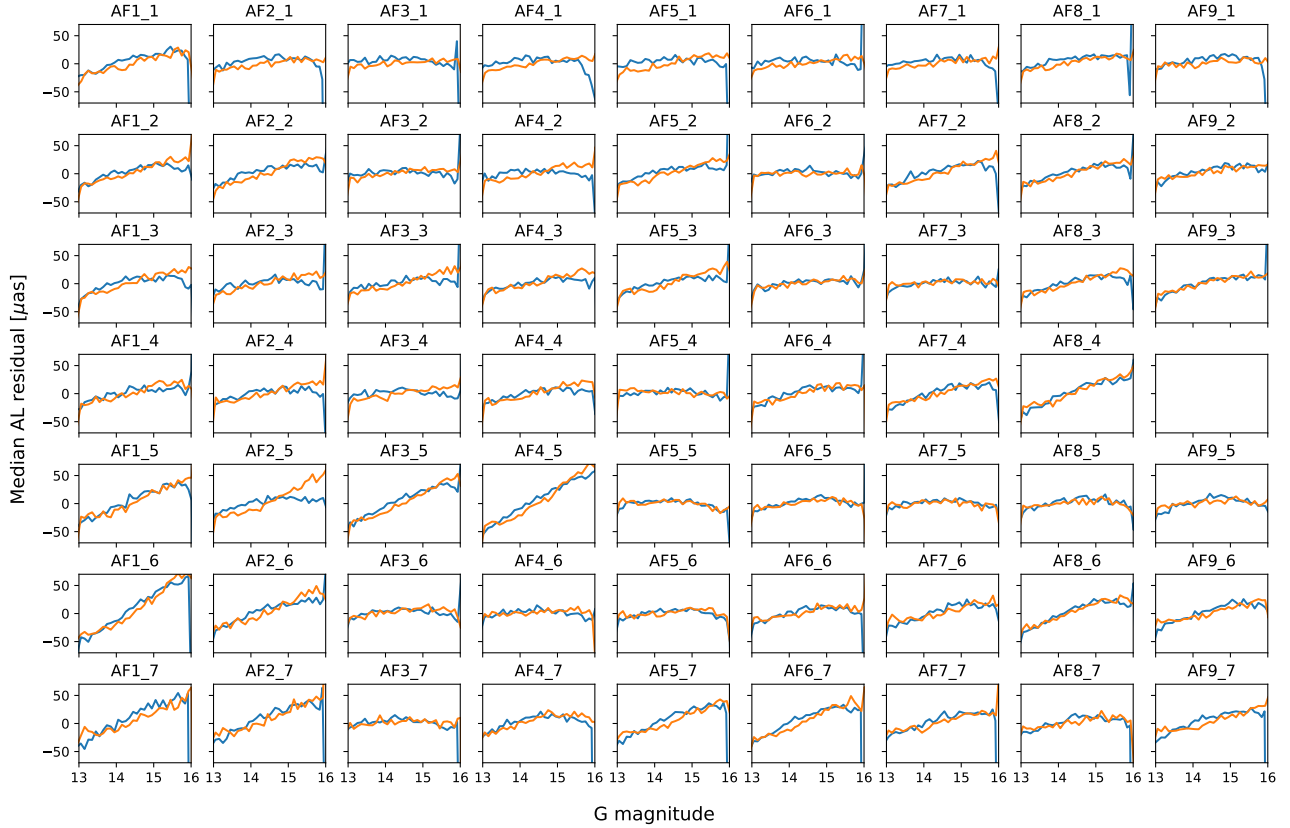


**Fig. A.5.** Median AL residual for WC1 vs.  $G$  (in the range 13–16) for each of the 62 CCDs in the AF. Blue and orange curves are for the PFoV and FFoV. See Fig. 3 for the labelling of the CCDs. The layout is mirror-reversed compared to Fig. 3.

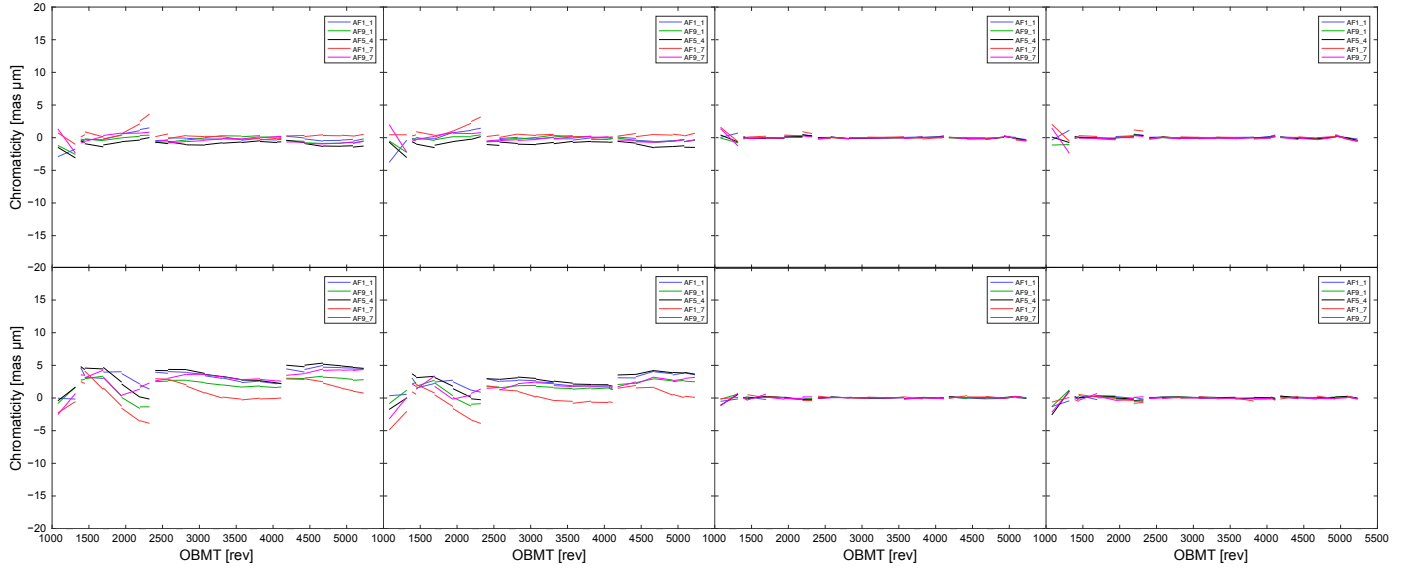
PSF calibrations, while the process worked very well for the LSF calibrations. This is one manifestation of several issues with the cycle 3 PSF modelling that will be resolved in the next cycle (Sect. 6.1 and Rowell et al. 2021).

Figure A.7 shows the corresponding AGIS calibration for observations where IPD used the LSF and PSF calibrations for the default colour  $\nu_{\text{eff}} = 1.43 \mu\text{m}^{-1}$ . Here the chromaticity is much stronger than in Fig. A.6 and largely similar for all four window classes. This figure thus illustrates intrinsic properties of the PSF while differences in the data processing, for example between the one- and two-dimensional windows, play a minor role. The calibrations are substantially different between the preceding and following fields, because they have different optical paths through most of the instrument and consequently different wavefront aberrations for a given CCD. The efficacy of the CALIPD 3.2 LSF calibration in removing chromaticity is striking when comparing the right-hand sides of Figs. A.6 and A.7.

Figure A.8 shows the development of the AL large-scale CTI (effect 6 in Table 2). CTI effects are caused by the complex interaction between the build-up of charge images in the CCDs during the TDI and the radiation-induced defects (charge

traps) in the silicon lattice (Crowley et al. 2016). While the lattice defects are of course the same in the two FoVs, PSF shapes are different, which causes subtle differences between the FoVs in the observed CTI effects. These differences are generally much smaller than the calibration uncertainties, and in order to reduce the latter we have chosen to display in Fig. A.8 only the effect averaged over the CCDs and the two FoVs. In the left-most plot (WC0a), observations are usually gated with the integration time reduced to less than a quarter of the maximum value, and the charge images reach close to the full-well capacity, or even saturate, at the end of the integration. All of these factors combine to make the average CTI effects very small in WC0a ( $\lesssim 5 \mu\text{as}$ ). Only for the slowest traps ( $\tau = 2000$  TDI periods) does the effect become clearly stronger with time. For WC0b and WC1 (the two middle panels in Fig. A.8) the effect is clearly present at all time scales and increasing with time. The strongest effect is also seen here for  $\tau = 2000$  TDI periods. For WC2 ( $G \gtrsim 16$ , in the right-most panel) the effect is mainly seen for  $\tau = 10$  TDI periods. The jumps at OBMT 2400 rev in several of the data series are real and caused by the M-class solar flare on 21 June 2015 (see Fig. 14 in Crowley et al. 2016).





**Fig. A.6.** Chromaticity calibration for image parameters based on  $v_{\text{eff}}$  from the photometric processing (PhotPipe). This is the calibration used for sources with a five-parameter solution (calculated in step 5 of Sect. 4.1). *Top*: preceding FoV. *Bottom*: following FoV. *From left to right*: WC0a, WC0b, WC1, WC2. Each diagram shows the development of the chromaticity term for the five CCDs indicated in the legends. The chromaticity correction in IDU was very successful for WC1 and WC2 (i.e.  $G \gtrsim 13$  mag), but only partially so for brighter sources.

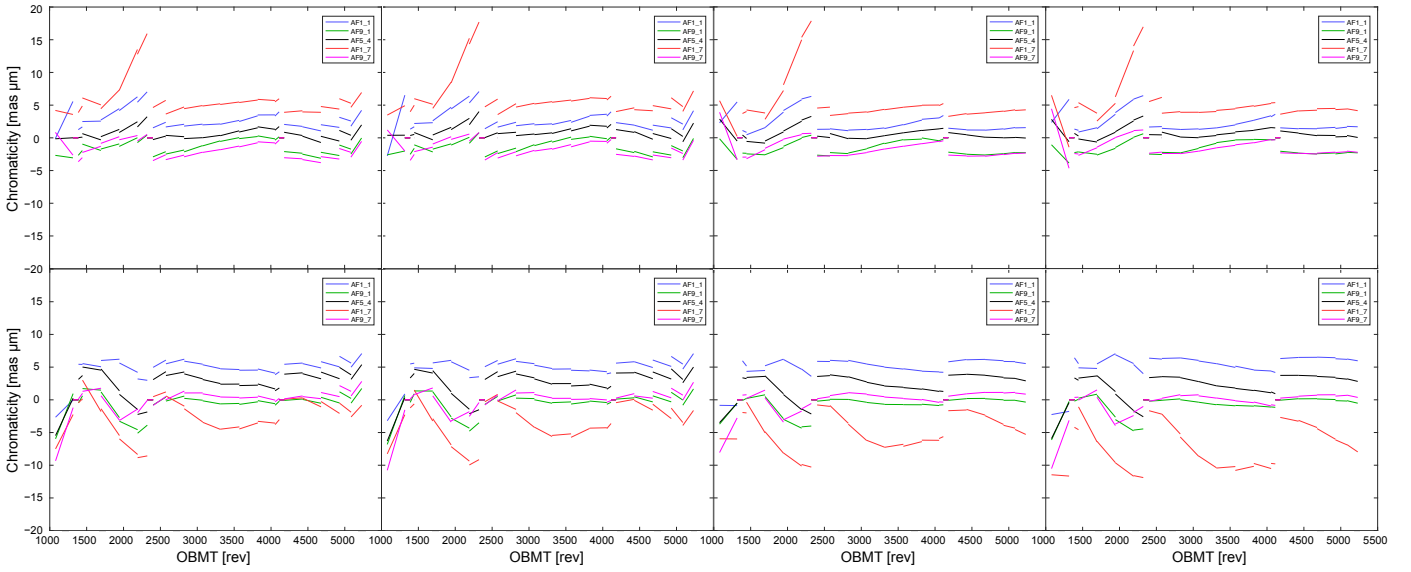


**Fig. A.7.** Chromaticity calibration for image parameters based on default  $v_{\text{eff}} = 1.43 \mu\text{m}^{-1}$ . This is part of the calibration  $C'$  calculated in step 6 of Sect. 4.1, that is for sources that obtain six-parameter solutions in AGIS. *Top*: preceding FoV. *Bottom*: following FoV. *From left to right*: WC0a, WC0b, WC1, WC2. Each diagram shows the development of the chromaticity term for the five CCDs indicated in the legends.

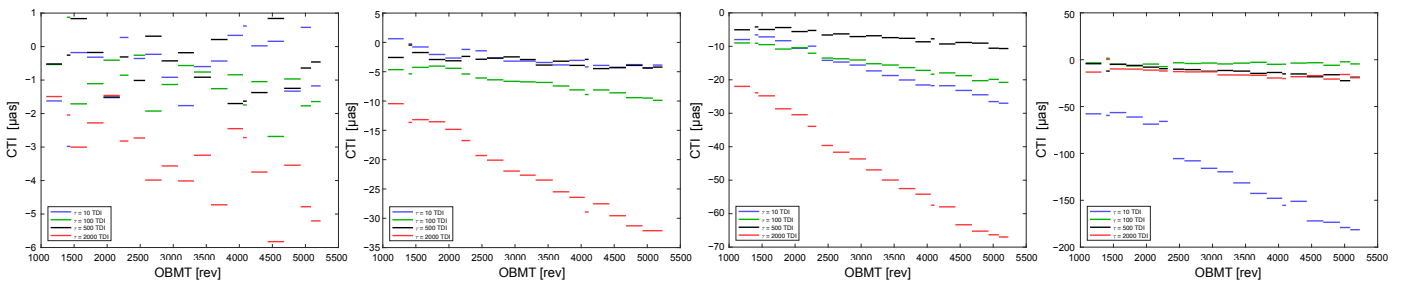


**Fig. A.8.** CTI calibration averaged over CCDs and FoVs. *From left to right*: WC0a ( $G \lesssim 11$ ), WC0b ( $11 \lesssim G \lesssim 13$ ), WC1 ( $13 \lesssim G \lesssim 16$ ), and WC2 ( $16 \lesssim G$ ). Each diagram shows the development of the coefficients of  $\exp(-\Delta t/\tau)$ , where  $\Delta t$  is the time since last charge injection, for the time constants  $\tau$  indicated in the legends.

## Appendix B: Parallax factor and AC rate

The scanning law of *Gaia*, described in Sect. 5.2 of [Gaia Collaboration \(2016a\)](#), specifies the intended (commanded) pointing of the *Gaia* telescopes as a function of time. In its nominal mode (the nominal scanning law, NSL), it causes a strong positive correlation between the AL parallax factor  $\partial\eta/\partial\varpi$  and the AC scan rate  $\dot{\zeta}$ , where  $\eta$ ,  $\zeta$  are the field angles of the source in either of *Gaia*'s FoVs (Fig. 3) and the dot signifies the time derivative. This correlation is illustrated by the blue circles in Fig. B.1 having a correlation coefficient of +0.985. As shown by the red crosses in the figure, the correlation can be reversed by changing the sense in which the spin axis revolves around the direction to the Sun. This mode, known as reversed precession, was used during data segments DS6 and DS7 (16 July 2019 to 29 July 2020; see Fig. 1).

The correlation between the AL parallax factor and the AC rate of a stellar image is a simple consequence of the scanning law and can be understood by considering the spherical triangle AZS in Fig. B.2. The diagram depicts the geometry at an instant when the star at *A* is in the centre of the FoV in the AL direction, that is  $\eta = 0$ . For the star to be inside the FoV at this time, the AC field angle must be small,  $|\zeta| \lesssim 0.4^\circ$ . According to the scanning law, the angle between the Sun (*S*) and the spin axis (*Z*) is fixed at  $\xi = 45^\circ$ , while *Z* revolves around *S* at a rate of 5.8 revolutions per year (precession period about 63 days). In the normal (forward) precession mode of the scanning law, used during most of the mission, *Z* revolves in the positive sense around *S*, so  $\dot{\phi} > 0$ ; in reversed precession mode it revolves in the opposite sense, so  $\dot{\phi} < 0$ . It should be noted that the spin of *Gaia* (with 6 h period) is always positive about *Z* ( $\dot{\chi} > 0$ ), independent of the precession mode.

Parallax  $\varpi$  causes a displacement of the star image by  $p = \varpi d \sin \theta$  in the direction towards the Sun, that is along the great circle *AS*. Here,  $d$  is the Sun–*Gaia* distance in au and  $\theta$  the angle from *A* to *S*. (Here, *S* should be understood as the solar system barycentre, and  $d$  as the distance from the solar system barycentre to *Gaia*, that is  $d_b$  in Sect. 3.4.4. However, for the present discussion – unlike the one in Sect. 3.4.4 – the distinction between barycentric and heliocentric quantities is not important.) The AL component of  $p$  is  $\Delta\eta \cos \zeta = -p \sin \gamma$ , with  $\gamma$  the angle at *A* in the spherical triangle. The AL parallax factor is therefore

$$\frac{\partial\eta}{\partial\varpi} = -d \sin \theta \sin \gamma \sec \zeta = -d \sin \xi \sin \chi \sec \zeta, \quad (\text{B.1})$$

where, in the last equality, we have used  $\sin \theta \sin \gamma = \sin \xi \sin \chi$  from the law of sines<sup>9</sup>.

The AC field angle  $\zeta$  is obtained from the law of cosines,

$$\sin \zeta = \cos \xi \cos \theta + \sin \xi \sin \theta \cos \phi, \quad (\text{B.2})$$

which upon differentiation gives  $\dot{\zeta}$  in terms of  $\dot{\xi}$ ,  $\dot{\theta}$ , and  $\dot{\phi}$ . According to the scanning law we have  $\dot{\xi} = 0$ , while expressions for  $\dot{\theta}$  and  $\dot{\phi}$  are complicated by the need to take into account the motion of the Sun along the ecliptic in addition to the precession. However, as the motion of the Sun is substantially slower than the precession, we may in a first-order approximation regard

<sup>9</sup> Neglecting the size of the FoV, we have  $\chi = \Omega + f\Gamma/2$ , where  $\Omega$  is the heliotropic spin phase,  $f = \pm 1$  the FoV index, and  $\Gamma = 106.5^\circ$  the basic angle. The differential parallax factor (preceding minus following) discussed in Sect. 3.4.4 is then  $-2d \sin \xi \sin(\Gamma/2) \cos \Omega$  ([Butkevich et al. 2017](#)).

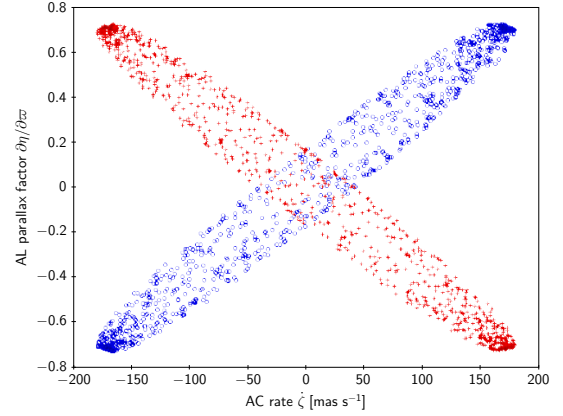


**Fig. B.1.** Correlation between AC rate and AL parallax factor. Blue circles show a random selection of 1000 FoV transits from data segments DS0–DS5, when the scanning law was in its normal (forward precession) mode. Red crosses show 1000 random transits from data segments DS6 and DS7, when the reversed precession mode was used. EDR3 is exclusively based on observations taken in the forward precession mode.

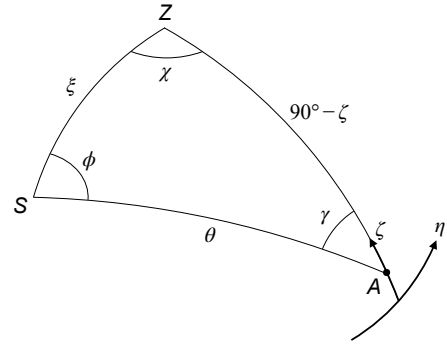


**Fig. B.2.** Spherical triangle for the parallax factor and AC rate. *A* is the position of the star, *Z* the nominal spin axis of *Gaia* (perpendicular to the two viewing directions), and *S* the position of the Sun. The directions of the AL and AC field angles  $\eta$ ,  $\zeta$  are indicated.

both Sun and star as stationary on the sky during an observation, in which case  $\theta \simeq 0$ . Then

$$\dot{\zeta} \simeq -\dot{\phi} \sin \xi \sin \theta \sin \phi \sec \zeta = -\dot{\phi} \sin \xi \sin \chi, \quad (\text{B.3})$$

where we have used  $\sin \theta \sin \phi = \cos \zeta \sin \chi$  from the law of sines. Comparing Eqs. (B.1) and (B.3), while recalling that  $\zeta$  is a small angle so  $\sec \zeta \simeq 1$ , we see that both the AL parallax factor and the AC rate vary as  $\sin \chi$  with nearly constant amplitudes, yielding a very strong correlation between the two quantities. We also see that the correlation has the same sign as  $\dot{\phi}$ , that is positive in the nominal case and negative for reversed precession.

In contrast to the first-order analysis above, Fig. B.2 does not show a perfect correlation between the AC rate and AL parallax factor. This is caused by the motion of the Sun, ignored in Eq. (B.3). A more careful analysis shows that  $\dot{\zeta}$  is not completely in phase with  $\partial\eta/\partial\varpi$ , but is phase shifted by an amount that varies periodically with the precession period of 63 days and an amplitude of  $\pm 13^\circ$ . The elliptical envelopes of the data points in Fig. B.2 are produced by this phase shift. Additional, much smaller modulations are due to variations in the Sun–*Gaia* distance ( $d$ ) and the neglected difference between the nominal Sun, which regulates the scanning law, and the solar system barycentre, which determines parallax.

Because the astrometric solution for EDR3 could not benefit from the decorrelation achieved with the reversed precession beginning in July 2019, it is possible that the EDR3 parallaxes are biased for the sources where the AC smearing has a significant impact on the image parameter determination. From the analysis of residuals we know that this is the case for WC0b observations using the gates with “long” exposure times, which is the reason why the calibration effect depending on the square of the AC rate (effect 7 in Table 2) was restricted to those observations. A subsequent study of the parallax biases in EDR3 (Lindegren et al. 2021) indeed shows a sharp discontinuity of the bias at  $G \simeq 13$  (the faint limit of the affected observations, according to Fig. 4), which could be caused by a location bias proportional to the AC rate in the individual observations, coupled with the positive correlation between the AC rate and parallax factor. A secure disentangling of the AC rate dependency from parallax will only be possible in cycle 4 with the inclusion of observations obtained in the reversed precession mode.

### Appendix C: Adding photometric information in a six-parameter solution

In this Appendix we discuss the possibility, mentioned in Sect. 2.3, to compute improved estimates of the astrometric parameters for a source with a six-parameter solution, when a better colour estimate is available than the astrometrically determined pseudocolour  $\hat{\nu}_{\text{eff}}$ . The colour could be  $G_{\text{BP}} - G_{\text{RP}}$ , if available, or a colour index from a different instrument. A prerequisite for the method is that the photometric colour index, and its uncertainty, can be transformed into an estimate  $\nu_p$  of the effective wavenumber, and a corresponding uncertainty  $\sigma(\nu_p)$ .

For a given source with six-parameter solution, let  $\hat{\alpha}$ ,  $\hat{\delta}$ ,  $\hat{\varpi}$ ,  $\hat{\mu}_{\alpha^*}$ ,  $\hat{\mu}_{\delta}$ , and  $\hat{\nu}_{\text{eff}}$  be the parameters as published in EDR3 and  $\mathbf{K}$  the  $6 \times 6$  covariance matrix computed as in Eq. (23). Given also the photometric estimate  $\nu_p \pm \sigma(\nu_p)$ , we seek a vector of updates,

$$\mathbf{x} = \begin{bmatrix} (\alpha - \hat{\alpha}) \cos \hat{\delta} \\ \delta - \hat{\delta} \\ \varpi - \hat{\varpi} \\ \mu_{\alpha^*} - \hat{\mu}_{\alpha^*} \\ \mu_{\delta} - \hat{\mu}_{\delta} \\ \nu_{\text{eff}} - \hat{\nu}_{\text{eff}} \end{bmatrix}, \quad (\text{C.1})$$

that optimally combine the six-parameter solution with the photometric data. We use the tilde to indicate the updated solution, thus  $\tilde{\mathbf{x}}$  for the optimal update and  $\tilde{\mathbf{K}}$  for its covariance matrix. We use here the notation  $\sigma(\hat{\varpi})$ ,  $\sigma(\tilde{\varpi})$ , etc. for the uncertainties.

On the assumption of a multivariate normal distribution of the errors, the problem can be solved in a Bayesian framework, taking the original and updated parameters as prior and posterior estimates, and the colour information as the data. The same result can be obtained by considering the normal equations for the corresponding least-squares problems, which is the approach taken here.

The original six-parameter solution may be represented by the update vector  $\hat{\mathbf{x}} = \mathbf{0}$  with covariance  $\mathbf{K}$ . The corresponding system of normal equations is

$$\mathbf{K}^{-1} \mathbf{x} = \mathbf{0}. \quad (\text{C.2})$$

It is assumed that observation equations are normalised to unit variance, so that the covariance of the least-squares estimate is obtained as the inverse of the normal matrix.

The unit variance observation equation representing the photometric estimate  $\nu_p \pm \sigma(\nu_p)$  is

$$\mathbf{u}' \mathbf{x} \sigma(\nu_p)^{-1} = (\nu_{\text{eff}} - \hat{\nu}_{\text{eff}}) \sigma(\nu_p)^{-1}, \quad (\text{C.3})$$

where  $\mathbf{u}$  is the column vector  $(0, 0, 0, 0, 0, 1)'$  (the prime indicates transpose). The system of normal equations obtained by adding this observation to the original system reads

$$(\mathbf{K}^{-1} + \mathbf{u}\mathbf{u}' \sigma(\nu_p)^{-2}) \mathbf{x} = \mathbf{u} (\nu_{\text{eff}} - \hat{\nu}_{\text{eff}}) \sigma(\nu_p)^{-2}. \quad (\text{C.4})$$

By means of the Sherman–Morrison formula (e.g. Press et al. 2007), the square matrix in the left member can be inverted to give the covariance matrix of the updated solution,

$$\begin{aligned} \tilde{\mathbf{K}} &= (\mathbf{K}^{-1} + \mathbf{u}\mathbf{u}' \sigma(\nu_p)^{-2})^{-1} \\ &= \mathbf{K} - \mathbf{K}\mathbf{u} (\mathbf{u}' \mathbf{K}\mathbf{u} + \sigma(\nu_p)^2)^{-1} \mathbf{u}' \mathbf{K}, \end{aligned} \quad (\text{C.5})$$

and hence the updated solution

$$\tilde{\mathbf{x}} = \mathbf{K}\mathbf{u} (\mathbf{u}' \mathbf{K}\mathbf{u} + \sigma(\nu_p)^2)^{-1} (\nu_{\text{eff}} - \hat{\nu}_{\text{eff}}). \quad (\text{C.6})$$

The last two equations are readily written in component form thanks to the simple structure of  $\mathbf{u}$ ; thus,

$$\tilde{x}_i = K_{i5} \frac{\nu_p - \hat{\nu}_{\text{eff}}}{K_{55} + \sigma(\nu_p)^2}, \quad i = 0 \dots 5 \quad (\text{C.7})$$

and

$$\tilde{K}_{ij} = K_{ij} - \frac{K_{i5} K_{j5}}{K_{55} + \sigma(\nu_p)^2}, \quad i, j = 0 \dots 5. \quad (\text{C.8})$$

For example, the updated parallax ( $i = 2$ ) is

$$\tilde{\varpi} = \hat{\varpi} + \rho(\hat{\varpi}, \hat{\nu}_{\text{eff}}) \sigma(\hat{\varpi}) \sigma(\hat{\nu}_{\text{eff}}) \frac{\nu_p - \hat{\nu}_{\text{eff}}}{\sigma(\hat{\nu}_{\text{eff}})^2 + \sigma(\nu_p)^2}, \quad (\text{C.9})$$

with uncertainty  $\sqrt{\tilde{K}_{22}}$ , that is

$$\sigma(\tilde{\varpi}) = \sigma(\hat{\varpi}) \sqrt{1 - \frac{\rho(\hat{\varpi}, \hat{\nu}_{\text{eff}})^2}{1 + \sigma(\nu_p)^2 / \sigma(\hat{\nu}_{\text{eff}})^2}}. \quad (\text{C.10})$$

Corresponding expressions hold for the other parameters. For the effective wavenumber ( $i = 5$ ), they can be written

$$\tilde{\nu}_{\text{eff}} = \frac{\sigma(\hat{\nu}_{\text{eff}})^{-2} \hat{\nu}_{\text{eff}} + \sigma(\nu_p)^{-2} \nu_p}{\sigma(\hat{\nu}_{\text{eff}})^{-2} + \sigma(\nu_p)^{-2}}, \quad (\text{C.11})$$

with uncertainty

$$\sigma(\tilde{\nu}_{\text{eff}}) = \left( \sigma(\hat{\nu}_{\text{eff}})^{-2} + \sigma(\nu_p)^{-2} \right)^{-1/2}. \quad (\text{C.12})$$

A few interesting observations can be made concerning the last four equations. We note that the parallax and its uncertainty are unchanged if  $\sigma(\nu_p) \gg \sigma(\hat{\nu}_{\text{eff}})$ , or if there is no correlation between the parallax and pseudocolour,  $\rho(\hat{\varpi}, \hat{\nu}_{\text{eff}}) = 0$ . If  $\nu_p = \hat{\nu}_{\text{eff}}$ , the parallax value is also unchanged, but its uncertainty will decrease if the correlation is non-zero. We note, furthermore, that the parallax uncertainty is at most reduced by the factor  $[1 - \rho(\hat{\varpi}, \hat{\nu}_{\text{eff}})^2]^{1/2}$ , which is reached in the limit when



$\sigma(v_p) \ll \sigma(\hat{v}_{\text{eff}})$ . This means that the potential gain in precision by the procedure may be significant (say, more than 5%), only if the correlation between the pseudocolour and the astrometric parameter of interest is  $\geq 0.3$  in absolute value. For the parallax, this is the case for only about 6% of the sources with six-parameter solutions. The median  $|\rho(\cdot, \hat{v}_{\text{eff}})|$  is about 0.1 for all five astrometric parameters, giving a median improvement in their uncertainties of at most 0.5%. Finally, we note that  $\tilde{v}_{\text{eff}}$  is the mean of  $\hat{v}_{\text{eff}}$  and  $v_p$  weighted by their inverse variances, with uncertainty corresponding to the sum of weights.

Equation (C.9) shows that the updated parallaxes  $\tilde{\varpi}$  are formally more precise than the original values  $\hat{\varpi}$  (for non-zero correlations); however, we want to determine whether they actually are better. The sample of the quasars in `agn_cross_id` with six-parameter solutions offers an opportunity to test this, although the sample is not representative for most six-parameter solutions in EDR3, as the quasars are usually not in crowded areas. Of the 398 231 sources in `agn_cross_id` with six-parameter solutions, 396 445 have colour indices  $G_{\text{BP}} - G_{\text{RP}}$  in the main table. To transform the colours to  $v_p$  we use Eq. (3), from which we also have an expression for the uncertainty:

$$\sigma(v_p) = \frac{1.61}{\pi} \frac{0.531 \sigma(G_{\text{BP}} - G_{\text{RP}})}{1 + [0.531(G_{\text{BP}} - G_{\text{RP}})]^2}. \quad (\text{C.13})$$

In this sample the effective wavenumber derived from the photometric colour is usually much more precise than the pseudocolour: the median  $\sigma(v_p)$  is  $0.03 \mu\text{m}^{-1}$  against a median  $\sigma(\hat{v}_{\text{eff}})$  of  $0.18 \mu\text{m}^{-1}$ . Thus most of the sources should benefit from the procedure, which is confirmed by the statistics in Table C.1. The median formal uncertainty is reduced by 1.2% for the full sample and by 7.7% for the subsample with correlations exceeding  $\pm 0.3$ . That these improvements are actual and not only formal is shown by the dispersions (RSE) of the parallaxes, which are reduced by, respectively, 1.7 and 8.1%. The dispersions of the normalised parallaxes (last line in the table) are practically unchanged by the update.

**Table C.1.** Statistics of original and updated parallaxes for quasars with six-parameter solutions.

Quantity	Unit	Full sample (396 445 sources)		Sub sample (28 806 sources)	
		$\hat{\varpi}$	$\tilde{\varpi}$	$\hat{\varpi}$	$\tilde{\varpi}$
med( $x$ )	[ $\mu\text{as}$ ]	-28.6	-28.3	-41.5	-40.8
med( $\sigma(x)$ )	[ $\mu\text{as}$ ]	836	826	1297	1197
RSE( $x$ )	[ $\mu\text{as}$ ]	973	956	1426	1311
RSE( $\frac{x - \text{med}(x)}{\sigma(x)}$ )	–	1.073	1.074	1.062	1.067

**Notes.** Columns 3 and 4 give statistics on the original parallaxes ( $\hat{\varpi}$ ) and updated values ( $\tilde{\varpi}$ ) for the full sample of quasars having six-parameter solutions and colours in EDR3. Columns 5 and 6 give statistics on the subsample with  $|\rho(\hat{\varpi}, \hat{v}_{\text{eff}})| > 0.3$ . The first two lines of data give the median parallax and median parallax uncertainty, the last two lines the robust scatter estimate (RSE; see footnote 8) of the parallaxes and of the median-centred parallaxes normalised by their uncertainties.

The quasar sample thus demonstrates that the procedure is capable of bringing a real and possibly significant improvement to the astrometry of a six-parameter solution under specific circumstances. Necessary conditions are that the correlation coefficients with pseudocolour are significant, and that a reliable colour is available. Although these conditions hold for a number of the quasars analysed above, they may not apply to more than a small fraction of the sources with six-parameter solutions. It should also be remembered that  $G_{\text{BP}} - G_{\text{RP}}$ , if available in EDR3, may be problematic for these sources. After all, they received six-parameter solutions because they did not have reliable BP and RP photometry in DR2, and the reason for that, such as crowding, may still be present in EDR3. The necessary colour information could of course come from a different instrument with better angular resolution than the BP and RP photometers of *Gaia*.